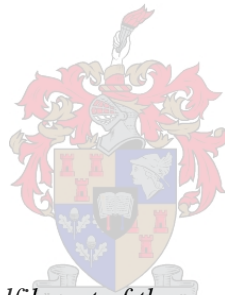


Dimensional Stability of Lightweight Foamed Concrete

By

Dino Roberto Do Amaral



*Thesis presented in fulfilment of the requirements for the degree of
Master of Engineering in Civil Engineering in the Faculty of Engineering
at Stellenbosch University*

Supervisor: Mr Algurnon S. van Rooyen

December 2019

Declaration

By submitting this thesis electronically, I declare that the entirety of the work contained therein is my own, original work, that I am the sole author thereof (save to the extent explicitly otherwise stated), that reproduction and publication thereof by Stellenbosch University will not infringe any third party rights and that I have not previously in its entirety or in part submitted it for obtaining and qualification

Signature:

Date: December 2019

Abstract

Lightweight Foamed Concrete (LWFC) is a variation of low density cellular concrete produced by entraining a system of regular and stable air voids into a mortar base mix. The air void structure in LWFC is created by incorporating a pre-formed aqueous foam into a regular mortar base mix which typically consists of ordinary Portland cement, water, fine aggregates and a variety of supplementary cementitious materials. The result of incorporating this pre-formed aqueous foam is a hardened concrete material which varies in density from 450 kg/m^3 – 1600 kg/m^3 , possess superior fresh state and insulative properties and drastically reduces dead loads on structures. Although significant strides have been made when concerning the mechanical characteristics of LWFC, the durability and long term behaviour properties of this material such as creep and shrinkage remain relatively undocumented. As the long-term dimensional stability of concrete is an essential factor to consider when designing any concrete structure, it is imperative that the creep and shrinkage behaviour of LWFC be investigated, quantified and recorded to aid in commercialising this innovative construction material.

This study investigates and quantifies the long-term creep and shrinkage behaviour of LWFC by means of three separate methods. The first of these is experimental testing on a variety of physical LWFC samples. The effects of density, foam volume, filler type and filler quantity as well as the effects of other additives have all been noted as important parameters to investigate. For this reason, LWFC mixes which vary in density from 1200 kg/m^3 – 1600 kg/m^3 and contain only cement have been tested to investigate the effects of density and foam volume whilst other mixes all with a density of 1400 kg/m^3 containing sand, fly ash and propylene glycol have been tested to investigate the effects of various fillers and additives in different quantities. The second investigation method is the study of three prominent theoretical prediction models which have been examined and their applicability to LWFC assessed. These prediction models are that of the Fib Model Code 2010, EN 1992-1 (2004) and Rilem Model B3. All three models have been calibrated with typical LWFC properties and adjustment factors proposed by comparing their results to experimentally obtained values from physical samples. The last research method utilised is that of developing a nonlinear viscoelastic Kelvin-Chain finite element model in Diana Finite Element Analysis Software. The finite element model utilises direct input of experimental creep and shrinkage curves to accurately replicate the results of physical tests.

The results obtained from physical creep and shrinkage tests indicate that LWFC exhibits drying creep and drying shrinkage strains in excess of $6000 \mu\text{m}$ which is more than six times what is generally seen from ordinary concrete. Additionally, under sealed conditions LWFC exhibits autogenous shrinkage and basic creep strain values which may be as high as $3000 \mu\text{m}$. It has been noted that for drying shrinkage, an inverse relationship appears to be present between density and drying shrinkage strain. For both creep

and shrinkage testing it has been found that the inclusion of both fillers in all ratios results in a decrease in strain values compared to mixes containing only cement. The inclusion of propylene glycol into LWFC is seen to significantly reduce the total amount of drying shrinkage and drying creep strain exhibited. Results from theoretical prediction models show good correlation to ordinary concrete results, however, adjustments factors ranging between 2.7 – 6.3 for shrinkage strains and 0.9 – 1.4 for creep strains have been applied to account for the increased shrinkage and creep behaviour of LWFC. The results obtained from Diana FEA are able to replicate LWFC shrinkage behaviour exactly whilst creep results may be replicated with an average accuracy of 0.46%.

The findings presented in this thesis indicate that the importance of quantifying the long-term deformation behaviour of LWFC cannot be understated. Results indicate that the inclusion of fillers such as sand and fly ash as well as the addition of additives such as propylene glycol are capable of reducing shrinkage and creep strains significantly, however, these strains are still far above what is typically accepted for ordinary concretes.

Opsomming

Liggewig skuimbeton is 'n variasie van sellulêre beton met 'n lae digtheid wat geproduseer word deur 'n stelsel van gereelde en stabiele lugruimtes, wat in 'n mortelbasis mengsel betrek word. Die lugvloei-stofstruktuur in liggewig skuimbeton word geskep deur 'n vooraf gevormde waterige skuim in 'n gewone basismengsel in te sluit, wat gewoonlik bestaan uit gewone Portland-sement, water, fyn aggregate en 'n verskeidenheid aanvullende sementhoudende materiale. Die resultaat van die voorgevormde waterige skuim is 'n geharde betonmateriaal wat in digtheid van 450 kg / m^3 - 1600 kg / m^3 wissel, wat 'n uitstekende vars toestand en isolerende eienskappe bevat, in gevolg verminder dit drasties die dooie las op strukture. Alhoewel daar belangrike vordering gemaak is met betrekking tot die meganiese eienskappe van liggewig skuimbeton, bly die duursaamheid en langdurige gedragseienskappe van hierdie materiaal soos die kruip en krimp gedrag relatief ongedokumenteer. Die langtermyn dimensionele stabiliteit van beton is 'n wesenlike faktor wat in ag geneem moet word by die ontwerp van enige betonstruktuur, dit noodsaak dat die kruip en krimp gedrag van liggewig skuimbeton ondersoek, gekwantifiseer en aangeteken moet word om hierdie innoverende konstruksiemateriaal te kommersialiseer.

Hierdie studie ondersoek en kwantifiseer die langtermyn -kruip- en krimpgedrag van liggewig skuimbeton met behulp van drie afsonderlike metodes. Die eerste hiervan is eksperimentele toetsing op 'n verskeidenheid fisiese liggewig skuimbeton-monsters. Die gevolge van digtheid, skuimvolume, tipe en hoeveelheid opvulmateriaal sowel as die gevolge van ander bymiddels is al opgemerk as belangrike parameters om te ondersoek. Om hierdie rede is liggewig skuimbeton-mengsels wat in digtheid van 1200 kg / m^3 - 1600 kg / m^3 verskil en slegs sement bevat, getoets om die gevolge van digtheid en skuimvolume te ondersoek, terwyl ander mengsels met 'n digtheid van 1400 kg / m^3 sand, vliegassand en propyleenglikol is getoets om die gevolge van verskillende vullers en bymiddels in verskillende hoeveelhede te ondersoek. Die tweede ondersoekmetode is die studie van drie prominente teoretiese voorspellingsmodelle, en die toepaslikheid daarvan op liggewig skuimbeton. Hierdie voorspellingsmodelle is dié van die Fib Model Kode 2010, EN 1992-1 (2004) en Rilem Model B3. Al drie modelle is gekalibreer met tipiese liggewig skuimbeton-eienskappe en aanpassingsfaktore wat voorgestel is deur hul resultate te vergelyk met eksperimenteel verkryde waardes uit fisiese monsters. Die laaste navorsingsmetode wat gebruik is, is die ontwikkeling van 'n nie-lineêre visco-elastiese Kelvin ketting eindige elementmodel in Diana Eindige Element Analiserende Sageware. Die eindige elementmodel maak gebruik van direkte invoer van eksperimentele kruip- en krimp kurwes om die resultate van fisiese toetse akkuraat te repliseer.

Die resultate verkry uit fisiese kruip- en krimptoetse dui aan dat liggewig skuimbeton droogkruip en droë krimp vervormings van meer as $6000 \mu\text{m}$ vertoon, wat dus ses keer meer is as wat algemeen gesien word

uit gewone beton. Boonop het liggewig skuimbeton onder verseëde toestande outogene krimp en basiese kruipvervormingwaardes wat tot $3000\mu\text{m}$ kan wees. Daar is opgemerk dat vir die droging van krimp 'n omgekeerde verband blyk te wees tussen digtheid en drogingskrimpvervorming. Vir beide die kruip- en krimpingsstoetse is daar gevind dat die insluiting van beide vullers in alle verhoudings lei tot 'n afname in vervormingwaardes in vergelyking met mengsels wat slegs sement bevat. Daar word gesien dat die insluiting van propyleenglikol in liggewig skuimbeton die totale hoeveelheid drogingskrimp en droë kruipvervorming aansienlik verminder. Resultate van teoretiese voorspellingsmodelle toon goeie korrelasie met gewone beton resultate, maar aanpassingsfaktore wat wissel tussen 2,7 - 6,3 vir krimpvervormings en 0,9 - 1,4 vir kruipvervormings is toegepas om rekening te hou met die verhoogde krimp en kruipgedrag van liggewig skuimbeton. Die resultate van Diana FEA kan liggewig skuimbeton se krimpgedrag presies naboots, terwyl kruipresultate met 'n gemiddelde akkuraatheid van 0.46% naboots kan word.

Die bevindings wat in hierdie tesis aangebied word, dui aan dat die belangrikheid van die kwantifisering van die langtermyn-vervormingsgedrag van liggewig skuimbeton nie onderskat kan word nie. Resultate dui daarop dat die insluiting van vullers soos sand en vliegassand en die byvoeging van bymiddels soos propyleenglikol die krimp- en kruipvervormings aansienlik kan verminder, maar hierdie vervormings is steeds hoog bo wat gewoonlik aanvaar word vir gewone beton.

Acknowledgements

The information presented in this document is not only the result of many hours of personal determination and commitment, but also a result of the support and guidance of numerous family members, friends and members of staff at Stellenbosch University. Without the support and guidance of these people, the completion of this thesis and Master's degree would have been unthinkable difficult. I would like to thank and acknowledge the following people for their direct and indirect contributions to this thesis:

- My supervisor, Mr. Algurnon Van Rooyen for his vast insight and knowledge about Lightweight Foamed Concrete and for always guiding me with a positive attitude and putting a smile on my face.
- Professor Gideon Van Zijl, for always making an opening to assist and answer questions no matter what the time or topic may be.
- The Concrete Institute for providing the funds that have made it possible for me to further my studies and conduct this research.
- The staff of the concrete laboratory for always lending a helping hand and their valuable insight throughout all stages of this research.
- The administrative staff of the Civil and Structural Engineering Departments, for always assisting with any and all administration issues quickly and with a warm welcome.
- My friends and colleagues within the faculty for their continuous support and assistance on all topics no matter how small or large.
- My mother and father, for allowing me to pursue my passions and get to this point in my life and education. You have supported me from the start of this journey and have always encouraged me to push myself further and never give up.
- My brother and sister, your impeccable example has always inspired me growing up to achieve more. You have always motivated me and supported me through life and every step of this journey.
- My partner Ludwig, your continuous encouragement, late-night coffee service and home-cooked meals are only a few of the countless things I am thankful for during this process.
- My amazing friends, from offering me your intellectual opinions to helping me maintain a social life, you are all deeply valued.
- My cats, thank you for keeping me company when everyone has gone to sleep and laying on my keyboard at all hours of the day.

Table of Contents

Declaration	i
Abstract	ii
Opsomming	iv
Acknowledgements	vi
Table of Contents	vii
List of Figures	x
List of Tables.....	xiii
Nomenclature	xiv
Chapter 1 – Introduction	1
1.1 Background.....	1
1.2 Scope and Objectives.....	2
1.3 Thesis Overview	3
Chapter 2 – Literature Review	4
2.1 Lightweight Foamed Concrete.....	4
2.1.1 Introduction.....	4
2.1.2 Constituents.....	5
2.1.2.1 Portland Cement.....	5
2.1.2.2 Fresh Cement Paste	8
2.1.2.3 Other Constituents.....	8
2.1.3 Microstructure	10
2.1.4 Mix Design.....	14
2.2 Shrinkage and Creep of Concrete	15
2.2.1 Introduction	15
2.2.2 Measuring Shrinkage and Creep	16
2.2.3 Shrinkage and Creep Elements.....	16

2.3	Shrinkage and Creep of LWFC.....	21
2.3.1	Introduction	21
2.3.2	Effects of Fillers	21
2.3.3	Effects of Foam Volume	23
2.3.4	Effects of Moisture Content	24
2.3.5	Effects of Glycol Compounds	25
2.3.6	Effects of Fibre Reinforcement	27
2.4	Existing Numerical Models	27
2.4.1	Fib Model Code 2010.....	28
2.4.2	EN 1992-1-1 (2004)	32
2.4.3	Rilem Model B3	34
2.4.4	Comparison of Numerical Models	37
Chapter 3 – Experimental Design		40
3.1	Materials and Parameters Tested	40
3.2	Mix Designs	41
3.3	Shrinkage and Creep Testing	43
3.4	Supplementary Tests	47
3.4.1	Compressive Strength.....	47
3.4.2	Verification of Load Values	47
Chapter 4 – Finite Element Modelling		48
4.1	Background	48
4.2	Finite Element Model.....	52
4.2.1	Model Creation and Geometry	52
4.2.2	Property Assignments.....	52
4.2.3	Boundary Conditions.....	54
4.2.4	Meshing	54
4.2.5	Analysis	55
4.2.6	Model Comparison	56
Chapter 5 – Results and Discussion		57

5.1	Physical Testing	57
5.1.1	Shrinkage Testing	57
5.1.2	Creep Testing	76
5.2	Physical Results vs Numerical Models	85
5.3	Physical Results vs Finite Element Results	90
Chapter 6 – Conclusions and Recommendations		94
6.1	Conclusions.....	94
6.2	Recommendations.....	96
References		97
Appendices		99
Appendix A – Drying Shrinkage Strains.....		100
A-1:	Average Drying Shrinkage Strain Readings	100
Appendix B – Drying Shrinkage Mass Loss		101
Appendix C – Autogenous Shrinkage Strains.....		102
C-1:	Average Autogenous Shrinkage Strains.....	102
Appendix D – Autogenous Shrinkage Mass Loss		103
Appendix E – Drying Creep Average Strains		104
E-1:	Average Drying Creep Strain Readings	104
Appendix F – Basic Creep Strains		105
F-1:	Average Basic Creep Strains	105

List of Figures

Figure 2-1: Tri-Calcium Silicate Reaction	6
Figure 2-2: Ettringite Shell.....	7
Figure 2-3: 3D Binary and 3D XCT Scans of 300 kg/m ³ LWFC	11
Figure 2-4: Relationship between average air void size and plastic density LWFC	12
Figure 2-5: SEM Images of 500 kg/m ³ (left) and 1000 kg/m ³ (right) LWFC	13
Figure 2-6: SEM Images of 1300 kg/m ³ , 1600 kg/m ³ and 1900 kg/m ³ LWFC.....	14
Figure 2-7: Log-normal frequency distributions for void sizes in 1700 kg/m ³ , 800 kg/m ³ and 300 kg/m ³ LWFC.....	14
Figure 2-8: Graphic indicating different forms of water held in hardened cement paste.....	17
Figure 2-9: Relationship between ambient relative humidity and moisture loss in concrete	18
Figure 2-10: Typical drying shrinkage curve for concrete.....	20
Figure 2-11: Typical drying creep curve for concrete.....	20
Figure 2-12: LWFC drying shrinkage strains for mixes containing sand and fly ash.....	22
Figure 2-13: Drying shrinkage strains for LWFC with varying replacement of fly ash	23
Figure 2-14: Drying shrinkage strains for LWFC containing sand with different foam volumes	23
Figure 2-15: Drying shrinkage strains for LWFC containing fly ash and sand for different foam volumes	24
Figure 2-16: Relationship between drying shrinkage and moisture content for LWFC containing sand	25
Figure 2-17: Relationship between drying shrinkage and moisture content for LWFC containing sand and fly ash	25
Figure 2-18: Chemical structures of PG (a), TEG (b) and DPTE (c).....	26
Figure 2-19: Drying shrinkage strains for LWFC containing glycol compounds.....	26
Figure 2-20: Drying shrinkage strains for LWFC mixes containing different percentages of fillers and fibres.....	27
Figure 2-21: Numerical Model Shrinkage Comparison	38
Figure 2-22: Numerical Models Creep Comparison	39
Figure 3-1: ASTM Flow Table Test 230mm.....	42
Figure 3-2: Paraffin wax sealed sample	46
Figure 3-3: Bearing face after grinding	46
Figure 3-4: Creep samples in loading frame	46
Figure 3-5: MarCator 1075 R Digital Indicator and 100 reference bar.....	46
Figure 3-6: 30kN load verification.....	47
Figure 3-7: Load Cell Setup.....	47

Figure 4-1: Poisson Matrix for Creep Function	48
Figure 4-2: Single Kelvin-Chain Unit	49
Figure 4-3: Kelvin-Chain	50
Figure 4-4: Kelvin-Chain Diana.....	51
Figure 4-5: Curve Fitting Solution Method Diana	51
Figure 4-6: Axisymmetric sheet input for 100mmx200mm cylinder.....	52
Figure 4-7: Direct Shrinkage Curve Input Diana	53
Figure 4-8: Direct Creep Curve Input Diana.....	53
Figure 4-9: Boundary Conditions.....	54
Figure 4-10: Meshed Element	54
Figure 4-11: CQ16A Isoparametric Element	55
Figure 4-12: Shrinkage Modelling Comparisons Diana.....	56
Figure 4-13: Creep Modelling Comparisons Diana	56
Figure 5-1: Relationship between total drying shrinkage and density	59
Figure 5-2: Total Drying Shrinkage Cement-only mixes.....	60
Figure 5-3: Total Drying Shrinkage Cement-ash mixes	61
Figure 5-4: Total Drying Shrinkage Cement-sand mixes	62
Figure 5-5: Total Drying Shrinkage Cement-sand-ash mixes.....	63
Figure 5-6: Total Drying Shrinkage PG mixes	64
Figure 5-7: PG Drying Shrinkage Reductions	64
Figure 5-8: Total Drying Shrinkage all mixes.....	65
Figure 5-9: Total Drying Shrinkage Strains	65
Figure 5-10: Drying Shrinkage Mass Loss.....	67
Figure 5-11: Total Autogenous Shrinkage Cement-only mixes.....	68
Figure 5-12: Total Autogenous Shrinkage cement-sand & cement-fly ash mixes.....	69
Figure 5-13: Total Autogenous Shrinkage cement-sand-fly ash mixes	70
Figure 5-14: Total Autogenous Shrinkage PG mixes	71
Figure 5-15 PG Autogenous Shrinkage Reductions.....	72
Figure 5-16: Total Autogenous Shrinkage Strains	72
Figure 5-17: Total Autogenous Shrinkage Strains Comparison	73
Figure 5-18: Autogenous Shrinkage Mass Losses	75
Figure 5-19: Total Drying Creep Strains.....	78
Figure 5-20: Total Drying Creep Strains Comparison	78
Figure 5-21: Relationship between initial strain and loading force	79
Figure 5-22: Total Specific Drying Creep.....	81

Figure 5-23: Total Basic Creep Strain Comparisons.....	83
Figure 5-24: Total Basic Creep Strains	83
Figure 5-25: Basic Specific Creep Curves	85
Figure 5-26: Numerical Modelling C12.....	86
Figure 5-27: Numerical Modelling C14.....	87
Figure 5-28: Numerical Modelling C16.....	87
Figure 5-29: Numerical Modelling AC1	88
Figure 5-30: Numerical Modelling SC1.....	89
Figure 5-31: Numerical Modelling SCP2	89
Figure 5-32 Diana Shrinkage Modelling SC1	91
Figure 5-33: Diana Shrinkage Modelling AC1	91
Figure 5-34: Diana Shrinkage Modelling AC2	91
Figure 5-35: Diana Shrinkage Modelling ACP2.....	92
Figure 5-36: Diana Creep Modelling SC1	92
Figure 5-37: Diana Creep Modelling AC1.....	92
Figure 5-38: Diana Creep Modelling AC2.....	93
Figure 5-39: Diana Creep Modelling ACP2.....	93

List of Tables

Table 2-1: Typical LWFC Classification Brackets	5
Table 2-2: Typical Portland Cement Constituents	5
Table 2-3: Relationship between target density, foam volume and porosity	11
Table 2-4: Relationship between target density, foam volume and air void size	12
Table 2-5: Fib Cement Coefficients	30
Table 2-6: Rilem B3 Cement Coefficients	36
Table 2-7: Rilem B3 Curing Coefficients	37
Table 2-8: Rilem B3 Relative Humidity Coefficients	37
Table 2-9: Numerical Model Calibration Input Parameters	38
Table 3-1: Water-Solid Ratios	42
Table 3-2: Final Mix Designs for Testing	43
Table 5-1: Shrinkage Testing Mixes	58
Table 5-2: Shrinkage Testing Casting Densities	59
Table 5-3: Total Drying Shrinkage Strains	66
Table 5-4: Total Drying Shrinkage Summary	66
Table 5-5: Time taken to reach 50% final drying shrinkage	66
Table 5-6: Drying Shrinkage Mass Loss	67
Table 5-7: Total Autogenous Shrinkage Strain Values	73
Table 5-8: Autogenous Shrinkage Contribution	74
Table 5-9: Autogenous Shrinkage Summary	75
Table 5-10: Autogenous Shrinkage Mass Losses	75
Table 5-11: Creep Testing Mixes	76
Table 5-12: Creep Testing Casting Densities	77
Table 5-13: Creep Testing Compressive Strengths	77
Table 5-14: Total Drying Creep Values	78
Table 5-15: Creep Tests Young's Modulus	79
Table 5-16: Total Drying Creep Summary	82
Table 5-17: Drying Creep Moisture Loss	82
Table 5-18: Total Basic Creep Strain Values	82
Table 5-19: Basic Creep Contribution	86
Table 5-20: Numerical Model Experimental Input Parameters	86
Table 5-21: Numerical Model Shrinkage Adjustment Factors	88
Table 5-13: Numerical Model Creep Adjustment Factors	90

Nomenclature

Abbreviations

LWFC	Lightweight Foam Concrete
NWC	Normal Weight Concrete
LWAC	Lightweight Aggregate Concrete
FA	Fly Ash
GGBS	Ground Granulated Blastfurnace Slag
SF	Silica Fume
3D XCT	Three-Dimensional X-Ray Computerised Tomography
SEM	Scanning Electron Microscope
C-S-H	Calcium Silicate Hydrate
ITZ	Interfacial Transition Zone
AAC	Autoclaved Aerated Concrete
SRA	Shrinkage Reducing Agent
PG	Propylene Glycol
TEG	Tri-Ethylene Glycol
DPTE	Di-Propylene Glycol Tert-Butyl-Ether
FEA	Finite Element Analysis

Symbols

ρ_{LWFC}	Density of Lightweight Foam Concrete
ρ_{basemix}	Density of mortar base mix
x_c	Mass of cement
w	Water content
w/c	Water-Cement ratio
a/c	Ash-Cement ratio
s/c	Sand-Cement ratio

w/a	Water-Ash ratio
w/s	Water-Sand ratio
RD_f	Relative density of aqueous foam
RD_c	Relative density of cement
RD_a	Relative density of ash
RD_s	Relative density of sand
t	Concrete age
t_s	Concrete age when drying commences
t_0	Age of the concrete at the time of loading
$\sigma_c(t_0)$	Applied external stress
E_{28}	Young's Modulus of concrete at 28 days age.
f_{cm}	Mean compressive strength
RH	Relative Humidity of ambient environment
H	Notional size of the member
L_0	Original gauge length
L_i	Length measured at time increment "i"
F	Maximum load at failure
A_c	Cross-sectional are of specimen
K	Spring stiffness
C	Viscous damping coefficient
V_f	Volume of aqueous foam
$\epsilon_{ci}(t_0)$	Initial strain at loading
$\epsilon_{cc}(t)$	Creep strain
$\epsilon_{cas}(t)$	Autogenous shrinkage strain
$\epsilon_{cds}(t, t_s)$	Drying shrinkage strain
$\epsilon_{cas0}(f_{cm})$	Notional autogenous shrinkage coefficient

$\epsilon_{cds0}(f_{cm})$	Notional drying shrinkage coefficient
$\epsilon_{sh\infty}$	Ultimate shrinkage strain
ϵ_{cs}	The total shrinkage strain.
ϵ_{cd}	The total drying shrinkage strain.
ϵ_{ca}	The total autogenous shrinkage strain.
ϕ_{bc}	Basic creep coefficient.
ϕ_{dc}	Drying creep coefficient
ϕ_0	Notional creep coefficient.
ϕ_{RH}	Factor to allow for the effects of relative humidity.
α_{as}	Autogenous shrinkage coefficient dependent on type of cement
α_{ds1} & α_{ds2}	Drying shrinkage coefficients dependent on type of cement
β_{RH}	Ambient relative humidity coefficient.
$\beta(f_{cm})$	Factor to allow for the effects of concrete strength.
$\beta(t_0)$	Factor to allow for the effects of concrete age.
$\beta_c(t, t_0)$	Coefficient to describe the development of creep with time after loading.
β_H	Factor to allow for the simultaneous effects of RH and notional size.
$\beta_{as}(t)$	Autogenous shrinkage time function.
k_h	Coefficient dependent on notional size.
κ_h	Humidity dependence coefficient.
$S(t)$	Time function for shrinkage
$J(t, t')$	Compliance Function
$C_0(t, t')$	Basic creep compliance
$C_d(t, t', t_0)$	Drying creep compliance
t_r	Retardation time
λ_α	Retardation time

Chapter 1 – Introduction

In a time where there is increasing pressure to reduce our footprint on the Earth and develop infrastructure which is more sustainable, there is a surge in efforts to develop and better understand the behaviour and characteristics of alternative construction materials. Lightweight Foamed Concrete (LWFC) is a revolutionary construction material which provides many benefits over the use of ordinary Normal Weight Concrete (NWC) in non-structural, semi-structural and structural applications. Although not new to the engineering community, this sparsely researched and documented material has gained significant interest in recent years as large-scale utilisation may only be possible once its mechanical and long-term characteristics are fully understood.

This chapter provides a brief overview of LWFC including its benefits and possible challenges hindering its increased use. This is then followed by the scope of research included in this thesis as well as the key research objectives identified. Finally, any and all limitations hindering research efforts have been identified and a brief chapter outline of this thesis is provided.

1.1 Background

Aerated concrete is a construction material which in its most basic form was invented by the early Romans but not officially classified and patented until the early 1920's (Amran, Farzadnia & Ali, 2015). The production of LWFC involves the mixing of a mortar base mix which is then entrained with a system of stable and regular air voids by means of incorporating a pre-formed aqueous foam. The mortar base mix often consists of Portland cement, water, fine aggregates and a variety of supplementary cementitious materials. The aqueous foam on the other hand, is attributed to a solution of water and either synthetic or natural foaming agents. When compared to (NWC) which typically has a density of 2400 kg/m^3 , the combination of this mortar base mix with aqueous foam yields a hardened concrete material which typically ranges in densities from $450 \text{ kg/m}^3 - 1600 \text{ kg/m}^3$ (Ramamurthy, Kunhanandan Nambiar & Indu Siva Ranjani, 2009).

There are several advantages that exist both in the fresh and hardened states which promote the use of LWFC as an alternative to NWC. These include self-compaction, minimal consumption of aggregate, lowering of structural dead loads, excellent thermal and acoustic insulation and increased fire resistance. Conversely, the air-void system which provides LWFC with these benefits may also be leading cause of its negative characteristics, the most prominent of which include diminished mechanical properties including compressive strength and Young's modulus. Research efforts to improve and quantify the

mechanical characteristics of LWFC such as that of (Nambiar & Ramamurthy, 2006) and (De Villiers, 2015), have yielded results which indicate that this material may be approaching the point where its use would be viable and favourable over equivalent NWC. However, the lack of knowledge pertaining to the long-term behaviour of this material is still one factor to be addressed before LWFC may be used in large-scale structural and semi-structural applications.

When carrying out the design procedure of concrete structures, structural engineers are required to account for both the ultimate and serviceability limit states. Whilst mechanical characteristics are required for accurate calculation of the former, the time-dependent strains of hardened concrete such as creep and shrinkage are one of the characteristics to be considered for the accurate calculation of the latter. Shrinkage may be described as the time-dependent volumetric change of an unrestrained and unloaded concrete member whilst creep may be described as the time-dependent volumetric change of a concrete member subjected to sustained loading. These two phenomena are expanded upon in later sections, however, their concept is important to note as their quantification and prediction is essential in assessing and mitigating the effects of cracking and long-term deflections in concrete structures.

Whilst extensive research has been conducted over decades on the creep and shrinkage strains of NWC, the information available on the creep and shrinkage behaviour of LWFC is severely limited. If LWFC is to be used extensively in the future as an alternative to NWC, it is imperative that this long-term deformation behaviour be fully understood and quantified. In doing so, it is possible to aid in the expansion of understanding this revolutionary material and also provide engineers with the tools they require to carry out safe and effective designs for structures incorporating LWFC.

1.2 Scope and Objectives

The use of LWFC as a structural and semi-structural construction material is a relatively new development and has been hindered by insufficient mechanical properties and lack of long-term behaviour information. Research efforts focused on improving mechanical characteristics of LWFC such as (Kearsley & Wainwright, 2001) and (de Villiers, van Zijl & van Rooyen, 2017) have been implemented with success. Thus, the main focus of this research is expanding the currently limited knowledge pertaining to long term deformation behaviour, particularly creep and shrinkage strains. This research does not focus on additional strains attributed to thermal and chemical factors but rather focuses on creep and shrinkage strains attributed to internal hydration (self-desiccation), internal moisture migration and evaporation (drying). The main objective of this research is to quantify and attain a holistic understanding of the creep and shrinkage behaviour of LWFC and aid in the process of codifying LWFC for structural design. The key research objectives identified are as follows:

- i. The primary objective of this thesis is to experimentally quantify and reduce the time-dependent creep and shrinkage strains of physical LWFC specimens by investigating the effects of density, foam volume, cement paste content, supplementary cementitious materials as well as any other additives.
- ii. Investigate current theoretical prediction models which allow for the calculation of creep and shrinkage strains in NWC and Lightweight Aggregate Concrete (LWAC). Populate these models with known LWFC properties and compare results to experimentally obtained strain readings. This is to be done in order to determine the accuracy and applicability of these models to LWFC specifically and if any, what adjustments should be made.
- iii. Develop a nonlinear Finite Element Model which is capable of replicating the time-dependent creep and shrinkage strains of LWFC specimens. These finite element results are also compared to experimentally obtained strains and theoretical results from prediction models.

1.3 Thesis Overview

Chapter 2 comprises an extensive literature review which unpacks the current knowledge of LWFC in general and its microstructure which is then followed by information pertaining to creep and shrinkage mechanisms in NWC as well as creep and shrinkage in LWFC. The chapter is concluded by investigating three current numerical creep and shrinkage prediction models. Chapter 3 describes the experimental design procedure utilised in the testing of physical samples for creep and shrinkage measurements as well as any supplementary testing that needs to be performed. In Chapter 4, background theory is provided on the methods utilised by Diana Finite Element Analysis Software to model creep and shrinkage of concrete as an ageing viscoelastic material. This chapter then also goes on to describe the finite element model set up and provides examples of some obtained results. Chapter 5 comprises the results and discussions where the results obtained from physical testing are compiled, shown and broken down. This chapter presents results for drying shrinkage, autogenous shrinkage, basic creep and drying creep measurements. In addition, numerical model and finite element results for LWFC are compared to physical results. This thesis is concluded with Chapter 6 which presents a summary of the research conducted, indicates the main observations and conclusions drawn from testing as well provides some indication of suggestions for further researching of the topic.

Chapter 2 – Literature Review

This chapter unpacks some of the most relevant information and research relating both to LWFC and creep and shrinkage of concretes in general. An overview of LWFC is given which includes some standard definitions and properties as well as information relating the most prominent constituents present within typical LWFC mixes. In addition, the microstructure and air-void structure of LWFC is studied and finally the mix design procedure is broken down. Creep and shrinkage of NWC and LWFC is also discussed including the mechanism associated with creep and shrinkage as well as the effects of fillers, foam volume and other SCMs. Finally, three of the most prominent numerical creep and shrinkage prediction models are studied and compared to assess their suitability for use in predicting the creep and shrinkage behaviour of LWFC.

2.1 Lightweight Foamed Concrete.

2.1.1 Introduction.

The concept of aerating traditional concrete and mortar mixtures with the intention of enhancing their properties is not something unique to modern engineering. In fact, it has been historically documented that early Roman societies stumbled upon the phenomenon when animal blood was added to mixtures consisting of small gravels, coarse sands, hot lime and water (Amran, Farzadnia & Ali, 2015). With some external agitation it was discovered that small air bubbles were generated within the mortar mix which improved both its workability and durability and thus, the rudimentary concept of foamed concrete and its advantages was discovered.

It was, however, a man by the name of Axel Eriksson whom first patented the first Portland cement-based foamed concrete in 1923. Definitions in literature vary from lightweight to cellular to aerated concrete, however, it is essential to note that the complete lack of any coarse aggregates technically categorises this material as a cement paste or mortar. Lightweight Foamed Concrete (LWFC) as it shall from here on forward be referred to, is produced by combining a base cement paste or mortar mixture with a pre-formed foam to achieve a final product which contains a regular and stable entrained air-void system which can occupy up to 85% of the material volume. The resultant material possesses a density which should fall in the range of 450 kg/m^3 – 1600 kg/m^3 which provides numerous advantages over Normal Weight Concrete (NWC) which with the addition of steel reinforcement can reach densities of 2500 kg/m^3 .

LWFC possesses many superior qualities to NWC such as improved workability and durability, minimised material consumption, low self-weight, improved thermal and acoustic insulation and increased fire resistance. Although initially envisaged as a non-structural filling material, advancements in cement, admixture and foaming agent technologies has seen the viability of using this material for

structural applications improve significantly in recent years. It is universal and may be applied to monolithic as well as prefabricated elements and provides a more economical solution to the manufacturing of large scale lightweight construction components. In addition to this, it also combines the positive properties of both construction and insulation materials (Namsone, Šahmenko & Korjakins, 2017). Table 2-1 indicates the typical classification brackets for LWFC.

Table 2-1: Typical LWFC Classification Brackets

Concrete Type	Density (kg/m ³)	Compressive Strength (MPa)
Constructive LWFC	600-2000	6-60
Insulating LWFC	350-600	1-6
Ultra Lightweight LWFC	<350	0.1-2

2.1.2 Constituents.

LWFC in its most basic form is a combination of Portland cement, fine aggregates, water and pre-formed aqueous foam. It is also common practice to include a multitude of different fibres, SCMs and superplasticisers depending on the desired fresh or hardened state properties. As Portland cement is perhaps the most important constituent in any concrete and the long-term deformation behaviour of concrete is often associated with the characteristics of the hardened cement paste, some background on the reactions involved in the hydration of ordinary Portland cement must first be provide.

2.1.2.1 Portland Cement.

Table 2-2 adapted from (Owens, 2013) is provided to aid in the explanation of the processes involved in the hydration of ordinary Portland cement. This table indicates the five major constituents present in typical Portland cement which consist of the four main oxides as well as gypsum.

Table 2-2: Typical Portland Cement Constituents

Cement Compound	Chemical Formula	Group
Tri-Calcium Silicate (Alite)	3CaO.SiO ₂	Silicates
Di-Calcium Silicate (Belite)	2CaO.SiO ₂	Silicates
Tri- Calcium Aluminate	3CaO.Al ₂ O ₃	Aluminates
Tetra-Calcium Alumino-Ferrite	4CaO.Al ₂ O ₃ .Fe ₂ O ₃	Aluminates
Gypsum	CaSO ₄	Sulphate

When water is added to Portland cement powder, each of the individual compounds indicated in Table 2-2 undergoes hydration and contributes to the final concrete product. However, it is only the silicates that are responsible for the strength of the final product. A brief summary of each hydration reaction adapted from (Mehta & Monteiro, 2006) and (Domone & Illston, 2010) follows.

(i) Tri-Calcium Silicate Reaction

It is the tri-calcium silicate reaction which is responsible for the majority of concrete strength within the first seven days after hydration has occurred. Upon the addition of water, there is a rapid reaction which results in the release of calcium ions, hydroxide ions and heat. The release of alkaline hydroxide ions OH⁻ also causes a sudden increase of the pH to over 12. This reaction continues producing calcium and hydroxide ions until saturation occurs. At this point the calcium hydroxide begins to crystallise whilst calcium-silicate-hydrate (C-S-H) begins to form simultaneously. This results in the precipitation of ions out of solution which accelerates the reaction of tri-calcium silicate to calcium and hydroxide ions, this is known as Le Chatlier's principle.

The continued formation of both calcium hydroxide and calcium silicate hydrate crystals provides nucleation points upon which more calcium-silicate-hydrate can form. The calcium-silicate-hydrate crystals form a layer over the un-hydrated tri-calcium silicate which grows thicker over time making it more difficult for water molecules to diffuse. This phenomenon explains why the calcium-silicate-hydrate reaction slows over time. Figure 2-1 provides a visual representation of what is meant with the above-mentioned tri-calcium silicate reaction whilst Equation 2.1 provides the equation for the hydration of tri-calcium silicate.

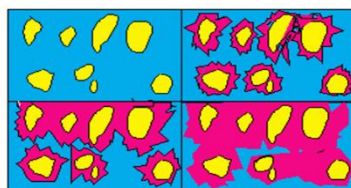


Figure 2- 1: Tri-Calcium Silicate Reaction

(ii) Di-Calcium Silicate Reaction

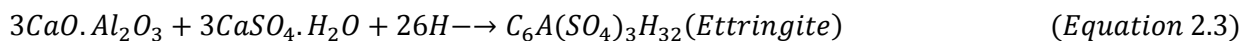
The reaction of Di-Calcium Silicate occurs much in the same manner as that of Tri-Calcium Silicate, however, it occurs at a much slower rate, releases less heat and is thus only responsible for concrete strength at a later stage. The products formed from this reaction are exactly the same as those from the tri-calcium silicate reaction and the hydration equation is given as follows:



(iii) Tri-Calcium Aluminate and Tetra-Calcium Aluminoferrite Reactions

As was stated earlier, it is only the silicates which contribute to the final strength of the concrete product, however, this does not mean that the aluminates may be neglected. As their reactions are complicated by the involvement of gypsum, only a brief explanation of the hydration reactions are given. When tri-calcium aluminate is hydrated, there is an intense and rapid reaction which occurs which releases a large amount of heat and results in flash setting. It is for this reason that gypsum is added into standard Portland cement mixes.

Calcium sulfoaluminate hydrates react with tri-calcium aluminate to prevent flash setting by reacting to form ettringite crystals according the following reaction:



The ettringite shell shown in Figure 2-2 adapted from (Robert, Robert, Tristana, Thomas & Kamyar, 2015) which is comprised of countless needle shaped crystals is impermeable to water and slows down the hydration reaction of tri-calcium aluminate. This ettringite shell is broken down after a few hours with the onset of cement hydration and hexagonal monosulfate hydrate ($C_4ASO_4H_{18}$) crystals are formed as a result of the reaction between the remaining tri-calcium aluminate and sulphates.

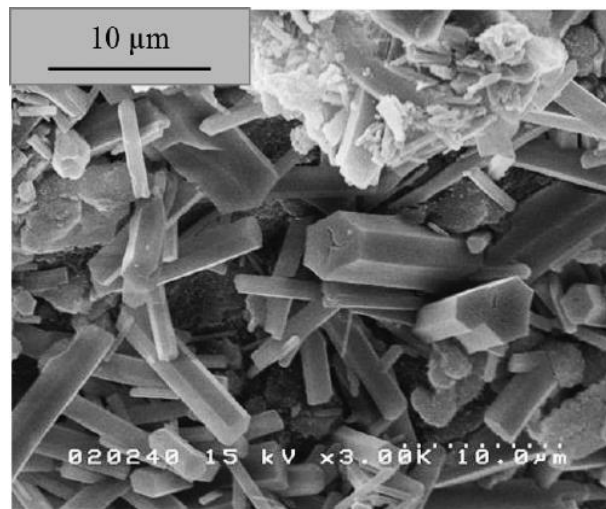


Figure 2-2: Ettringite Shell

The tetra-calcium aluminoferrite reaction results in the production of reaction products similar to that resulting from the tri-calcium aluminate reaction (Calcium sulfoaluminate hydrates). However, this reaction is slower and has no significant influence on the final concrete.

2.1.2.2 Fresh Cement Paste

As the hydration reaction between Portland cement powder and water has been discussed, it is possible to discuss their combined influence as a homogenous fresh cement paste once hydration has occurred. To begin this discussion, it is essential that the defining characteristics of a cement paste are understood, and thus exactly how it is classified. Cement paste may be classified at rest as Bingham-type fluid (Du & Folliard, 2005). This classification rests upon two defining characteristics of the paste itself, the first of these being the yield strength and the second being the apparent viscosity. These two properties play a fundamental role in air entrainment in the following ways.

All air voids present within a paste possess a buoyancy force which allows them to migrate through and out of the paste. In the case of cement pastes, the yield strength is the governing factor which determines with what ease entrained voids may migrate through and out of the paste. Only air voids that possess a buoyancy force greater than that of the paste's yield strength are able to migrate through and out whilst those with smaller buoyancy forces remain entrained within the paste itself. The apparent viscosity of a cement paste also plays two significantly important roles. The viscosity of a paste influences its ability to absorb shock and prevent disturbance to entrained air voids as well as influencing the ease with which entrained air voids are able to coalesce and destabilise the system. Thus, it may be presumed that both cement pastes with higher yield strengths and viscosity are more suitable for air entrainment, however, special attention should be given as to the effects this has on the desired final workability of the mixture.

2.1.2.3 Other Constituents

The process of entraining air in concrete although advantageous in many ways, does not come without its consequences. High porosity is directly linked to the reduction and limitation of mechanical strength and is simultaneously responsible for increased water absorption and drying shrinkage (Namsone, 2017). As a means of minimising these effects as much as possible, (Ramamurthy, Kunhanandan Nambiar & Indu Siva Ranjani, 2009) have noted that rapid-hardening Portland cements and cement powders high in alumina and calcium sulfoaluminates have been used in LWFC mixtures with the intention of reducing setting time and improving early age strength.

Another highly useful and cost-effective method of combatting the adverse effects of air entrainment in concrete is the use of varying types and quantities of SCMs such as fly ash (FA), ground granulated blastfurnace slag (GGBS) and silica fume (SF). Multiple studies such as those of (Hilal, Thom & Dawson, 2015a) and (Nambiar & Ramamurthy, 2006), have indicated that the inclusion of FA as well as GGBS in LWFC mixes are effective ways to reduce the overall cost of the product, improve consistency and workability and lower the overall heat of hydration whilst still contributing positively to the overall long-term strength gain of the concrete. Although not used to lower the overall cost and act as a filler, the use of SF in LWFC mixes has also been documented to positively aid in the long term strength gain of the final concrete. Whilst there are no set rules on the replacement ratios of Portland cement with SCMs as

varying research goals dictate varying constituent requirements, various studies indicate that replacement values are typically 30-70% for FA, 10-50% for GGBS and up to 10% for SF.

Whilst the water-cement ratio often dictates the final strength of a NWC specimen, the water requirement of a LWFC mix is more responsible for the consistency and stability of the concrete in the fresh state and is dependent on the characteristics and composition of individual admixtures. The consistency and viscosity of the cement paste is the energy barrier responsible for ensuring air voids remain entrained in the mixture (Du & Folliard, 2005). Mixes with lower water contents are often stiffer and may lead to insufficient air void size or void breakage, whilst mixes with higher water contents may become too thin resulting in the separation and segregation of the paste-void system. It is thus, imperative in LWFC mixes that the correct water-cement ratio be determined as the importance of total water content in LWFC mixes cannot be over-emphasised.

The use of various superplasticisers as well as natural and synthetic fibres has become common practice in almost all special application concretes. The complex interaction between hydration products and surfactant molecules means that the use of superplasticisers in LWFC mixes has been limited primarily due to the fact that in many cases there is a negative effect on the stability of the generated foam (Kunhanandan Nambiar & Ramamurthy, 2008). Whilst the use of superplasticisers in LWFC is possible, it is not favoured as the complexity of modern chemical admixtures which sometimes act as foaming agents themselves means it is impossible to generalise their reactions with foam (Du & Folliard, 2005). On the other hand, the use of fibres has been documented in studies such as that of (Awang & Ahmad, 2015) to significantly enhance the viability of structural LWFC. In particular, shorter 12 mm polypropylene fibres in the dosage range 1-3 kg/m³ have been seen to increase the shear capacity of LWFC to an equivalent NWC value. In addition to this, fibres have also been documented to reduce brittleness and improve the final strength of the concrete whilst simultaneously reducing the total weight and cost of the mix.

This section is concluded with arguably the most important constituent of LWFC, the foam itself. LWFC may vary either by the use of natural or synthetic foaming agents and the foaming method used. The pre-foaming method of producing LWFC consists of preparing a base mix and a pre-formed foam separately and combining afterwards. The base mix is first produced by combining research specific quantities and variations of Portland cement, fine aggregates, SCMs, admixtures and water which yields a cement mortar. This is then combined with a pre-formed foam which may be generated by either the wet or dry foaming method. In the production of foam using the wet foaming method, a solution of water and foaming agent is sprayed over a fine mesh which yields a foam with bubbles sizes of approximately 2-5mm and is relatively unstable and therefore not favoured. In the dry foaming approach, a 40:1 solution of water and hydrolysed protein foaming agent together with 1.25 grams of sulphate powder per litre is forced simultaneously with compressed air through a series of high density restrictions. The result is a far

more stable and easier to blend foam which has a target density of approximately 75g/l and bubbles smaller than 1mm in size (Ramamurthy *et al.*, 2009).

2.1.3 Microstructure

The incorporation of pre-formed aqueous foam and resulting air-void structure is undoubtedly the most important factor responsible for the unique fresh and hardened state properties of LWFC. In addressing the topic of microstructure as it pertains to LWFC specifically, it first needs to be clarified that macro-pores are created by air entrainment whilst smaller meso/capillary-pores (>10nm) and micro/gel-pores(<10nm) are present in the hardened cement paste (Hilal, Thom & Dawson, 2015b). Understanding this pore structure and air-void system is essential as it determines not only the mechanical characteristics of LWFC, but also durability aspects. It is also important to note that various research efforts on the topic seem to indicate that negative effects on mechanical properties of LWFC such as reduced compressive strength and Young's modulus have been attributed to larger macro-pores and meso-pores, whilst smaller micro-pores present in the gel are believed to be a contributing factor to creep and shrinkage (Hilal *et al.*, 2015) When investigating the topic of microstructure and its link to air-void systems, there appear to be three main areas of interest. The first of these is the total air content or porosity, the second being the average air void size and finally the air void size distribution.

2.1.3.1 Porosity

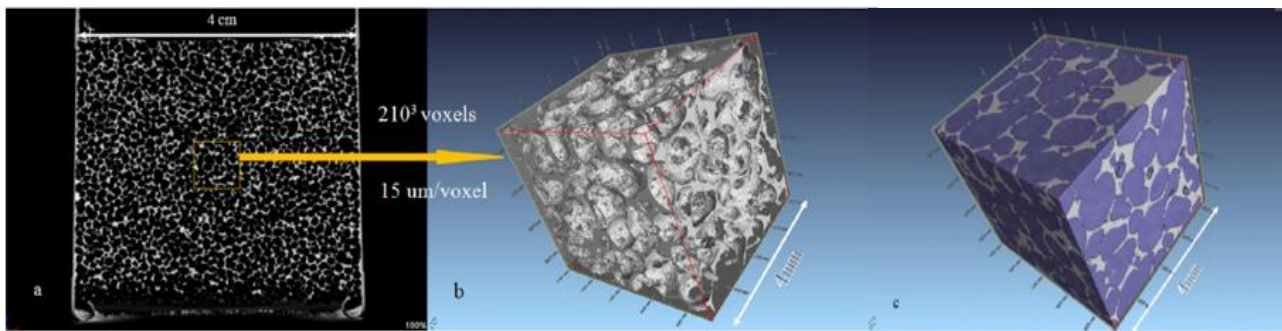
In a study conducted by (Hilal *et al.*, 2015b), it is stated that as the shape, size and distribution of individual air-voids within the concrete may play a vital role in the behaviour of LWFC and thus, simply investigating the total air-void content is not sufficient. As the microstructure of hardened cement paste is not affected by the inclusion of pre-formed aqueous foam, the total air content and porosity in LWFC may be attributed to the entrained air voids only. With this simplification known, the task of calculating total porosity in LWFC may be done by evaluating the ratio of dry density after incorporation of foam and curing to that of the dried and cured density of the equivalent mortar mix with no foam added. Equation 2.4 represents what is meant by this:

$$Porosity = 1 - \frac{\rho_{LWFC}}{\rho_{base\ mix}} \quad (Equation\ 2.4)$$

The relationship between target density, foam volume and porosity may be seen in Table 2-3 adapted from a study conducted by (Wei, Yiqiang, Yunsheng & Jones, 2013). This table indicates the results of porosity calculations performed using Equation 2.4 as well as three-dimensional X-ray computerised tomography (3D XCT). It may be seen that there is a strong correlation in results obtained from both methods and increasing the total foam volume of the LWFC increases the total porosity accordingly. Figure 2-3 is also provided as a visual aid to emphasise the total amount of air voids present in a 300 kg/m³ LWFC mix tested.

Table 2-3: Relationship between target density, foam volume and porosity

Mix	Target Density (kg/m ³)	V _{foam} (%)	Porosity (%)	
			Equation 2.1-4	3D XCT
A	1900	0	-	-
B	1700	10.5	12.51	12
C	1500	21.0	21.87	21.39
D	1300	32.5	35.78	35.5
E	1000	47.3	49.30	47.24
F	800	57.9	59.52	59
G	600	68.4	69.52	69.22
H	500	73.7	75.78	75.45
I	400	78.9	80.00	79.19
J	300	84.2	86.52	84.17

Figure 2-2: 3D Binary and 3D XCT Scans of 300 kg/m³ LWFC

2.1.3.2 Air Void Size

With the overall relationship between target density, foam volume and porosity explored, it is possible to delve into some of the finer details of the air-void structure, the first of these being the average air void size. In the same study conducted by (Wei *et al.*, 2013), the effects of air void size have been investigated by utilising the 3D XCT technology to measure the average size of voids in mixes varying only in total foam volume and plastic density. The results shown in Table 2-4 and Figure 2-4 indicate that increasing the total amount of entrained air by increasing the foam volume results in an increase in the average size of air voids present. In fact, there appears to be profound increase in the size of air voids in mixes with less than forty-eight percent total cement paste whilst the average air void size of higher density mixes approaches an approximate asymptotic value of 0.1mm - which is the average size of air bubbles in the pre-formed foam on its own. By increasing the total amount of foam present it is believed that increase in total voids as well as the reduction in cement paste both actively contribute to increasing void size. As mentioned in previous sections, the viscosity and yield strength of cement paste is responsible for

preventing void migration. By decreasing the total quantity of paste whilst simultaneously increasing the total amount of air voids, these smaller voids are able to migrate and coalesce into larger irregular air voids, thus increasing the average size of voids present in the mix. This phenomenon is shown visually in Figure 2-5 which indicates the scanning electron microscope (SEM) images of a 500 kg/m³ mix and a 1000 kg/m³ mix. It should also be noted that for a study conducted by (Hilal *et al.*, 2015b) for a fixed foam volume, mixes containing fly ash appeared to present with smaller average void sizes than mixes containing sand.

Table 2-4: Relationship between target density, foam volume and air void size

Mix	Target Density (kg/m ³)	V _{foam} (%)	Average air-void size (mm)
A	1900	0	-
B	1700	10.5	0.104
C	1500	21.0	0.113
D	1300	32.5	0.122
E	1000	47.3	0.173
F	800	57.9	0.263
G	600	68.4	0.59
H	500	73.7	0.7
I	400	78.9	0.8
J	300	84.2	0.956

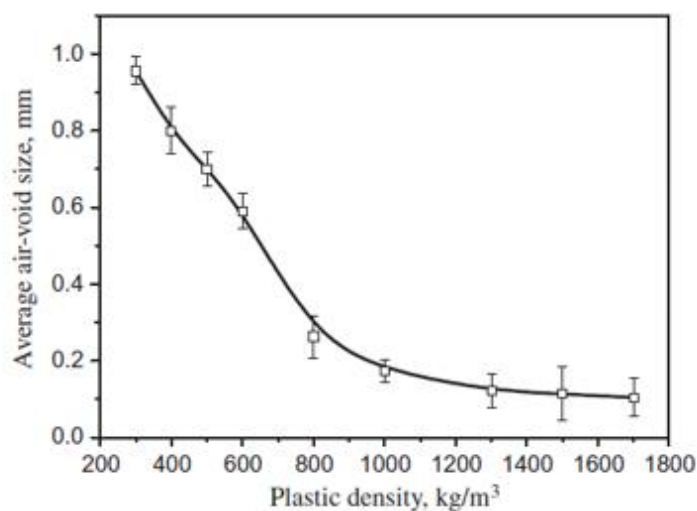


Figure 2-3: Relationship between average air void size and plastic density LWFC

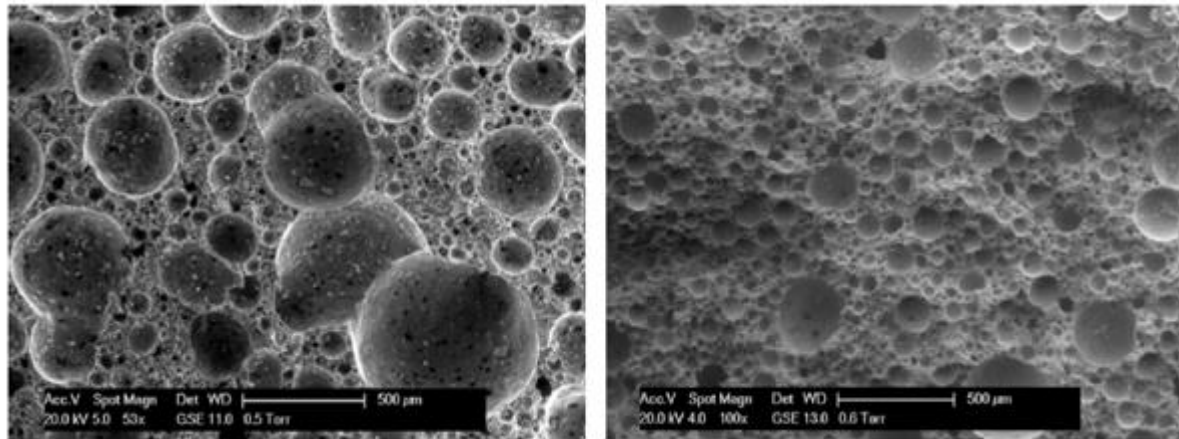


Figure 2-4: SEM Images of 500 kg/m³(left) and 1000 kg/m³(right) LWFC

2.1.3.3 Air Void Size Distribution

As not all air voids entrained in LWFC mixes are of equal size and the information provided in Section 2.1.3.2 pertains to average void sizes, it is also essential to discuss the pore size distribution when discussing LWFC microstructure properties. In an interesting study conducted by (Hilal *et al.*, 2015b), the effects of pore size distribution have been investigated and isolated by measuring the variance in pore size both in the aqueous pre-formed foam before addition to the base mix and also after addition as a LWFC specimen. A bitumen emulsion has been used to ensure that the aqueous foam may be accurately scanned, measured and compared to the hardened LWFC samples. In this study it has been uncovered that the size and size distribution of air voids in the foam on its own and once incorporated into the base mix vary. It has been discovered that in the foam on its own, void sizes vary from 100 µm to 875 µm with a median of approximately 325 µm and membrane thickness of 100µm, whereas voids once combined with the base mortar mix vary from 20 µm to 1950 µm. There are two important conclusions drawn from this data, the first of these is that LWFC presents with larger air voids than foam on its own which has been attributed to coalescence. The second interesting thing to note is that whilst the smallest bubble sizes recorded in the foam alone are rarely below 100 µm, there are a much larger percentage of air voids present in the LWFC sample which are below this threshold. As a matter of fact, it has been noted that about only twenty percent of voids present in the foam are smaller than 100 µm whilst approximately thirty to forty percent of voids in the LWFC mix are smaller than this value. It is theorised that this may be due to void distension caused by the mixing process and that researchers may have been severely overestimating the average size of air voids present in hardened LWFC mixes.

Figure 2-6 a, b and c indicate SEM images of 1300 kg/m³, 1600 kg/m³ and 1900 kg/m³ LWFC mixes respectively. This figure not only visually portrays the findings of greater void coalescence in less dense mixes, but also indicates the greater variation in pore size distributions experienced by less dense mixes. In addition to this, Figure 2-7 adapted from (Wei *et al.*, 2013) indicates the log-normal frequency

distribution graphs of 1700 kg/m³, 800 kg/m³ and 300 kg/m³ LWFC mixes. It should be noted that the majority of air voids in all mixes are of approximately the same size, however, the distribution is more uniform for denser mixes attributed the smaller quantity of larger coalesced voids previously mentioned.

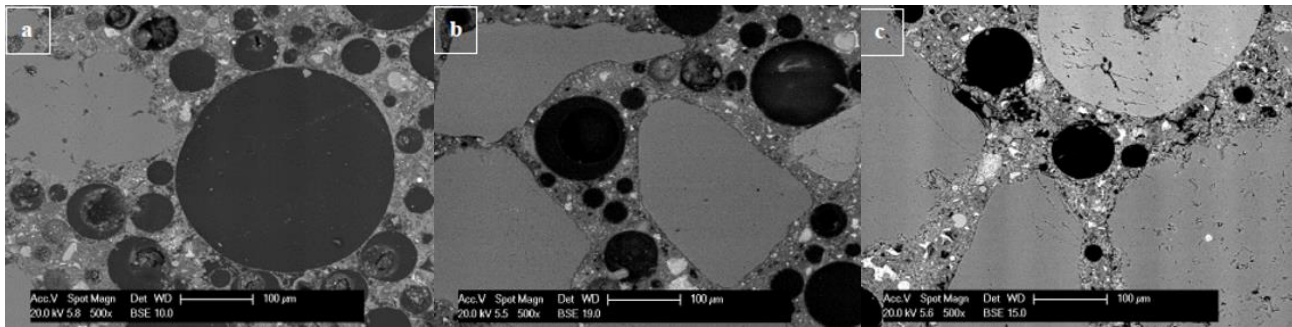


Figure 2-5: SEM Images of 1300 kg/m³, 1600 kg/m³ and 1900 kg/m³ LWFC

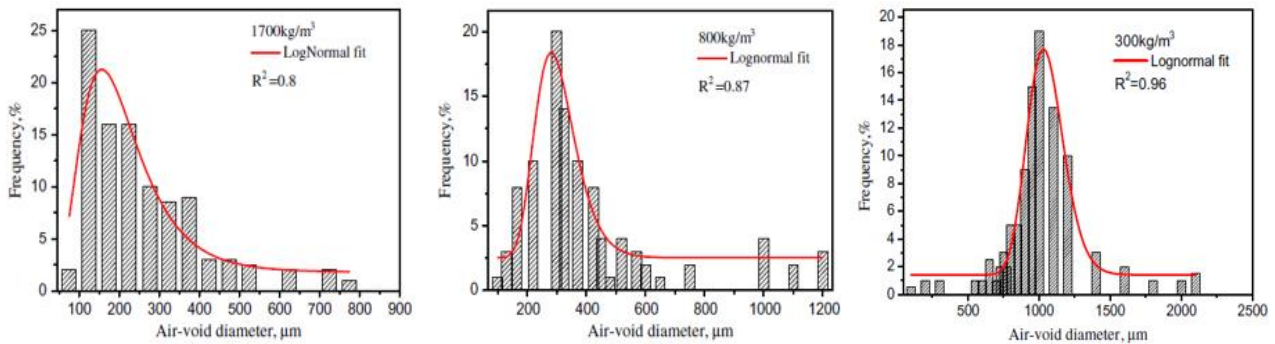


Figure 2-6: Log-normal frequency distributions for void sizes in 1700 kg/m³, 800 kg/m³ and 300 kg/m³ LWFC

2.1.4 Mix Design

As LWFC mixes are designed for a target plastic density and are void of any coarse aggregates, typical concrete mix design procedures cannot be utilised. Numerous different mix design approaches tailored specifically for LWFC have been put forward in various literature, however, the method laid out in the works of (Kearsley & Mostert, 2005) appears to be the most widely accepted. This approach, much like many other LWFC mix design methods, relies upon expressing individual constituents such as sand, FA, GGBS and SF as a fraction of the cement content by weight. A target density together with relevant constituent ratios should be chosen and specified and the cement content as well as the foam content may then be solved for simultaneously using two separate equations. Equation 2.5 is utilised to determine the mass of cement and is reliant on the sum of the mass of the individual constituents whilst Equation 2.6 utilised to determine the total volume of foam required to achieve the specified density and is reliant on the sum of the volume of the individual constituents.

$$\rho_{LWFC} = x_c + x_c \left(\frac{W}{C}\right) + x_c \left(\frac{a}{C}\right) + x_c \left(\frac{S}{C}\right) + x_c \left(\frac{a}{C}\right) \left(\frac{W}{a}\right) + x_c \left(\frac{S}{C}\right) \left(\frac{W}{S}\right) + RD_f V_f \quad (\text{Equation 2.5})$$

$$1000 = \frac{x_c}{RD_c} + x_c \left(\frac{w}{c}\right) + \frac{x_c \left(\frac{a}{c}\right)}{RD_a} + \frac{x_c \left(\frac{s}{c}\right)}{RD_s} + x_c \left(\frac{a}{c}\right) \left(\frac{w}{a}\right) + x_c \left(\frac{s}{c}\right) \left(\frac{w}{s}\right) + V_f \quad (\text{Equation 2.6})$$

In addition to the Equation 2.5 and Equation 2.6, Equation 2.7 has been developed as a means of estimating the required plastic casting density in order to attain a desired cured density. As it has only been developed using a restricted amount of samples its use is limited, however, it may be used as a rough approximation.

$$\rho_{LWFC} = 1.034 \cdot \rho_{dry} + 101.96 \quad (\text{Equation 2.7})$$

2.2 Shrinkage and Creep of Concrete

2.2.1 Introduction

The concept of concrete shrinkage and creep was first revealed in the year 1907, however, the first comprehensive research conducted on the topic brought about by the construction of long span concrete arch dams was not performed until the 1930s. This was later followed by another spike in interest during the 1970s and 1980s necessitated by the boom in construction of pre-stress concrete nuclear pressure vessels. The topic has always been of great interest within the engineering community as a means of predicting and minimising the long term deformations associated with damage and failure, and is currently of great interest today as a means of improving concrete durability (Bažant, 2013).

Shrinkage and creep are two phenomena which have been known about for decades, however, the task of understanding their exact causes and mechanisms is something made more difficult by the complexity of concrete as a material and something which still troubles researchers today. Numerous nonlinear effects, changing material properties with time due to internal hydration reactions and irregular moisture diffusion are all factors contributing to the increased analysis complexity of concrete over and above other conventional construction materials such as steel.

There have been countless research papers published over the years and whilst it is not an exact science, it is generally accepted that both creep and shrinkage of concrete are affected by similar factors and thus, should be addressed together. According to (Mehta & Monteiro, 2006), shrinkage and creep both share their origins within the hardened cement paste, there is a partial reversibility associated with the resulting strains, the evolution of the deformations is similar and follows a similar curve and the acting mechanisms usually do so in a similar way. When addressing the topic of shrinkage and creep in concrete, it is important to introduce two general concepts. The volumetric stress-independent deformation due to changes in water content with time is generally referred to as shrinkage whilst creep can be summarised as the volumetric stress-dependent deformation of a concrete sample under sustained loading with time (Bažant, 2013). Distinguishing between the stress-dependent and stress-independent concepts is

imperative as creep is generally understood as the difference in volumetric deformation between a loaded and unloaded specimen of concrete exposed to the same climatic conditions.

2.2.2 Measuring Shrinkage and Creep

There are currently many different theoretical models for the prediction of shrinkage and creep of concrete, all of which rely on data obtained from hundreds of physical tests performed on countless variations of concrete specimens under countless climatic conditions. One such example of a database used for the calibration of theoretical prediction models is that of the NU-ITI database which has been compiled by the Infrastructure Technology Institute of Northwestern University (Bažant & Li, 2008). This database comprises of physical test results obtained from 621 creep tests and 490 shrinkage tests.

The investigation of shrinkage and creep in concrete is typically approached from two different angles. The first of these is the physical measurement of creep and shrinkage values on concrete specimens whilst the second approach is that of investigating the physical properties of water near solid surfaces and other characteristics in the microstructure of the xerogel in the hardened cement paste. However, due to the fundamental complexities associated with concrete as a material, neither the microscopic nor the macroscopic approach are sufficient to truly understand the full magnitude of the complexities associated with the mechanisms involved in shrinkage and creep (Wittman, 1982).

Whilst it is possible to describe some physically relevant mechanisms associated with the phenomena, so-called apparent mechanisms such as crack formation and internal stress states do modify the time dependent deformation to a large degree and their effects on shrinkage and creep have proven difficult to fully understand.

2.2.3 Shrinkage and Creep Elements

As mentioned previously, one of the most commonly agreed-upon facts about shrinkage and creep of concrete is that they share their origin within the hardened cement paste. In particular, it is believed that the primary cause of these phenomena is the migration through and loss of water from within this hardened paste. It is also important to point out that whilst shrinkage and creep share this mechanism, the driving forces behind them are quite different. In the case of shrinkage, the driving force behind the migration and loss of internal water is attributed to a difference in the hygral equilibrium between the concrete and surrounding environment whilst, in the case of creep this driving force is attributed to the applied stress and internally generated forces. With this distinction made, it is possible to delve into the processes involved in this moisture migration and in doing so, the topic of voids and capillary water within the hardened cement paste must be addressed.

2.2.3.1 Voids and Capillary Water

As mentioned in Section 2.1.2.1, the hydration of tri-calcium silicate with water results in the formation of calcium-silicate hydrate (C-S-H) crystals. Interlayer spaces and capillary pores exist between these C-

S-H crystals which research has shown may account for up to 28% of the porosity in solid C-S-H (Mehta & Monteiro, 2006). Whilst capillary pores are not uncommon in hardened cement paste, larger macropores with diameters larger than 50nm are believed to contribute more towards strength and permeability whilst smaller micropores with diameters between 5nm-50nm are believed to play a more important role in creep and shrinkage. It is, however, the water contained within these macropores and micropores which is of more importance than the pores themselves.

Following this, it is imperative that this capillary water be classified separately insuring that their influence on creep and shrinkage is better understood. Free water contained in macropores is of less importance as its migration and loss has a negligible effect on creep and shrinkage, however, the loss and migration of water contained in micropores held by capillary tension and hydrogen bonding is believed to contribute to shrinkage and creep of concrete. Figure 2-8 adapted from (Mehta & Monteiro, 2006) is provided as a visual aid in explaining the concept of the different types of water contained in and around the hardened C-S-H. It visually indicates how water contained within hydrated cement paste is capable of existing in different forms and are classified by the degree of ease with which they can be removed.

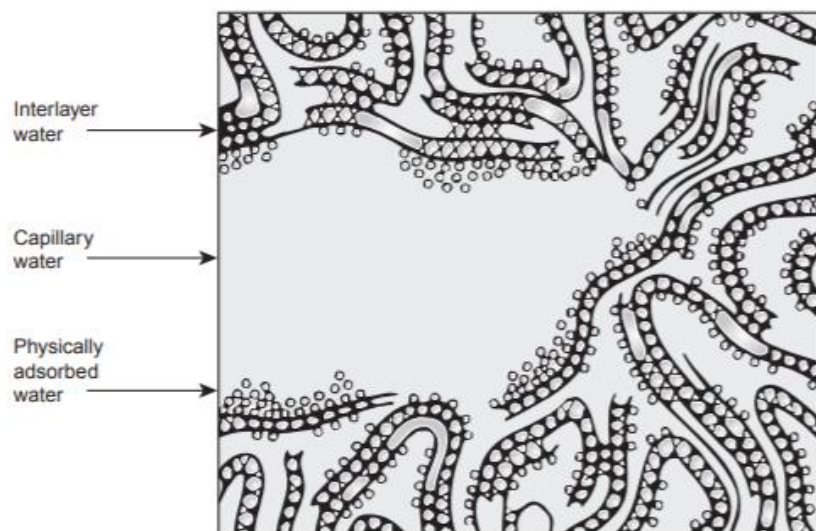


Figure 2-7: Graphic indicating different forms of water held in hardened cement paste

2.2.3.2 Moisture Loss

In conditions where the relative humidity of the environment surrounding a concrete specimen is equal to one-hundred percent, there is no loss of water from the concrete to the environment and a homogenous moisture equilibrium is maintained. In such cases, internal hydration reactions result in autogenous shrinkage which may usually be neglected whilst basic creep arising from internal moisture migration due to the applied stress results in all points within the cross-section exhibiting the same behaviour and thus, creep may be considered as a fundamental material property.

In conditions where the relative humidity of the surrounding environment falls below one-hundred percent, concrete specimens are subject to drying shrinkage and drying creep. In such conditions, free water held in macropores is able to migrate through the hardened cement paste and escape into the environment. As this free water is not attached to the microstructure of the hydration products by any physical or chemical bond, its loss is not accompanied by any volumetric change of the hardened cement paste itself. It follows from this, that a saturated and hydrated cement paste is capable of losing a considerable amount of free water without experiencing any drying shrinkage or creep. Such behaviour is shown by line A-B in Figure 2-9 adapted from (Mehta & Monteiro, 2006).

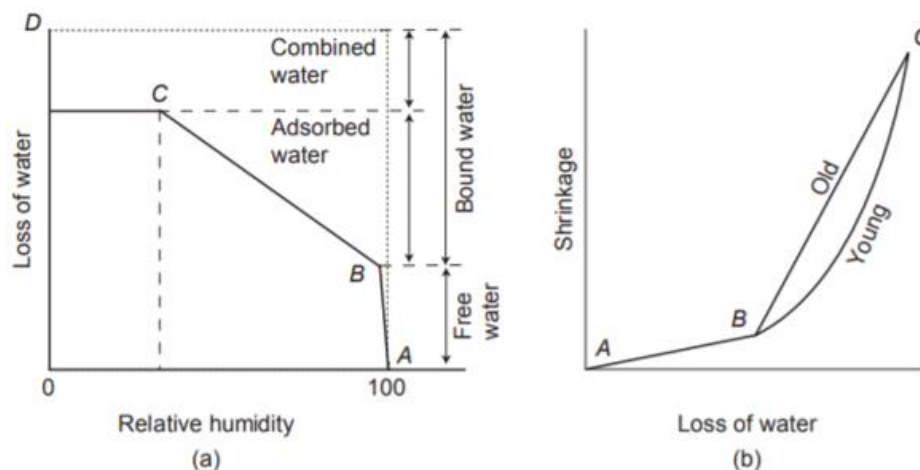


Figure 2-8: Relationship between ambient relative humidity and moisture loss in concrete

Upon further drying of a concrete specimen once the majority of the free water held in the macropores has been evaporated, a considerable amount of shrinkage is able to take place. As seen by line B-C in Figure 2-9, this occurs due to the loss of physically and chemically bonded water particles within the micropores of the hardened paste. Research on the microstructure of saturated hardened cement pastes has indicated that absorbed water is responsible for the generation of disjoining pressures when confined between two narrow solid surfaces. Removal of this confined water results in a reduction of net disjoining pressure between solid surfaces which in turn results in a volumetric decrease and shrinkage of the system. It is also possible under extreme drying conditions to remove the interlayer water present as a monomolecular water film within the C-S-H structure. This is possible only under extreme conditions as the higher contact area of the interlayer water with the solid surfaces and the tortuosity of transport paths calls for much stronger driving forces to migrate water particles through and out of the hardened paste.

It is important to note again that the same mechanisms responsible for drying shrinkage are responsible for creep. Whereas hygral inequality is the driving force responsible for moisture migration in drying shrinkage, continued external stress becomes the driving force for water held in micropores under creep conditions, thus it is logical to conclude that creep strains may occur even at conditions of one-hundred percent relative humidity.

2.2.3.3 Non-linear Mechanisms

It is generally agreed upon amongst researchers that there are additional factors at play apart from the loss of physically absorbed water that contribute to the phenomenon of creep. Concrete is unique in this behaviour in the sense that when exposed to applied stresses in the range of service levels (30%-40% of the ultimate compressive strength) it exhibits a linear creep behaviour. However, at applied stress in excess of 40% of the ultimate compressive strength, there are numerous non-linear effects which come into play and increase the total amount of creep exhibited and the complexity of the analysis. One such example of these non-linear effects is the micro-cracking experienced at the interfacial transition zone (ITZ) between aggregate particles and hardened cement paste.

Another interesting non-linear effect which has been noted is that of the delayed elastic response of concrete under creep conditions. As concrete is loaded over an extended period of time there is a tendency for the total stress on the cement paste to decrease, this has been attributed to the bond behaviour of aggregates and hardened cement paste. Under sustained loading, internal loads are gradually transferred from the cement paste to the aggregate particles. This results in a gradual decrease of the stresses imparted on the hardened cement paste whilst the stresses experienced by the aggregate particles gradually increase, it is also important to note that aggregate particles which have much higher stiffness's than hardened cement paste deform elastically under increased loading.

2.2.3.4 Reversibility

Another important characteristic to discuss when addressing the topic of creep and shrinkage of concrete is that of reversibility. To aid in this explanation, Figure 2-10 and Figure 2-11 are provided from (Mehta & Monteiro, 2006) and indicate typical drying shrinkage and drying creep behaviour curves for conditions of drying and wetting and loading and unloading respectively. Partial reversibility, which is another characteristic both creep and shrinkage have in common, is of great importance when bearing in mind practical design considerations. When investigating Figure 2-10 which indicates typical drying shrinkage behaviour, it is important to notice that as concrete does not return to its original dimensions upon rewetting, a distinction must be made between reversible and irreversible shrinkage. By definition, reversible shrinkage is the portion of total shrinkage that is recoverable and reproducible upon subsequent wet-dry cycles, whilst irreversible shrinkage is the portion of total shrinkage that occurs upon first drying and cannot be recovered upon subsequent wet-dry cycles. Whilst reversible shrinkage is believed to be attributed to the rehydration of cement particles and capillary pores, it is believed that irreversible shrinkage may be as a result of secondary reactions that occur within the C-S-H structure as a consequence of dehydration.

When turning attention to Figure 2-11 which indicates typical drying creep behaviour upon loading and unloading cycles, it may be seen that upon unloading there is a degree of elastic recovery which is of approximately the same order as the deflection upon initial loading. This immediate elastic recovery is then followed by a gradual decrease in total strain which is commonly referred to as creep recovery. Whilst creep recovery is known to occur over a much shorter time period than the initial drying creep, its reversibility is not complete. Much like is done with drying shrinkage behaviour, a distinction must be made between reversible and irreversible creep. It is believed that a portion of the reversible creep may be attributed to the delayed elastic response of the aggregates and cement paste as mentioned earlier, whilst non-linear deformations in the hardened cement paste are not recoverable. The elastic deformations of the stiffer aggregates is completely recoverable.

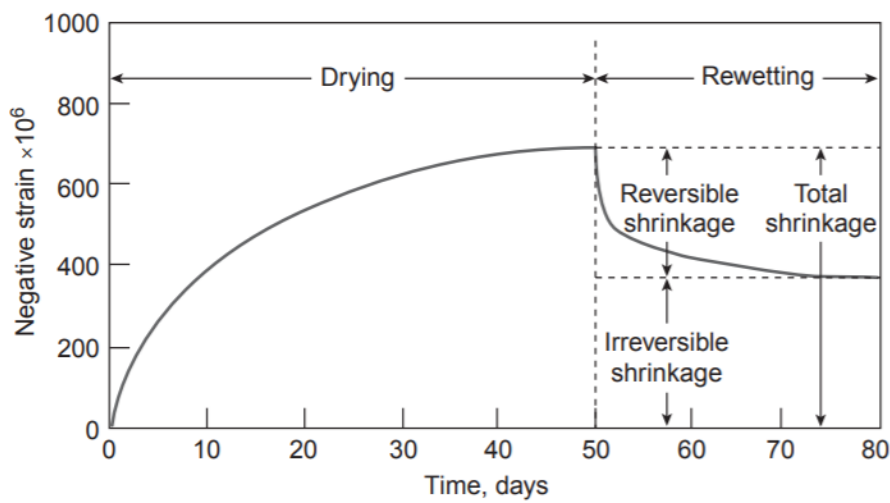


Figure 2-9: Typical drying shrinkage curve for concrete

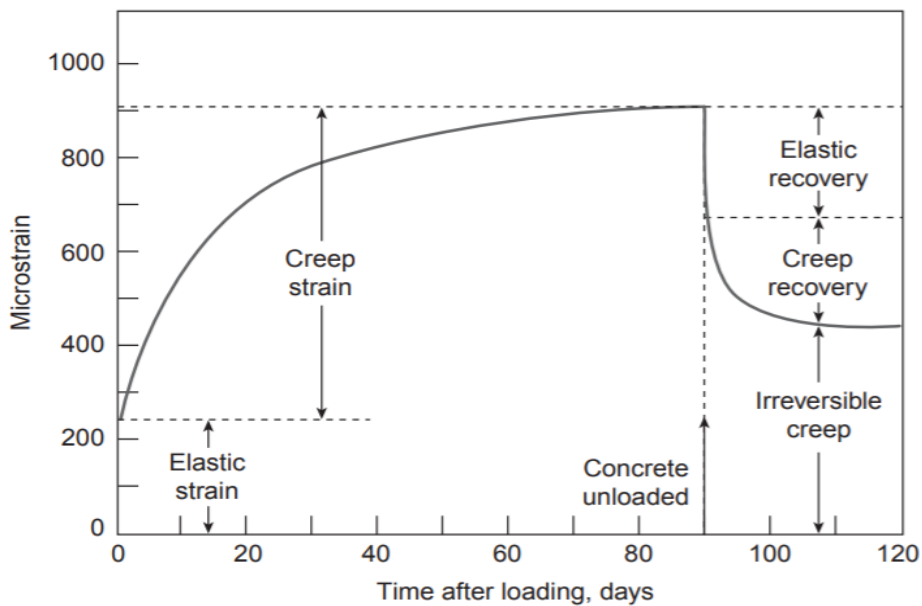


Figure 2-10: Typical drying creep curve for concrete

2.3 Shrinkage and Creep of LWFC

2.3.1 Introduction

The creep and shrinkage behaviour of concrete is caused predominantly by the same mechanisms. The most prominent of which include the moisture removal from the physically absorbed water held within the micropores of the hardened cement paste a host of non-linear effects such as aggregate-paste interaction and micro-cracking. There have been many papers written on the magnitude and causes of creep and shrinkage of aerated concretes such as (Narayanan & Ramamurthy, 2000), however, the literature available on the creep and shrinkage behaviour of LWFC specifically appears to be severely limited.

A number of different research efforts on the topic have yielded results which indicate that the creep and shrinkage values of LWFC are significantly higher than equivalent NWC – somewhere in the order of four to ten times higher (Nambiar, 2014). Factors such as concrete composition, density, moisture content, climate and microstructure properties have all been noted to influence the degree of creep and shrinkage. It is also interesting to note that one of the most common methods of reducing drying shrinkage and creep of aerated concretes is that of autoclave curing which results in a product known as Autoclaved Aerated Concrete (AAC). This reduction in creep and shrinkage of AAC samples may corroborate what has been previously mentioned that creep and shrinkage are likely to be functions of the hydration products resulting from the hydration of Portland cement and the formation of hardened C-S-H. Autoclaving both minimises moisture loss and promotes faster setting which when combined, drastically reduce the volumetric deformation of specimens. Comparative studies have been done comparing the drying shrinkage behaviour of LWFC containing different fillers, foam volumes, moisture contents, synthetic fibres as well as glycol compounds, the results of which are discussed in Section 2.3.2 – Section 2.3.6.

2.3.2 Effects of Fillers

In a study performed by (Nambiar, 2014), the drying shrinkage behaviour of control LWFC was compared to mixes containing different percentages of fillers such as sand and fly ash. It was shown that for all filler-cement ratios for both the sand and fly ash mixes, the resulting drying shrinkage was reduced compared to the control LWFC mixture which contained only Portland cement. This was attributed to a number of factors, all of which have been previously mentioned in the preceding sections describing the mechanisms involved in creep and shrinkage of concrete.

The replacement of Portland cement with fillers such as sand and fly ash results in the reduction of the total volume of cement powder present in the mix. As the hydration of Portland cement is responsible for the formation of C-S-H, micropores and water absorption, reducing the total amount of cement reduces the total amount of hardened cement paste, solid C-S-H and total absorbed water, thus reducing the loss of absorbed water and reducing shrinkage. Additionally, the smaller shrinkage values, particularly for the

mixes containing sand, may be attributed to the higher shrinkage straining capacity of the stiffer sand particles. This observation is shown graphically in Figure 2-12 adapted from (Nambiar, 2014) for a constant foam volume.

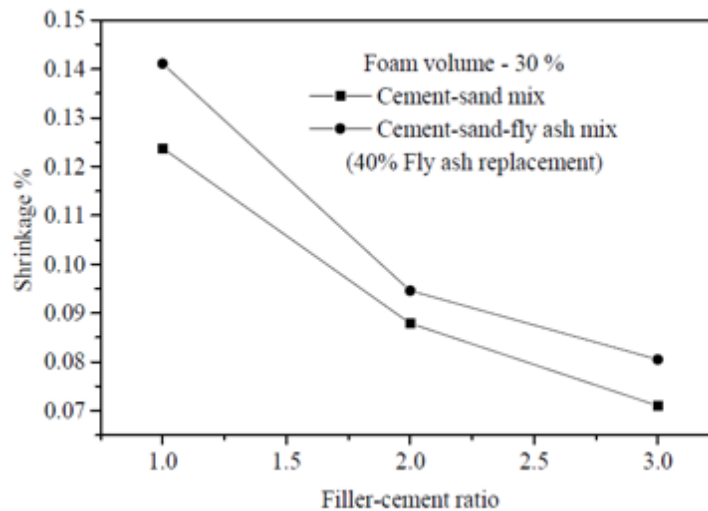


Figure 2-11: LWFC drying shrinkage strains for mixes containing sand and fly ash

It has been noted, however, that an increase in the percentage of fly ash in the mix did result in higher shrinkage values, although still lower than the control mix. Mixes with one hundred percent fly ash replacement exhibited on average thirty one percent more shrinkage than the equivalent replacement with sand. In addition to the higher shrinkage restraining capacity of sand previously mentioned, mixes with fly ash generally require a greater amount of water in order to achieve a stable and workable mix. By increasing the water demand of a mix, the total amount of water absorbed and available for later evaporation is increased, thus resulting in higher shrinkage.

It is also known that mixes containing fly ash generally require a longer amount of time to fully cure and harden. The result of increasing this setting time also allows for a longer period of time where unhydrated and partially hydrated water molecules are able to migrate and escape from the concrete specimen (Hilal *et al.*, 2015). The increase in shrinkage values accompanied by increasing the percentage of fly ash in the mix is shown in Figure 2-13. It should still be noted that whilst increasing the fly ash percentage does increase the total shrinkage, the values observed are still lower than the control LWFC mix.

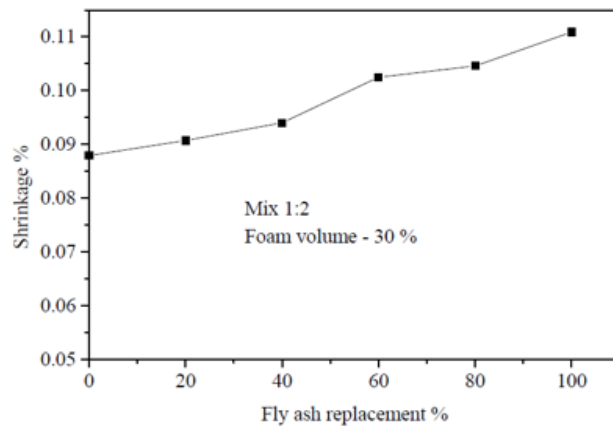


Figure 2-12: Drying shrinkage strains for LWFC with varying replacement of fly ash

2.3.3 Effects of Foam Volume

As foam volume would seem to be the leading factor in the creep and shrinkage of LWFC, its complexity is not of the magnitude that would be expected. Shown in Figure 2-14 and Figure 2-15 adapted from (Nambiar, 2014), it can be seen that for both cement-sand and cement-fly ash mixes the total shrinkage exhibited increases with a decrease in total foam volume. Whilst this may seem counter-intuitive at first, this agrees with the microstructure theories previously discussed. Pores created during the making of LWFC are of the size that they do not fall into the micropore category. Macropores which are regularly spaced and not inter-connected are not responsible for the absorption of water responsible for creep and shrinkage but rather play a role in properties such as strength and durability.

Yet again, the total volume of hardened cement paste and aggregates present are identified as the leading cause of creep and shrinkage. As foam volume increase and decrease so decreases and increase the total amount of hardened cement paste and solid C-S-H present respectively. It has already been discussed how increasing and decreasing the total volume of these solids effects the creep and shrinkage behaviour and thus, the phenomenon of increased shrinkage with decreasing foam volume may be explained.

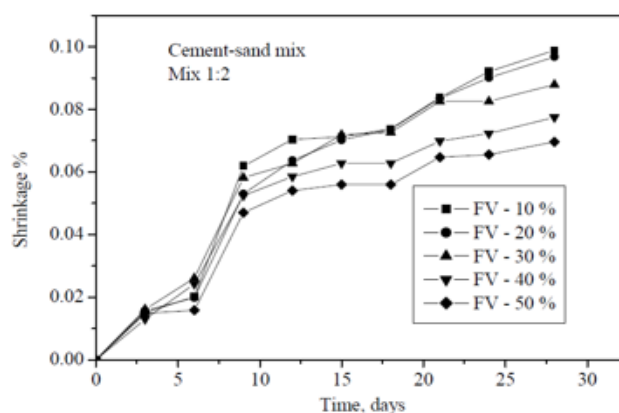


Figure 2-13: Drying shrinkage strains for LWFC containing sand with different foam volumes

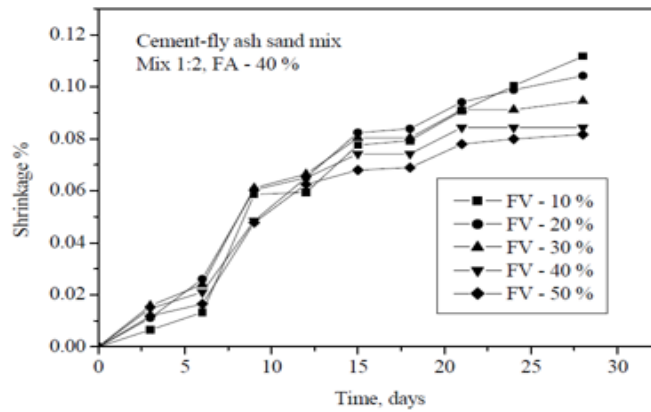


Figure 2-14: Drying shrinkage strains for LWFC containing fly ash and sand for different foam volumes

2.3.4 Effects of Moisture Content

Arguably the most important factor influencing creep and shrinkage of concrete is that of moisture content. The moisture content (absorbed water) and loss thereof is one of the key driving forces behind the phenomena of drying creep and drying shrinkage. Shown in Figure 2-16, it is possible to investigate to what extent the moisture content of LWFC has on its creep and shrinkage behaviour. When investigating mixes with different foam volumes it is possible to recognise that mixes with higher foam volumes possess lower moisture contents. This is as a result of higher foam volumes resulting in smaller hardened cement paste volumes which absorb less water. It may also be noted that mixes containing higher foam volumes exhibit faster drying than those with lower volumes. This is attributed to the fact that mixes with higher foam volumes possess smaller volumes of free water and thus, are dried completely over a shorter period of time.

It has been noted that both cement-sand and cement-fly ash mixes exhibited similar behaviour with respect to drying shrinkage and moisture content regardless of the foam volumes involved. In explaining the shapes of each graph, theory previously mentioned on the different forms in which water is held within hardened concrete should keep in mind. High moisture contents exhibit relatively low shrinkage attributed to the higher amount of free water which is able to migrate and evaporate from macropores without resulting in a considerable volume reduction. When moving towards lower moisture contents, it may be seen that a steady increase in the total amount of drying shrinkage is exhibited. In this stage, as mentioned in previous sections, the free water has been used up and absorbed water within smaller micropores begins to migrate and evaporate due to a larger hygral inequilibrium. The removal of this water from micropores is what results in a volume reduction of the hardened cement paste and the onset of drying shrinkage. In the lower portions of the graphs (below three percent moisture) a sharp increase in the total amount of shrinkage may be seen. Under continued and extreme drying, the interlayer water held as a monomolecular water film between hardened C-S-H may be removed. It is in these extreme conditions under immense hygral equilibrium that virtually all capillary water is removed and extreme shrinkage occurs.

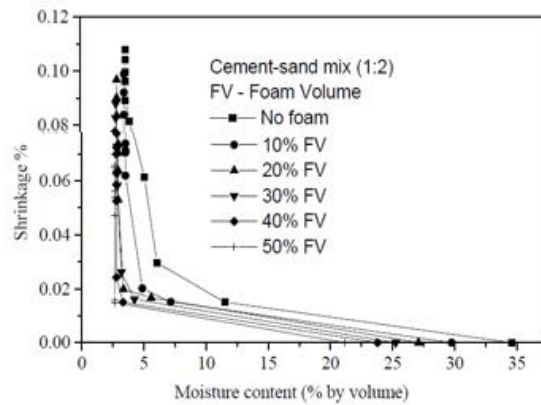


Figure 2-15: Relationship between drying shrinkage and moisture content for LWFC containing sand

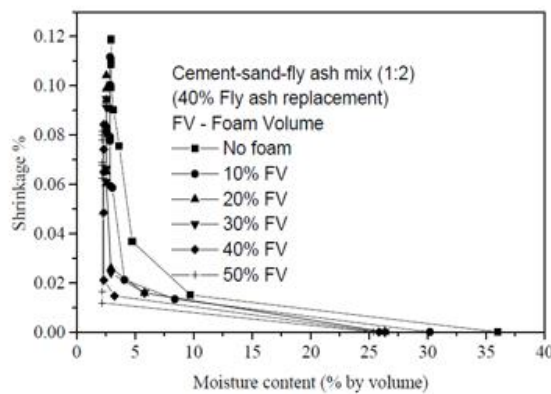


Figure 2-16: Relationship between drying shrinkage and moisture content for LWFC containing sand and fly ash

2.3.5 Effects of Glycol Compounds

One of the most common methods of reducing the drying shrinkage and creep behaviour of NWC is the use of shrinkage reducing agents (SRA). Whilst this is an effective method of minimising the effects of drying shrinkage and creep in NWC, its use in LWFC has been limited due to its unfavourable interaction with surfactant molecules resulting in foam degradation. The exact mechanisms associated with the phenomena are complicated, however, it is commonly understood that one of the leading mechanisms is the surface tension and ease with which physically absorbed water within the hardened cement paste can be removed. Chain molecules of glycol compounds are known to possess surface tension reducing properties and it is for this reason that (Chindapasirt & Rattanasak, 2011) investigated the effects of including three different glycol compounds in typical LWFC containing fly ash.

The three glycol compounds investigated were that of commercial propylene glycol (PG), tri-ethylene glycol (TEG) and di-propylene glycol tert-butyl-ether (DPTE) shown graphically in (a), (b) and (c) in Figure 2-18 respectively. Chemical compounds which contain two hydroxyl groups (OH) are known as diols or glycols and are known to aid in high water solubility. In addition to this, they are also known to be hydrophilic and attract water from the surrounding medium through either absorption or adsorption.

By referring to Figure 2-18 adapted from (Chindapasirt & Rattanasak, 2011), it may be seen that TEG is a longer chain molecule and more polar than that of PG and DPTE. This polarity is attributed to the presence of both the (O) and (OH) hydroxyl groups and thus, TEG is more commonly used as a plasticiser.

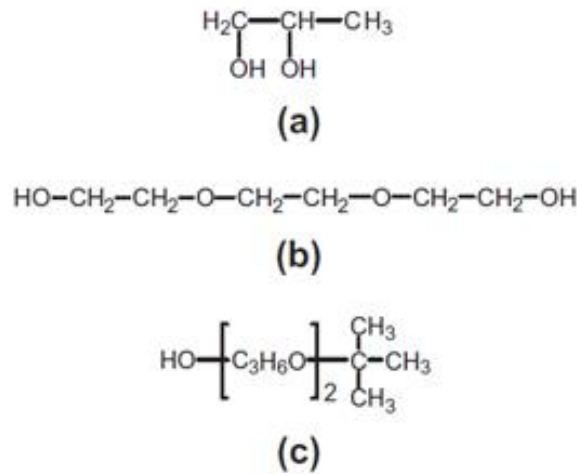


Figure 2-17: Chemical structures of PG (a), TEG (b) and DPTE (c)

Figure 2-19 adapted from (Chindapasirt & Rattanasak, 2011) indicates the physical shrinkage results obtained for the mixes including the three glycol compounds and a control mix containing only fly ash. It may be seen that the drying shrinkage values for the control LWFC are in the range of approximately 2450 microstrain. It should also be noted that the shrinkage range for typical mortars is approximately 800-2000 microstrain which again emphasises the need for some sort of SRA. It may be seen that over the entire testing period, all mixes containing glycol compounds exhibit far less drying shrinkage (1520, 1430 and 1060 microstrain for PG, TEG and DPTE respectively). It was noted, however, that whilst DPTE appears to have the most profound effect of drying shrinkage, it resulted in foam degradation and accelerated setting times.

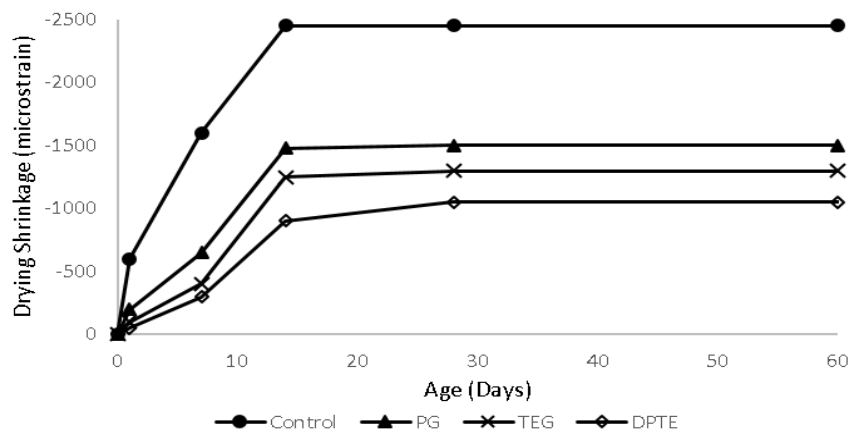


Figure 2-18: Drying shrinkage strains for LWFC containing glycol compounds

2.3.6 Effects of Fibre Reinforcement

In a study conducted by (Roslan, Awang & Mydin, 2012), the effects of different percentages of additives on drying shrinkage of LWFC has been investigated. The paper investigates the inclusion of additives such as fly ash, lime and polypropylene fibres. It has been found that whilst fly ash and lime do not contribute positively to the reduction of drying shrinkage strains, the inclusion of polypropylene fibres does. By investigating Figure 2-20, the effects that the various additives have on the total drying shrinkage strains may be seen. Values for the control LWFC of approximately 0.1-0.3% are between four to ten times higher than drying shrinkage strains recorded for equivalent NWC. The Figure also indicates that a 0.4% (PF40-C) and 0.2% (PF20-C) inclusion of polypropylene fibres significantly improves the drying shrinkage behaviour of the LWFC. It is believed that this improvement may be attributed to the ability of polypropylene fibres to bridge gaps and prevent the formation and propagation of microcracks which is one of the non-linear effects contributing to the phenomena of creep and shrinkage in concrete.

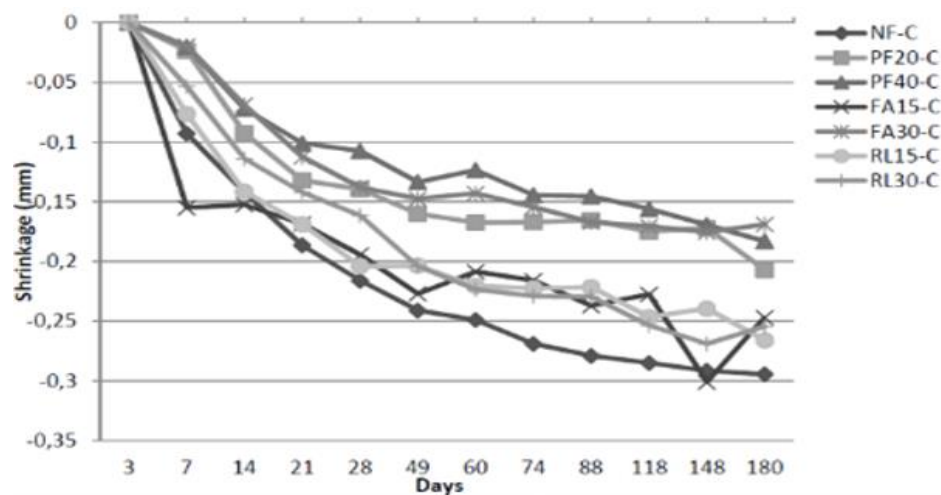


Figure 2-19: Drying shrinkage strains for LWFC mixes containing different percentages of fillers and fibres

2.4 Existing Numerical Models

The phenomena of creep and shrinkage in concrete have been known about for decades and there are currently numerous different standards which include dedicated sections for the prediction of creep and shrinkage strains in both NWC and LWAC. As there are currently no standards that include prediction models for the creep and shrinkage strains in LWFC, three of the most common and widely accepted international standards are investigated, implemented and their results compared to test data obtained from physical samples and finite element modelling. The intention is to investigate to what extent these existing models are able to predict the actual creep and shrinkage behaviour of LWFC and if required, determine what adjustments need to be made to these models to account for the increased creep and shrinkage strains in LWFC. The three chosen models are that of the Model Code 2010, EN 1992-1-1 (2004) and the Rilem Model B3. The sections that follow provide a brief background of each standard as well as information relating to how creep and shrinkage strains are defined and estimated.

2.4.1 Fib Model Code 2010

The International Federation for Structural Concrete (*fib*) has been publishing pioneering work in codification since the early 1970's. The most recent of these specifications first published in 2012 is that of the Model Code 2010 (MC2010), which has been developed over the last ten years through a collaboration of no less than 44 countries. The MC2010 includes the whole life-cycle of a concrete structure with specific sections for shrinkage and creep predictions. The total strain at a time t , $\varepsilon_c(t)$, of a concrete member loaded uni-axially at a time t_0 with a constant stress $\sigma_c(t_0)$ is as follows:

$$\varepsilon_c(t) = \varepsilon_{ci}(t_0) + \varepsilon_{cc}(t) + \varepsilon_{cas}(t) + \varepsilon_{cT}(t) \quad (\text{Equation 2.8})$$

The total strain in MC2010 is attributed to the initial strain at loading (ε_{ci}), creep strain (ε_{cc}), shrinkage strain (ε_{cs}) and thermal strain (ε_{cT}) respectively. For the purpose of this research only the initial, creep and shrinkage strains are discussed. The initial strain at loading together with the creep strain attributed to basic and drying creep as well as the shrinkage strain attributed to autogenous and drying shrinkage are expanded from Eq. 2.8 and expressed in Eq. 2.9 and Eq. 2.10

$$\varepsilon_c(t) = \varepsilon_{ci}(t_0) + \varepsilon_{cc}(t) + \varepsilon_{cas}(t) + \varepsilon_{cds}(t, t_s) \quad (\text{Equation 2.9})$$

$$\varepsilon_c(t) = \frac{\sigma_c(t_0)}{E_{28}} + \frac{\sigma_c(t_0)}{E_{28}} [\varphi_{bc}(t, t_0) + \varphi_{dc}(t, t_0)] + \varepsilon_{cas}(t) + \varepsilon_{cds}(t, t_s) \quad (\text{Equation 2.10})$$

Where:

- $\varepsilon_{ci}(t_0)$ = Initial strain at loading (t_0).
- $\varepsilon_{cc}(t)$ = Creep strain at time t .
- $\varepsilon_{cas}(t)$ = Autogenous shrinkage strain at time t .
- $\varepsilon_{cds}(t, t_s)$ = Drying shrinkage strain at time t after drying commences at time t_s .
- $\sigma_c(t_0)$ = Applied external stress at time of initial loading.
- E_{28} = Young's Modulus of concrete at 28 days age.
- φ_{bc} = Basic creep coefficient.
- φ_{dc} = Drying creep coefficient

2.4.1.1 Basic Creep

The basic creep coefficient is calculated as follows:

$$\varphi_{bc}(t, t_0) = \beta_{bc}(f_{cm}) \cdot \beta_{bc}(t, t_0) \quad (\text{Equation 2.11})$$

With:

$$\beta_{bc}(f_{cm}) = \frac{1.8}{(f_{cm})^{0.7}} \quad (\text{Equation 2.12})$$

$$\beta_{bc}(t, t_0) = \ln \left(\left(\frac{30}{t_{0,adj}} + 0.035 \right)^2 \cdot (t - t_0) + 1 \right) \quad (\text{Equation 2.13})$$

2.4.1.2 Drying Creep

The drying creep coefficient may be calculated as follows:

$$\varphi_{dc}(t, t_0) = \beta_{dc}(f_{cm}) \cdot \beta(RH) \cdot \beta_{dc}(t_0) \cdot \beta_{dc}(t, t_0) \quad (\text{Equation 2.14})$$

With:

$$\beta_{dc}(f_{cm}) = \frac{412}{(f_{cm})^{1.4}} \quad (\text{Equation 2.15})$$

$$\beta(RH) = \frac{1 - \frac{RH}{100}}{\sqrt[3]{0.1 \cdot \frac{h}{100}}} \quad (\text{Equation 2.16})$$

$$\beta_{dc}(t_0) = \frac{1}{0.1 + t_{0,adj}^{0.2}} \quad (\text{Equation 2.17})$$

$$\beta_{dc}(t, t_0) = \left[\frac{(t - t_0)}{\beta_h + (t - t_0)} \right]^{\gamma(t_0)} \quad (\text{Equation 2.18})$$

With:

$$\gamma(t_0) = \frac{1}{2.3 + \frac{3.5}{\sqrt{t_{0,adj}}}} \quad (\text{Equation 2.19})$$

$$\beta_h = 1.5h + 250\alpha_{f_{cm}} \leq 1500\alpha_{f_{cm}} \quad (\text{Equation 2.20})$$

$$\alpha_{f_{cm}} = \left(\frac{35}{f_{cm}} \right)^{0.5} \quad (\text{Equation 2.21})$$

Where:

- f_{cm} = Mean compressive strength at an age of 28 days in MPa.
- RH = Relative Humidity of ambient environment in %
- h = Notional size of the member (2*area/perimeter)

2.4.1.3 Adjusting Creep for LWAC

For LWAC the standard creep coefficient may be adjusted as follows:

$$\varphi_1 = \eta_E \cdot \varphi(t, t_0) \quad (\text{Equation 2.22})$$

Where:

- $\eta_E = (\rho/2200)^2$, with oven dry density ρ in (kg/m³)
- Concrete classes LC12/13 and LC16/18, this must be multiplied by an additional factor of 1.3.

2.4.1.4 Total Shrinkage

The total shrinkage strain may be expressed as the sum of the autogenous and drying shrinkage as follows:

$$\varepsilon_{sc}(t, t_s) = \varepsilon_{cas}(t) + \varepsilon_{cads}(t, t_s) \quad (\text{Equation 2.23})$$

2.4.1.5 Autogenous Shrinkage

The total autogenous shrinkage occurring under sealed conditions with no moisture transfer between the specimen and environment is expressed as follows:

$$\varepsilon_{cas}(t) = \varepsilon_{cas0}(f_{cm}) \cdot \beta_{as}(t) \quad (\text{Equation 2.24})$$

With:

$$\varepsilon_{cas0}(f_{cm}) = -\alpha_{as} \left(\frac{\frac{f_{cm}}{10}}{6 + \frac{f_{cm}}{10}} \right)^{2.5} \cdot (10^{-6}) \quad (\text{Equation 2.25})$$

$$\beta_{as}(t) = 1 - \exp(-0.2\sqrt{t}) \quad (\text{Equation 2.26})$$

Where:

- $\varepsilon_{cas0}(f_{cm})$ = Notional autogenous shrinkage coefficient.
- $\beta_{as}(t)$ = Autogenous shrinkage time function.
- t = Concrete age in days.
- f_{cm} = Mean compressive strength at an age of 28 days in MPa
- α_{as} = Coefficient dependent on type of cement shown by Table 2-5.

Table 2-5: Fib Cement Coefficients

Strength Class	α_{as}	α_{ds1}	α_{ds2}
32.5 N	800	3	0.013
32.5 R, 42.5 N	700	4	0.012
42.5 R, 52.5N, 52.5 R	600	6	0.012

2.4.1.6 Drying Shrinkage

The total amount of drying shrinkage experienced by a sample subjected to drying conditions is expressed as follows:

$$\varepsilon_{cds}(t, t_s) = \varepsilon_{cds0}(f_{cm}) \cdot \beta_{RH}(RH) \cdot \beta_{ds}(t - t_s) \quad (\text{Equation 2.27})$$

With:

$$\varepsilon_{cds0}(f_{cm}) = [(220 + 110 \cdot \alpha_{ds1}) \cdot \exp(-\alpha_{ds2} \cdot f_{cm})] \cdot 10^{-6} \quad (\text{Equation 2.28})$$

$$\beta_{RH} = -1.55 \cdot \left[1 - \left(\frac{RH}{100} \right)^3 \right] \quad 40\% \leq RH \leq 99\% \quad (\text{Equation 2.29})$$

$$\beta_{ds}(t - t_s) = \left(\frac{(t - t_s)}{0.035h^2 + (t - t_s)} \right)^{0.5} \quad (\text{Equation 2.30})$$

Where:

- $\varepsilon_{cds0}(f_{cm})$ = Notional drying shrinkage coefficient.
- β_{RH} = Ambient relative humidity coefficient.
- RH = Ambient relative humidity in %.
- t_s = Concrete age when drying commences in days.
- $(t-t_s)$ = The duration of drying in days.
- f_{cm} = Mean compressive strength at an age of 28 days in MPa.
- h = Notional size of the member (2*area/perimeter).
- α_{ds1} & α_{ds2} = Coefficients dependent on type of cement shown in Table 5.

2.4.1.7 Adjusting Shrinkage for LWAC

The shrinkage of LWAC may be calculated as follows:

$$\varepsilon_{lcs}(t, t_s) = \eta \cdot \varepsilon_{sc}(t, t_s) \quad (\text{Equation 2.31})$$

Where:

- $\eta = 1.5$ for LC8, LC12 and LC16 class concretes.
- $\eta = 1.2$ for LC20 and higher class concretes.

2.4.2 EN 1992-1-1 (2004)

The history of the Eurocodes programme stretches back to the 1980's, where after 15 years of development the first European codes were generated. The Eurocode 2 (EN 1992) specifically focusses on the design of concrete structures and much like the MC2010 provide standards applicable to the entire life-cycle of a structure including specific creep and shrinkage prediction sections

2.4.2.1 Total Creep

The total creep strain at time t of a uni-axially loaded specimen loaded with a constant force of σ_c at a time t_0 is expressed as:

$$\varepsilon_{cc}(t, t_0) = \varphi(t, t_0) \cdot \left(\frac{\sigma_c}{E_c} \right) \quad (\text{Equation 2.32})$$

With:

$$\varphi(t, t_0) = \varphi_0 \cdot \beta_c(t, t_0) \quad (\text{Equation 2.33})$$

$$\varphi_0 = \varphi_{RH} \cdot \beta(f_{cm}) \cdot \beta(t_0) \quad (\text{Equation 2.34})$$

$$\varphi_{RH} = 1 + \frac{1 - RH/100}{0.1 \sqrt[3]{h_0}} \quad (\text{Equation 2.35})$$

$$\beta(f_{cm}) = \frac{16.8}{\sqrt{f_{cm}}} \quad (\text{Equation 2.36})$$

$$\beta(t_0) = \frac{1}{(0.1 + t_0^{0.2})} \quad (\text{Equation 2.37})$$

$$\beta_c(t, t_0) = \left[\frac{(t - t_0)}{(\beta_H + t - t_0)} \right]^{0.3} \quad (\text{Equation 2.38})$$

$$\beta_H = 1.5[1 + (0.012RH)^{18}]h_0 + 250 \leq 1500 \quad (\text{Equation 2.39})$$

Where:

- φ_0 = Notional creep coefficient.
- φ_{RH} = Factor to allow for the effects of relative humidity.
- $\beta(f_{cm})$ = Factor to allow for the effects of concrete strength.
- $\beta(t_0)$ = Factor to allow for the effects of concrete age.
- $\beta_c(t, t_0)$ = Coefficient to describe the development of creep with time after loading.
- β_H = Factor to allow for the simultaneous effects of RH and notional size.
- RH = The relative humidity of the environment in %.
- f_{cm} = Mean compressive strength at an age of 28 days in MPa.

- h_0 = Notional size of the member ($2 \cdot \text{area}/\text{perimeter}$).
- t = Age of the concrete in days at the time considered.
- t_0 = Age of the concrete at the time of loading in days.
- $t-t_0$ = Non-adjusted age of loading in days.

2.4.2.2 Adjusting Creep for LWAC

Creep strains so derived as in Section 2.4.2.1 are to be multiplied by a factor η_2 :

Where:

- $\eta_2 = 1.3$ for $f_{cm} < \text{LC16/18}$
- $\eta_2 = 1.0$ for $f_{cm} > \text{LC20/22}$

2.4.2.3 Total Shrinkage

The total shrinkage strain is expressed as the sum of the autogenous and drying shrinkage strains. Drying shrinkage is said to develop slowly as it is a function of the migrating water through the hardened concrete whilst autogenous shrinkage develops during the hardening process. The total shrinkage is therefore expressed as:

$$\varepsilon_{cs} = \varepsilon_{cd} + \varepsilon_{ca} \quad (\text{Equation 2.40})$$

Where:

- ε_{cs} = The total shrinkage strain.
- ε_{cd} = The total drying shrinkage strain.
- ε_{ca} = The total autogenous shrinkage strain.

2.4.2.4 Autogenous Shrinkage

The autogenous shrinkage under sealed conditions may be expressed as:

$$\varepsilon_{ca}(t) = \beta_{as}(t)\varepsilon_{ca}(\infty) \quad (\text{Equation 2.41})$$

With:

$$\varepsilon_{ca}(\infty) = 2.5(f_{ck} - 10) \cdot 10^{-6} \quad (\text{Equation 2.42})$$

$$\beta_{as}(t) = 1 - \exp(-0.2t^{0.5}) \quad (\text{Equation 2.43})$$

2.4.2.5 Drying Shrinkage

It follows that the development of drying shrinkage strain with time is expressed as:

$$\varepsilon_{cd}(t) = \beta_{ds}(t, t_s) \cdot k_h \cdot \varepsilon_{cd0} \quad (\text{Equation 2.44})$$

With:

$$\beta_{ds}(t, t_s) = \frac{(t - t_s)}{(t - t_s) + 0.04 \sqrt{h_0}^3} \quad (\text{Equation 2.45})$$

Where:

- k_h = Coefficient dependent on notional size.
- t = Age of the concrete in days at the time considered.
- t_s = Age of concrete in days at the beginning of drying.
- h_0 = Notional size of the member ($2 \cdot \text{area} / \text{perimeter}$).

2.4.2.6 Adjusting Shrinkage for LWAC

Shrinkage strains so derived as in Section 2.4.2.3 are to be multiplied by a factor η_3 :

Where:

- $\eta_3 = 1.5$ for $f_{cm} < \text{LC16/18}$
- $\eta_3 = 1.2$ for $f_{cm} > \text{LC20/22}$

2.4.3 Rilem Model B3

The Rilem Model B3 first submitted to ACI Committee 209 in 1995, builds upon the methods set out in the CEB Model (1990) and the previous ACI 209 Model which was developed in the mid 1960's. This model is stated to have coefficients of variation which deviate from global sample data considerably less than those of the former and significantly less than those of the latter. The total strain at time $t > 0$ which represents the sum of the instantaneous deformation, basic creep and additional deformation due to drying is expressed as:

$$J(t, t') = q_1 + C_0(t, t') + C_d(t, t', t_0) \quad (\text{Equation 2.46})$$

It may be seen that unlike the previous two model codes described, the Rilem Model B3 differs in its use of compliance functions rather than notional coefficients. The creep behaviour is estimated as follows:

2.4.3.1 Basic Creep

The basic creep compliance function, based on the log-double-power law is expressed as:

$$C_0(t, t') = q_0 \ln\{1 + \psi[(t')^{-m} + \alpha](t - t')^n\} \quad (\text{Equation 2.47})$$

With:

$$q_0 = 2408 f_c^{-0.5} \quad (\text{Equation 2.48})$$

Where:

- $m = 0.5$
- $n = 0.1$
- $\alpha = 0.001$
- $\psi = 0.3$
- t = Age of concrete in days.
- t' = Age of concrete when loaded in days.
- $C_0(t, t')$ = Compliance function for basic creep only.
- q_0 = Coefficient accounting for the effect of concrete strength.
- f_c = Mean 28 day cylinder compressive strength in MPa.

2.4.3.2 Drying Creep

The additional deformation due to drying is estimated by means of the drying creep compliance function as follows:

$$C_d(t, t', t_0) = q_5 [e^{-3H(t)} - e^{-3H(t')}]^{0.5} \text{ for } t' > t_0 \quad (\text{Equation 2.49})$$

With:

$$H(t) = 1 - (1 - h)S(t) \quad (\text{Equation 2.50})$$

$$q_5 = 6000 (f_c)^{-1} \quad (\text{Equation 2.51})$$

$$S(t) = \tanh \sqrt{\frac{t - t_0}{\tau_{sh}}} \quad (\text{Equation 2.52})$$

Where:

- $C_d(t, t', t_0)$ = Compliance function for additional creep due to drying.
- t = Age of concrete in days.

- t' = Age of concrete when loaded in days.
- t_0 = Age of concrete when drying begins in days.
- h = Relative humidity of the environment expressed as a decimal ($0 < h < 1$)
- $H(t)$ = Spatial average of pore relative humidity within the cross section ($0 < H < 1$)
- $S(t)$ = Time function for shrinkage.
- τ_{sh} = Shrinkage half-time in days = $4.9(2 \cdot \text{area}/\text{perimeter})$

2.4.3.3 Total Shrinkage

The mean shrinkage strain in the cross-section unlike the previous two models is not expressed as the sum of autogenous and drying shrinkage and is expressed as follows:

$$\varepsilon_{sh}(t, t_0) = -\varepsilon_{sh\infty} \kappa_h S(t) \quad (\text{Equation 2.53})$$

With:

$$\varepsilon_{sh\infty} = \alpha_1 \alpha_2 \left[0.019 w^{2.1} (f_c)^{-0.28} + 270 \right] \quad (\text{Equation 2.54})$$

Where:

- α_1 = Coefficient to account for the type of cement used given by Table 2-6.
- α_2 = Coefficient to account for the type of curing used given by Table 2-7.
- κ_h = Humidity dependence coefficient given by Table 2-8.
- $S(t)$ = Time function for shrinkage given by Equation 2.4.3-7.
- $\varepsilon_{sh}, \varepsilon_{sh\infty}$ = Shrinkage strain and ultimate shrinkage strain respectively. Always given in 10^{-6} .
- w = Water content of the concrete mix in kg/m^3 .

Table 2-6: Rilem B3 Cement Coefficients

α_1	Cement Type
1.0	Type I
0.85	Type II
1.1	Type III

Table 2-7: Rilem B3 Curing Coefficients

α_2	Curing Method
0.75	Steam cured
1.0	Cured in water or 100% RH
1.2	Sealed during curing

Table 2-8: Rilem B3 Relative Humidity Coefficients

κ_h	h
$1-h^3$	$h \geq 0.98$
-0.2	$h = 1$ (Swelling in water)
Linear interpolation	$0.98 \leq h \leq 1$

2.4.4 Comparison of Numerical Models

In initial effort to gauge the applicability and accuracy of the numerical models described in the previous three sections, comparison graphs have been generated by plotting both the total shrinkage strains and total creep strains over time. These graphs depict calculated strain variations with time for all three models as well as the actual measured strain values obtained for tests conducted on physical samples. The intention in this section is to attain a preliminary understanding of the differences in accuracy in each numerical model compared both to each other and to actual test results. The physical test data has been obtained from the NU-ITI shrinkage and creep database previously mentioned and the test results chosen to be analysed for shrinkage and creep are that of sets e_069_01 and c_076_01 respectively. The input parameters for each data set are given in Table 2-9.

Table 2-9: Numerical Model Calibration Input Parameters

Parameter	e_069_01	c_076_01	Unit
Cylinder Dimensions	150x300	150x600	mm
w/c	0.6	0.68	-
a/c	5.02	6.047	-
c	358	300	kg/m ³
w	214.8	204	kg/m ³
f _c	17.7	15.5	MPa
E ₂₈	26500	27000	MPa
2(v/s)	75	75	mm
t ₀ /t _s	7	28	Day
RH	65	99	%

The total shrinkage strains calculated from each numerical model as well as the results from physical tests for a total period of drying equal to seven hundred and sixty days is as follows:

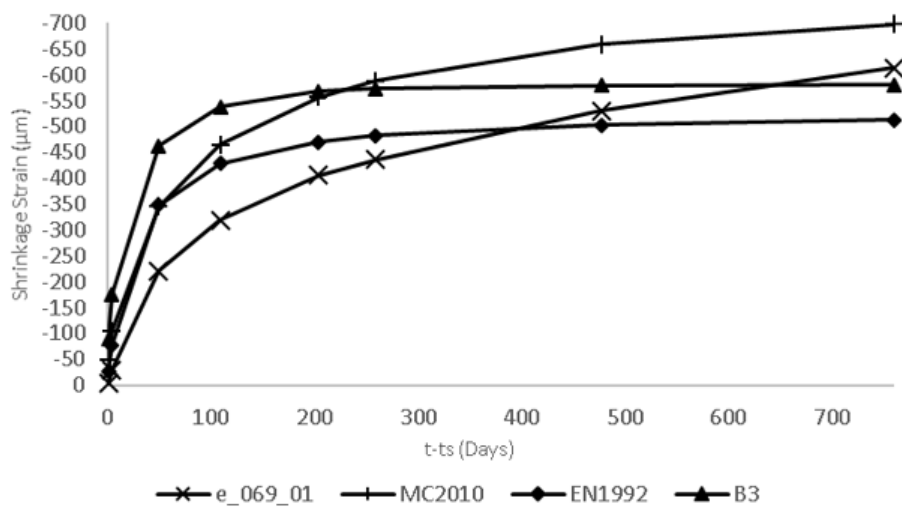


Figure 2-20: Numerical Model Shrinkage Comparison

It may be noted when investigating Figure 2-21 that in general, all three numerical models provide fairly accurate representations of the actual shrinkage behaviour of the concrete specimen. It may be seen that within the first four hundred days of drying, all three models overestimate the actual shrinkage strain whilst towards the end only the B3 model and Eurocode model underestimate it. On average over the entire period of drying, MC2010, EN 1992 and B3 all conservatively overestimate drying shrinkage strains by approximately 39%, 25% and 41% respectively. When investigating the final shrinkage strain value at seven hundred and sixty days, MC2010 still overestimates the actual value by approximately 12%

whilst the Eurocode and B3 models underestimate this value by approximately 20% and 6% respectively. With this in mind, it would appear that the B3 prediction model may be the most suited to this application.

Inputting the material parameters for data set c_076_01 into the three numerical models for creep prediction yields the results shown in Figure 2-22. For all models, the total creep shrinkage comprised of drying creep and basic creep is calculated in addition to the initial strain at the time of loading. The resultant creep strain is then divided by the initial applied stress which is 40% of the ultimate strength of the concrete which yields the specific creep curves shown expressed as $J(t,t')$ in microstrain per unit stress.

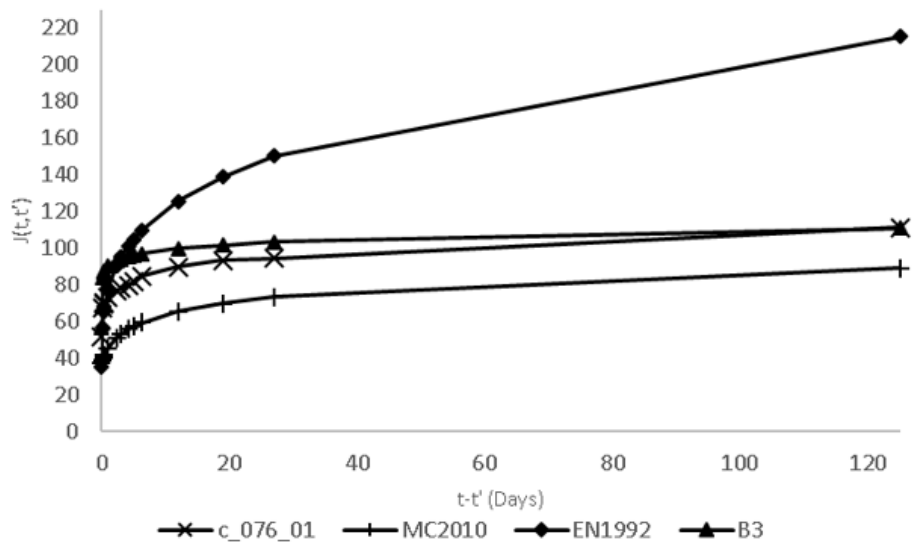


Figure 2-21: Numerical Models Creep Comparison

It may be seen that upon initial loading at $t-t'=0$, only the Rilem Model B3 is able to accurately replicate the results of the physical test data within a reasonable accuracy. In fact, the initial strain value only differs approximately 8.5% from that of the physical results whilst the MC2010 and EN 1992 initial strain values vary by approximately 28% and 32% respectively. This difference may be attributed to the adjustments made to the twenty-eight day Young's modulus value in both codes. When investigating the overall picture it is possible to see that both the MC2010 and B3 curves are able to replicate physical data reasonable well whilst the EN1992 method appears to diverge further with increasing time. On average, the results of MC2010, EN1992 and B3 vary 31%, 22% and 16% from the physical test data respectively with the closest ultimate strain at one hundred and twenty-five days being replicated by model B3 which varies only 0.4% from the physical test data. It would appear that due to the additional input parameters in model B3 such as cement content, water content and aggregate-cement ratio, the accuracy is increased and this appears to be the most suitable method to consider going forward.

Chapter 3 – Experimental Design

This chapter identifies the key parameters affecting mix design decisions as well as information pertaining to all of the constituent materials used in the chosen mix designs. The process utilised to attain workable and stable LWFC mixes is briefly explained and relevant water-solid ratios provided. The final mix designs are explained and summarised indicating relevant identification codes and constituent proportions. Finally, the testing procedures followed to conduct both experimental shrinkage and creep testing as well as any supplementary tests are given.

3.1 Materials and Parameters Tested

Typically, the measurement of creep and shrinkage strains attained from physical concrete samples provide the best indication and quantification of the long-term deformation behaviour of various different concrete mixes. In an effort to improve and expand the current understanding of creep and shrinkage as it pertains to LWFC specifically, it is proposed that physical testing and measurement of shrinkage and creep strains is to be conducted on a number of different LWFC samples. The intention of using this physical testing is to attain tangible shrinkage and creep data for various LWFC mixes, thus aiding in the process of achieving a holistic understanding of the dimensional stability of LWFC and providing data from which further numerical and finite element modelling may be carried out.

In Chapter 1 it has been stated that the effects of foam volume, density, cement paste content, supplementary cementitious materials and other additives are to be investigated and in Chapter 2 the influence of microstructure, different SCMs and additives have been studied. Using these key objectives in conjunction with literature findings, it is possible to identify a selected amount of mix variations to be put forward for experimental creep and shrinkage testing. In an effort to investigate the effects of foam volume, density and cement paste, mixes may be tested which contain only ordinary Portland cement and vary only in density. These mixes are to vary in density from 1200 kg/m^3 to 1600 kg/m^3 and contain only OPC 52.5N CEMII cement conforming to SANS 50197-1:2013 with a relative density of 3.14.

As the cement-only mixes quantify the effects of varying density and foam volume, the effects of different filler types in varying quantities must also be investigated. As fly-ash is a staple of typical LWFC mixes, samples containing cement and fly-ash are to be tested. Ulula Class-S Fly-ash conforming to SANS 50450-1:2011 with a relative density of 2.20 is to be used with $a/c=1$ and $a/c=2$ and the results compared to a control cement-only mix of the same density. This is to be done to investigate the effects of fly-ash as a filler in general and to what extent varying the filler/cement ratio plays a role.

As uncovered in Chapter 2, LWFC samples containing sand as a filler have been seen to exhibit improved dimensional stability attributed to the increased shrinkage restraining capacity of stiffer sand particles. With this known, it is imperative that mixes containing cement and sand only be investigated. Readily available Malmesbury sand conforming to SANS 5844:2006 with a relative density of 2.65 and fineness modulus of 2.21 is to be used with $s/c = 1$ and $s/c=2$ and the results compared to the cement-only control mix and cement-fly-ash mixes of the same density. With both fly-ash and sand mixes being tested, mixes which feature a combination of both fillers are to be tested in an effort to study their combined influence in comparison to the cement-only and filler-only mixes.

The potential benefits of glycol compounds have also been uncovered in research and thus, the final mixes to be put forward for experimental creep and shrinkage testing are to contain commercial grade propylene glycol with a density of 1.036g/cm^3 . The added effects of this propylene glycol are to be tested by including it in selected cement-sand and cement-fly-ash mixes in the dosage of seven percent by weight of cement. Additionally, it should be noted that as polypropylene fibres are also a staple of typical LWFC mixes and have been reported to aid in mitigating the effects of non-linear actions such as cracking, all mix variations are to contain SAPY Corefil 12mm polypropylene fibres with a density of 910 kg/m^3 and dosage of 0.45% by mix volume. All mixes are also produced using FoamTech hydrolysed protein-based foaming agent with a relative density of 0.075 kg/m^3 .

3.2 Mix Designs

The consistency and workability of a hydrated cement paste directly influences the stability of LWFC mixes. This is due to the yield strength and viscosity characteristics of the paste and their ability to allow or inhibit the migration of entrained air voids through and out of the paste. As a preliminary step and as a means of more accurately controlling the workability of base mixes and determining the water demand of Portland cement and SCMs, the ASTM flow table test for hydraulic cements shown in Figure 3-1 may be utilised. The full test which may be found in the ASTM C230/C230M Standard Specification is conducted in summary as follows:

1. Sample mixture is placed into a 50mm high cone with an upper diameter of 70mm and a lower diameter of 100mm. This cone rests upon a circular base plate with a diameter of 255mm.
2. The cone is removed leaving only the sample mixture and the base plate which is attached to a rotating handle is then lifted and dropped repeatedly fifteen times from a height of 12.7mm.
3. The diameter of the spread of the sample mixture is then measure in two directions and the average is taken.
4. An average spread value of 230mm is acceptable to attain a stable and workable LWFC mixture. This is based upon previous research such as that of (van Rooyen, 2013) and (Dunn, 2017)

The flow table test is carried out for all combinations of cements, fillers and additives, adjusting the water content each time until a target diameter of 230mm is achieved. By carrying out this process, the w/c ratio may be attained first by producing a base mix which contains only cement and water. When adding fillers such as fly ash and sand, the corresponding water/binder ratio may then be achieved, and as the w/c is already known, the appropriate water demand of the fillers may be calculated. It should also be noted that all mixes contain 0.45% fibres by volume and no appreciable difference in water demand for mixes containing 7% propylene glycol by weight of cement has been noted. This process is repeated for all s/c, a/c and s/a ratios which yields the following:

Table 3-1: Water-Solid Ratios

Ratio	Value
water/cement	0.38
water/sand	0.073
water/ash	0.32



Figure 3-1: ASTM Flow Table Test 230mm

As the mix objectives, materials and water demands have been determined and specified, a decision may be made as the final mixes to be cast for physical testing. A matrix-based approach is to be used in which only specific densities and filler/cement ratios are to be tested. As the physical measurement of creep and shrinkage strains often requires numerous samples for each mix design tested, this approach limits the total amount of samples that need to be cast. Interpolation and extrapolation may therefore be used for mixes with densities and filler/cement ratios which vary from those tested. Table 3-2 indicates the decision on the final mixes to be tested. It may be seen that the effects of foam volume and density are to be investigated by testing cement only mixes which vary only in density, thus eliminating the effects of SCMs and any other additives. The effects of various filler/cement ratios is also investigated by varying sand/cement, ash/cement and ash/sand ratios for mixes of the same density. In this way the effects of the fillers themselves may be investigated rather than density and foam volume. Finally, two mixes are to be made which include commercial propylene glycol. This enables its effects to be recorded and compared to the mixes with the same filler/cement ratios and density. The values indicated in Table 3-2 are representative of ten litre mixes.

Table 3-2: Final Mix Designs for Testing

Mix	a/c	s/c	Density (kg/m ³)	Cement (kg/m ³)	Water (kg/m ³)	Sand (kg/m ³)	Fly Ash (kg/m ³)	Fiber (kg/m ³)	Foam (kg/m ³)	PG (kg/m ³)
C12	0	0	1200	850	320	0	0	4.1	30.7	0
C14	0	0	1400	1000	380	0	0	4.1	22.8	0
C16	0	0	1600	1150	440	0	0	4.1	14.9	0
SC1	0	1	1400	560	250	560	0	4.1	26.8	0
SC2	0	2	1400	390	200	780	0	4.1	28.4	0
AC1	1	0	1400	510	360	0	510	4.1	18.5	0
AC2	2	0	1400	340	350	0	690	4.1	17.0	0
SAC1	1	1	1400	370	260	370	370	4.1	23.4	0
SAC2	2	2	1400	230	230	460	460	4.1	23.5	0
SCP2	0	2	1400	390	200	780	0	4.1	28.4	27.3
ACP2	2	0	1400	340	350	0	690	4.1	17.0	23.8

3.3 Shrinkage and Creep Testing

This section provides a summary of the procedures carried out in order to conduct the autogenous shrinkage, drying shrinkage, basic creep and drying creep experiments. A combination of existing standards have been used as discrepancies have been found in each and there is no one standard available for the shrinkage and creep measurement of LWFC specifically. Some of these discrepancies include different preparation methods, different sample sizes, sample quantities and varying measuring schedules. This has been done in an effort to standardise the testing procedure as much as possible whilst still attaining appropriate results. The reference standards used to conduct shrinkage testing are:

- BS ISO 1920-8:2009 – Testing of concrete – Part 8: Determination of drying shrinkage of concrete samples prepared in the field or in the laboratory
- ASTM C 157/C 157M – 08 Standard Test Method for Length Change of Hardened Hydraulic Cement Mortar and Concrete

Whilst the reference standards used to conduct creep testing are:

- Draft: BS EN 12390-17 (Testing hardened concrete: Part 17: Determination of creep in concrete in compression (08 June 2018))
- ASTM C512 – 02 Standard Test Method for Creep of Concrete in Compression

When preparing samples for shrinkage and creep testing, a total of ten 100mm x 200mm cylindrical moulds are to be prepared. In addition, an electronic measuring gauge capable of measuring one-hundredth of a millimetre (Figure 3-5), 100mm stainless steel reference bar, stainless steel gauge studs, concrete adhesive, paraffin wax and plastic wrap are required. From the ten cylindrical samples cast, two are to be used for measurements of autogenous shrinkage, two are to be used for measurements of drying shrinkage, two are to be used for basic creep, two are to be used for drying creep and the remaining two are to be used for accompanying compressive strength or Young's modulus tests.

The process of sample preparation is to begin with casting of all ten cylindrical moulds at the same time from the same batch. Once cast, the samples may then be covered with either a damp cloth or plastic wrap where they are to be left to set in a climate-controlled room at approximately 23°C and 50% relative humidity for approximately twenty to forty-eight hours. Once set, the cylinders are to be stripped from their moulds and wiped clear of all excess dirt and oils after which time the top and bottom bearing surfaces may then be ground to a sufficiently even finish to ensure even stress distribution for those samples subjected to creep testing. An example of a cylinder after grinding is shown in Figure 3-3.

For both shrinkage and creep samples, the concrete adhesive may then be used to attach two sets of two gauge studs on opposite sides of the cylinder at a length of 100mm apart (gauge length $\geq h/2$). Once the stainless steel gauge studs have been attached, samples to be used for drying shrinkage measurements are to be sufficiently sealed in plastic wrap and left to cure until an age of seven days from casting whilst the samples used for drying creep measurements are also sealed and left to cure until an age of twenty-eight days where full strength has been achieved. For both autogenous shrinkage and basic creep, the samples are to be sufficiently coated in paraffin wax (shown in Figure 3-2) and plastic wrap and also left to cure for seven and twenty-eight days respectively. The process of sealing autogenous samples in paraffin wax and plastic wrap is carried out to provide a double barrier against moisture loss and ensure perfect sealed conditions. It should also be noted that all curing and sample preparation is to be carried out in the same climate-controlled room at approximately 23°C and 50% relative humidity.

After a setting and curing period of seven days, the shrinkage samples may be prepared for testing. Samples used for drying shrinkage measurements may be unwrapped whilst the samples used for autogenous shrinkage are to be left sealed in both the plastic wrap and paraffin wax to ensure no moisture loss. The samples are then to be placed in a low-disturbance area within the climate-controlled room with at least 50mm clearance on both sides. With the samples placed, the length gauge may be used to measure and record the initial lengths between gauge studs on each side of each cylinder – this serves as the initial gauge length as compared to the 100mm reference bar. With the initial lengths measured and recorded, subsequent measurements are to be taken once per day for seven days, once per week for four weeks and once per month until the end of testing. The shrinkage strain may be calculated as follows:

$$\varepsilon_{sh} = \frac{L_0 - L_i}{L_0} \quad (\text{Equation 3.1})$$

Where:

- ε = Shrinkage strain (μm)
- L_0 = Original gauge length (mm)
- L_i = Length measured at time increment “i” (mm)

After the curing period of twenty-eight days has been completed and the creep samples have reached adequate strength, the samples may be prepared for testing. Samples used for drying creep measurements may be unwrapped whilst the samples used for basic creep are to be left sealed in both the plastic wrap and paraffin wax to ensure no moisture loss. The length comparator may be used to measure and record the initial lengths between gauge studs on each side of each cylinder – this serves as the initial gauge length as compared to the 100mm reference bar. With the initial lengths recorded, the samples may then be carefully placed into the loading frame and secured, Figure 3-4 indicates the loading frame used with eight cylinders secured in the four individual loading structures. Once secured, the samples are to be loaded with a compressive force equal to but not exceeding 40% of their ultimate compressive strength which is determined just prior by means of uniaxial cylinder compression tests conducted according to SANS 5863. It should also be noted that the load should be applied in less than thirty seconds. With the samples loaded, subsequent measurements are to be taken immediately after the load has been applied, once per day for seven days, once per week for four weeks and once per month until the end of testing. The creep strains (expressed in microstrain) may then be calculated by dividing the change in length at each testing day by the original gauge length as shown by Equation 3.2. Additionally, the compliance function $J(t, t', t_0)$ or “specific creep” may also be calculated and is expressed as the ratio of microstrain to applied unit stress as shown by Equation 3.3.

$$\varepsilon_{cr} = \frac{L_0 - L_i}{L_0} \quad (\text{Equation 3.2})$$

$$\text{Specific Creep} = \frac{\mu m(t)}{\sigma_0} \quad (\text{Equation 3.3})$$

Additionally, it should also be noted that measurement points shall be parallel to the principal axis of the test specimen, and length readings taken on each measuring day should be taken as the average of the two sets of gauge studs on each cylinder and the average of both cylinders for each mix for drying shrinkage, drying creep, autogenous shrinkage and basic creep. The masses of all cylinders are also to be recorded after stripping, when testing commences and at the date of completion to compare total moisture loss in each specimen versus shrinkage exhibited. No more than three cylinders may be stacked vertically and loaded simultaneously and specimens shall be aligned as perfectly as possible with smooth-ground bearing faces to avoid uneven stress distributions. It should also be ensured that before recording each reading, the applied stress should not have deviated more than 3% from the target value.

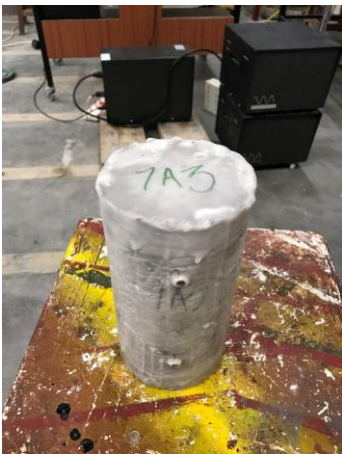


Figure 3-2: Paraffin wax sealed sample



Figure 3-3: Bearing face after grinding



Figure 3-4: Creep samples in loading frame



Figure 3-5: MarCator 1075 R Digital Indicator and 100mm reference bar

3.4 Supplementary Tests

3.4.1 Compressive Strength

As samples subjected to creep testing are to be loaded at 40% of their ultimate compressive strength, cylinder compressive strength tests are to be conducted on all mix variations proposed for testing. Done in accordance with SANS 5863 (SANS, 2006), additional cylinders are cast whilst casting creep and shrinkage specimens and put aside to be tested for compressive strength at an age of twenty-eight days. The uniaxial test is to be performed by means of a Contest Grade A compression testing machine where cylinders are loaded at a rate of 90kN/m until failure occurs. Where f_{cc} denotes the compressive strength in Mega Pascal, F the maximum load at failure and A_c the cross-sectional area of the specimen the cylinder compressive strength is expressed as follows:

$$f_{cc} = \frac{F}{A_c} \quad (\text{Equation 3.4})$$

3.4.2 Verification of Load Values

In an effort to ensure creep cylinders are loaded to the correct value, a load calibration test has been conducted by placing a load cell between two disposable cylinders and recording the output (Figure 3-6). As the hydraulically operated jacks lack sensitivity and pressure gauges indicate loading pressure in bar and psi, this has been considered an essential step to ensure reliability in loading values and attain useable results. After placing the load cell between cylinders, the jacks are pressurised to a target value and the output recorded in an effort to attain a correlation between jack pressure and loading force. This process has been repeated for a variety of target loads and it has been established that a correlation of approximately 1 bar = 1 kN exists. In addition, recordings have also been carried out for approximately one hour to ensure no pressure is lost which should be the case as the loading frame contains an accumulator tank to ensure pressure stability in the hydraulic jacks even when disconnected from the pump. Figure 3-7 indicates the results of a loading calibration test carried out for a target load of 30kN.



Figure 3-6: Load Cell Setup

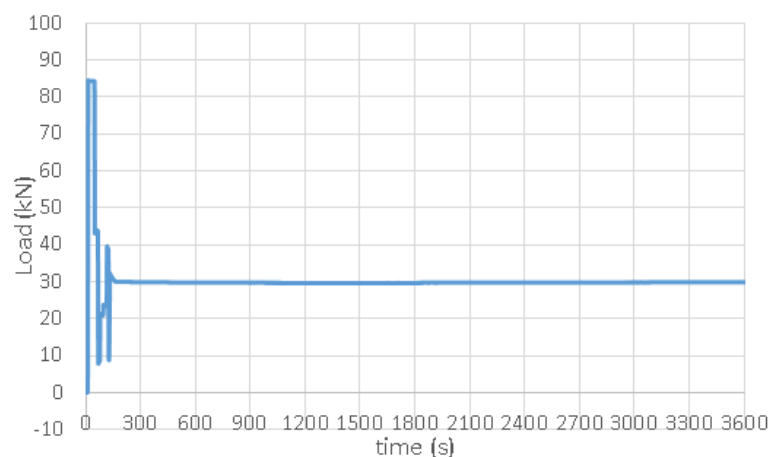


Figure 3-7: 30kN load verification

Chapter 4 – Finite Element Modelling

The latest update of Diana Finite Element Analysis Software is that of Diana 10.2. Whereas previous versions of this FEA software have been restricted to metal creep and transient creep models, this latest version allows for the modelling of creep and shrinkage of concrete under long term load as an aging viscoelastic material. Diana makes provision for the design codes discussed in this paper and thus simplifies the task of attaining creep and shrinkage strains by allowing the user to input certain input parameters previously mentioned and implementing the specified design code procedure to attain the output. However, as LWFC does not behave in the same way as regular concrete and none of the codes studied include sections to deal with creep and shrinkage of LWFC specifically, a finite element analysis has to be created using a user defined non-linear Kelvin-Chain non-linear viscoelastic model.

4.1 Background

A viscoelastic model is used to describe a material behaviour with memory. More accurately put, it is used to describe a case where the strain history affects the current stresses. When analysing this type of behaviour, it is important to note that input data may either be obtained from physical creep or relaxation testing. Whereas in creep testing the strains are recorded over time for a constant stress applied at the beginning, relaxation tests consist of applying an initial strain and recording the accompanying stresses over time. The resulting strain-time data obtained for creep testing is referred to as the creep function whilst stress-time data obtained from relaxation tests is referred to as the relaxation function. As the focus of this research is shrinkage and creep testing, only the creep function is described further.

Viscoelastic behaviour may be represented by means of a creep function. The relation between stresses and strains obtained from a creep function may be given as:

$$\varepsilon(t) = \int_{-\infty}^t J(t, \tau) \bar{C} \dot{\sigma}(\tau) d\tau \quad (\text{Equation 4.1})$$

In this equation, the term $J(t, \tau)$ refers to the creep function whilst \bar{C} represents a 6x6 dimensionless matrix which is set up as a function of the material Poisson's ratio. This matrix is expressed as:

$$\begin{bmatrix} 1 & -\nu & -\nu & 0 & 0 & 0 \\ -\nu & 1 & -\nu & 0 & 0 & 0 \\ -\nu & -\nu & 1 & 0 & 0 & 0 \\ 0 & 0 & 0 & 2(1+\nu) & 0 & 0 \\ 0 & 0 & 0 & 0 & 2(1+\nu) & 0 \\ 0 & 0 & 0 & 0 & 0 & 2(1+\nu) \end{bmatrix}$$

Figure 4-1: Poisson Matrix for Creep Function

It is then assumed that from time equal to negative infinity to time equal to zero, nothing has occurred and no stresses and strains are recorded. In this case, the strain increment is then calculated from time equal to zero to time equal to “t” and time equal to “t” to time equal to delta “t”. Equation 4.1 then becomes:

$$\varepsilon(t) = \int_0^t J(t + \Delta t, \tau) - J(t, \tau) \bar{C} \dot{\sigma}(\tau) d\tau + \int_t^{t+\Delta t} J(t + \Delta t, \tau) \bar{C} \dot{\sigma}(\tau) d\tau \quad (\text{Equation 4.2})$$

Diana has three viscoelastic models available, namely the Maxwell Chain, Power Law and Kelvin Chain Models. Both the Kelvin Chain and Double Power law models are examples of creep functions and it is the Kelvin Chain model which has been focused on during this research. According to (Hedegaard, Asce, Shield, Asce, French & Asce, 2014), creep models which are typically represented as compliance functions have been converted to rate-type models based on the Kelvin-Chain model specifically for plain concrete following the works of (Bažant & Prasannan, 1989). The conversion of rate-type models to Kelvin-Chain models allows for the more efficient computation of viscoelastic behaviour as the need to refer to the entire stress history of the viscoelastic material at each integration point for each time step is negated.

Physically, the Kelvin-Chain model may be described as a simple mechanical model for viscoelastic behaviour represented by a linear spring and dashpot connected in parallel as shown in Figure 4-2. The total strain in the Kelvin-Chain model resulting from an initial applied unit stress at time zero is expressed mathematically as:

$$\varepsilon = \frac{\sigma_0}{K} \left(1 - e^{-\frac{Kt}{C}} \right) \quad (\text{Equation 4.3})$$

Where:

- K = Spring stiffness
- C = Viscous damping coefficient of the dashpot
- ε = Strain
- σ_0 = Initial applied unit stress
- t = time

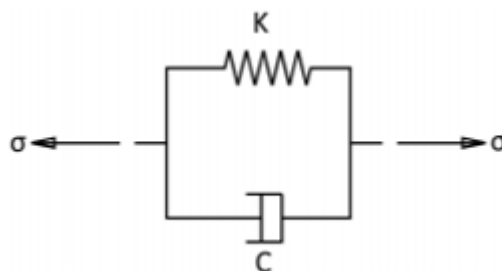


Figure 4-2: Single Kelvin-Chain Unit

As time progresses towards infinity, the strain converges to an asymptotic value of σ_0/K indicating the total applied stress is resisted by the spring element only. Additionally, the retardation time t_r is determined by the stiffness and viscosity of the springs and dashpots at each point in the Kelvin Chain. The retardation time may be calculated as follows:

$$t_r = \frac{C}{K} \quad (\text{Equation 4.4})$$

Assuming that the initial applied unit stress is kept constant at a value of one and is applied at time zero, Equation 4-4 may be utilised to describe the compliance function such that:

$$\varepsilon = \sigma_0 J(t, t_0) = \sigma_0 \left\{ \frac{1}{K} [1 - e^{-K(t-t_0)/C}] \right\} \quad (\text{Equation 4.5})$$

As the Kelvin-Chain model is used to describe the time-dependent behaviour of a viscoelastic material, a series of linearly connected chain “links” may be used as shown in Figure 4-3. It is assumed that all chain elements are subjected to the same applied stress and therefore, the total strain may be expressed as the sum of strains resulting from each individual element. This is expressed mathematically as follows:

$$\varepsilon(t) = \sigma_0 J(t, t_0) = \sigma_0 \sum_{i=1}^N A_i \left\{ \left[1 - e^{-\frac{K(t-t_0)}{C}} \right] \right\} \quad (\text{Equation 4.6})$$

Where:

- $A_i = 1/K_i =$ Compliance element of element “i”.
- $t_{ri} = C_i/K_i =$ Retardation time of element “i”.

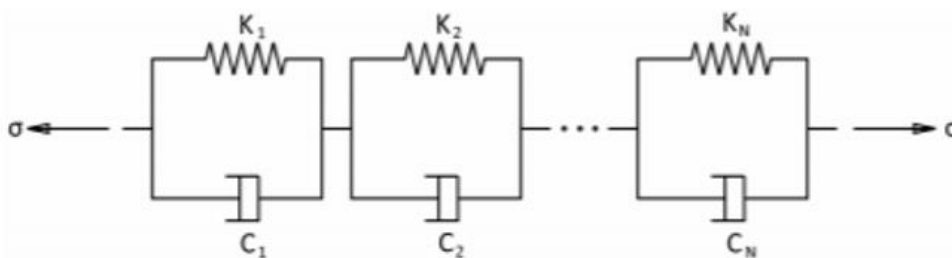


Figure 4-3: Kelvin-Chain

The Kelvin-Chain model utilised by Diana FEA software is formulated on the same theory, however, the creep function calculated as a function of the concrete Young’s Modulus is expressed as Dirichlet series shown visually in Figure 4-4 and mathematically by Equation 4.7.

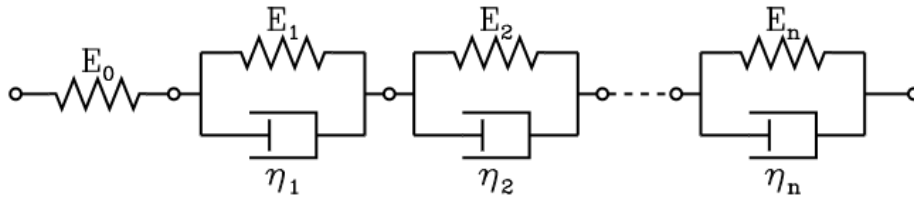


Figure 4-4: Kelvin-Chain Diana

$$J(t, \tau) = \sum_{\alpha=0}^n \frac{1}{E_{\alpha}(\tau)} \left(1 - e^{-\frac{t-\tau}{\lambda_{\alpha}}}\right) \quad (\text{Equation 4.7})$$

In this formulation, the $E_{\alpha}(\tau)$ term denotes that the stiffness of the model may be time dependent due to temperature or maturity influences. In the same way as Equation 4.4, the retardation time in Diana is calculated as follows:

$$\lambda_{\alpha} = \frac{\eta_{\alpha}}{E_{\alpha}} \quad (\text{Equation 4.8})$$

As the theory behind creep functions and the Kelvin Chain has been discussed, it is possible to delve into the methods utilised by Diana when receiving creep and shrinkage data as indirect input variables. Diana is able to generate direct input from indirect input of shrinkage or creep curves with time. The direct input of the Kelvin Chain parameters is determined by the total number of units in the chain, for each unit in the chain the elasticity of springs and viscosity of dashpots are determined from the indirect input of these shrinkage and creep curves. Diana utilises curve fitting to determine the properties of these chains as indicated by Figure 4-5. In this method, the initial stiffness of the unit without the dashpot is represented by the $E_0(\tau)$ value, whilst the $1/E_i(\tau)$ reciprocal stiffness denotes the final strain. The corresponding stiffness and retardation times of other links within the chain are then calculated by means of a nonlinear least squares approximation. In this approximation, the initial parameters are iteratively adapted by minimising the difference between the given curve f and the approximated curve f^* at n discrete ages. This method is indicated by Equation 4.9.

$$\text{error} = \sum_{i=1}^n (f_i - f_i^*)^2 \quad (\text{Equation 4.9})$$

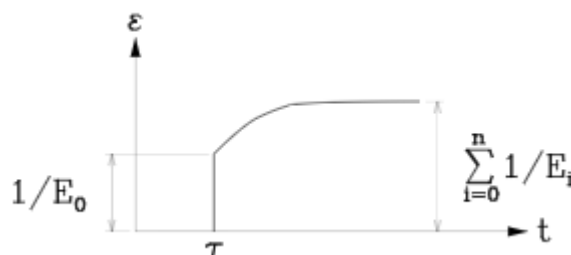


Figure 4-5: Curve Fitting Solution Method Diana

4.2 Finite Element Model

This section describes the process followed to generate the FEA models capable of replicating the results of physical shrinkage and creep tests on sample cylinders in Diana FEA. The modelling planes, dimensions, material properties, meshing properties and all other input parameters are given and described to provide a full schematization of the problem.

4.2.1 Model Creation and Geometry

When beginning the process of creating the FEA model, a structural analysis must be chosen specifying the model dimensions to be axial symmetric. An axial symmetric model may be used in this case as it is only necessary to replicate one plane within the longitudinal section of a cylinder as all concentric planes within the cylinder exhibit the same stress and strain distributions due to symmetry. Diana also specifies in the initial model creation step that the default mesher type, default mesh order and mid-side node locations must be chosen, these are identified as hexa/quad, quadratic and on-shape respectively.

As the axial-symmetric model has been created, it is now possible to define and add the required geometry by creating a polygon sheet. Again, the use of a two-dimensional polygon sheet is required as only one plane within the longitudinal section is being replicated. The polygon sheet dimensions should correlate to a width equal to half the width of the sample cylinder and a height equal to the full height of the sample cylinder. An example of the input for creating a polygon sheet correlating to a concrete cylinder of 100mm x 200mm is given in Figure 4-6.

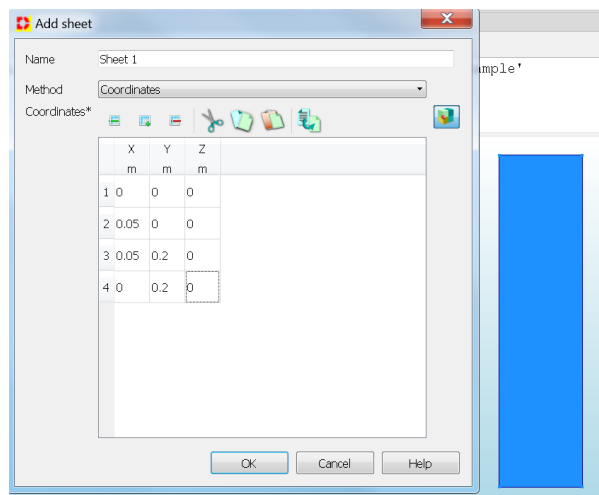


Figure 4-6: Axisymmetric sheet input for 100mmx200mm cylinder

4.2.2 Property Assignments

Geometry specified and created, it is now possible to specify property assignments by first selecting the polygon sheet and assigning the element class to regular solid rings. Solid rings in Diana are axisymmetric elements with a two-dimensional cross-section. For each element there are two degrees of freedom correlating to the x and y displacements at each node. With the element class specified, it is now possible

to create a new material and specify the material class. LWFC is not included in any of the current standard design codes and thus, the standard concrete code materials may not be used. Instead, the material class of concrete and masonry may be selected where the Maxwell/Kelvin Chain viscoelasticity material model may be selected. Once selected, the linear material properties such as Young's modulus, Poisson's ratio and mass-density may be specified. Following this, viscoelastic chains may be added by specifying the chain type as Kelvin Chains-creep and the input type to be creep function with the maximum number of chains equal to ten (it should be noted that Diana allows only a maximum of ten chains). With these specified, the appropriate creep function may be input which consists of inputting time increments accompanied by specific creep values expressed as microstrain per unit stress. An example of this input is shown in Figure 4-8 for the creep function for data set c_076_01 used in Section 2.4.4. To finish off the material definition, the shrinkage strain function may be specified as element age dependent where the element age shrinkage strain may be defined by inputting a corresponding shrinkage curve consisting of measured shrinkage strains over time for the same material. An example of this input is also shown in Figure 4-7 for the shrinkage curve for data set e_069_01 used in Section 2.4.4.

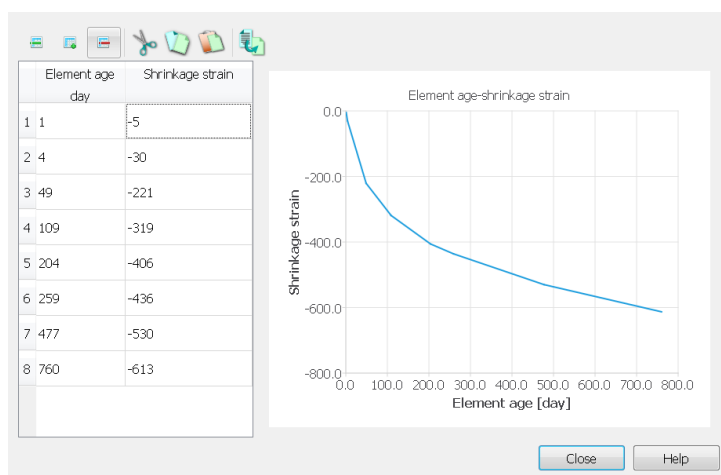


Figure 4-7: Direct Shrinkage Curve Input Diana



Figure 4-8: Direct Creep Curve Input Diana

4.2.3 Boundary Conditions

Now that the geometry and property assignments have been set, it is possible to define support conditions and assign mesh properties. As an axisymmetric plane within the sample cylinder is being modelled, two translational boundary conditions are to be specified. The first of these is assigning a base boundary condition preventing translation in the vertical direction which simulates the effects of a sample being placed on a solid surface. The second boundary condition must be applied to the inside edge of the polygon sheet replicating the zero-displacement in the horizontal direction along the centreline of the cylinder. The boundary conditions are shown in Figure 4-9 and are applied along the entire edge of the sheet even though Diana only displays five points on each edge. Rotational boundary conditions are not required in this instance as the two-dimensional axisymmetric modelling space automatically prevents any rotations of the element out of plane.

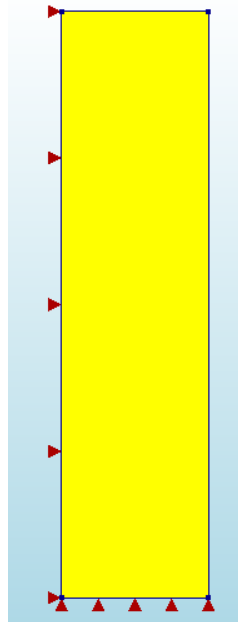


Figure 4-9: Boundary Conditions

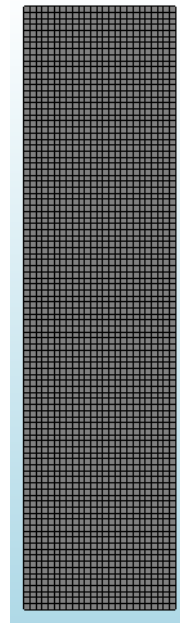


Figure 4-10: Meshed Element

4.2.4 Meshing

Geometries, material properties and boundary conditions specified, the mesh properties of the model may now be set. The polygon sheet may be selected and the element size specified either by edge divisions or element size. In this case, the element size has been selected and specified as 0.002m which divides the axisymmetric element into one hundred elements in the vertical direction and twenty-five elements in the horizontal direction as shown in Figure 4-10. The seeding method is also then chosen as element size and the mesher type is specified as hexa/quad elements with the mid-side node location on shape. The rectangular shape of the axisymmetric polygon sheet promotes the use of hexa/quad elements as opposed to triangular elements. Additionally, mesh sensitivity dependent on element size has been noted as negligible attributed to the direct input of creep and shrinkage curves and curve fitting solution method.

The elements used in this instance are CQ16A quadrilateral elements as shown visually in Figure 4-11. A CQ16A element represents an eight node isoparametric axisymmetric solid ring element with a quadrilateral cross-section. The CQ16A quadrilateral element is based on quadratic interpolation and Gauss integration where the polynomial used for the displacements in the horizontal and vertical directions is given by:

$$u_i(\xi, \eta) = a_0 + a_1\xi + a_2\eta + a_3\xi \cdot \eta + a_4\xi^2 + a_5\eta^2 + a_6\xi^2\eta + a_7\xi \cdot \eta^2 \quad (\text{Equation 4.10})$$

The use of this polynomial yields strain ϵ_{xx} which varies linearly in the horizontal direction and quadratically in the vertical direction and strain ϵ_{yy} which varies linearly in the vertical direction and quadratically in the horizontal direction. It should also be noted that shear strain γ_{xy} varies quadratically in both directions. The default integration scheme applied by Diana for a CQ16A quadratic element is 2x2 where $n_\xi = 2$ and $n_\eta = 2$.

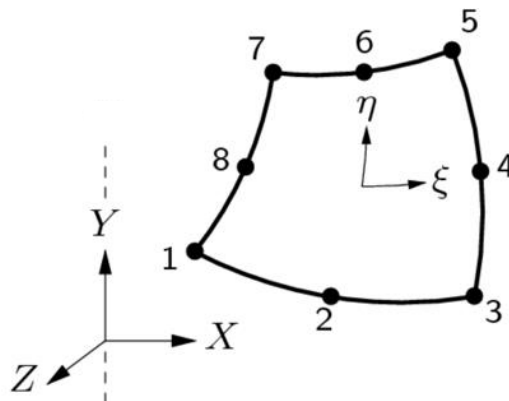


Figure 4-11: CQ16A Isoparametric Element

4.2.5 Analysis

The penultimate step in creating the FEA model is that of creating and running the analysis. In this step, a structural non-linear analysis step is created where a custom command is added. The command added is that of execute time steps where the time steps may be chosen as user specified. The user specified time steps for each model must correlate to the creep and shrinkage curves used as inputs in the Kelvin Chain material section to ensure consistency in results. With the time steps specified, equilibrium iterations are set to a total of ten with the method being Newton-Raphson. The convergence norms for displacement and force must also be set to continue rather than terminate with a convergence tolerance of 0.01 and abort criterion of 10000. As the model geometries, properties, meshing and analysis methods have been specified, the model outputs may be chosen. As only the creep and shrinkage strains of specimens are of interest, the total Green principal strains may be selected where after submitting for analysis, the strains in the E1 direction are used to compile and compare results.

4.2.6 Model Comparison

In an effort to gauge the accuracy and applicability of the axisymmetric model created in Diana, the same sample data used to calibrate the numerical models in Chapter 2 has been used to calibrate the finite element model. Shown in Figure 4-12 and Figure 4-13 for shrinkage and creep respectively, the results of the physical tests are plotted together with the output from the Kelvin-Chain material model and the numerical models already provided in the Diana material library. As Diana does not make provision for the Rilem B3 model, the results obtained from manual Excel calculations are provided for reference. It may be seen that overall, all models are able to replicate the actual shrinkage and creep behaviour fairly accurately, particularly that of the Kelvin-Chain model. The next closest result is that of the Rilem B3 mode which varies approximately 5% from actual results at seven hundred and sixty days. Both the MC2010 and EN1992 material models in Diana provide similar results to one another with an average underestimation at the end of simulation equal to approximately 22%. This indicates that where available, the direct input of shrinkage and creep curves from physical testing is favourable for finite element model simulations.

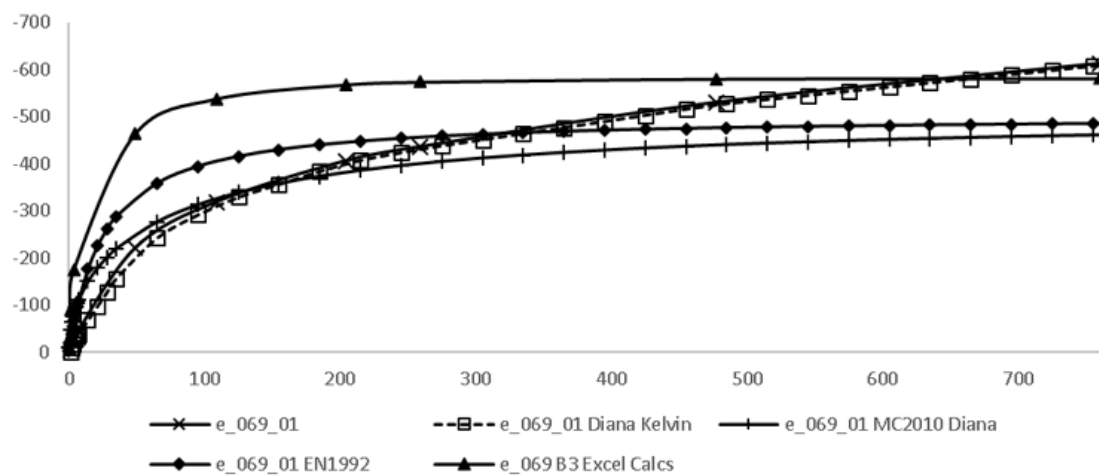


Figure 4-12: Shrinkage Modelling Comparisons Diana

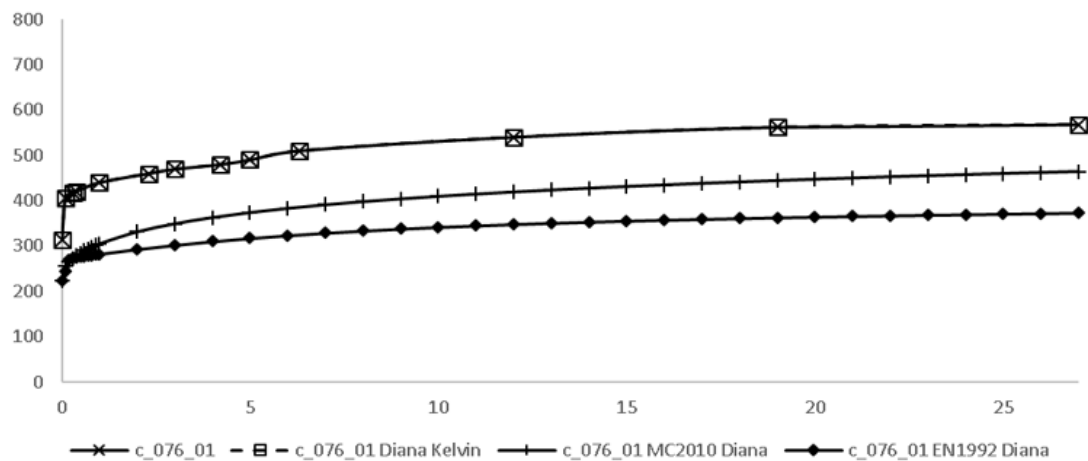


Figure 4-13: Creep Modelling Comparisons Diana

Chapter 5 – Results and Discussion

This chapter provides the experimentally obtained drying shrinkage, autogenous shrinkage, basic creep and drying creep strains for a total of forty-four cylinders tested over a one hundred and fifty five day period and sixteen cylinders tested over a twenty-eight day period. The shrinkage and creep strains have been obtained as discussed in the Experimental Design Chapter and the results for LWFC samples which vary in density and fillers are presented and discussed. In addition, the contribution of basic creep and autogenous shrinkage to drying creep and drying shrinkage is discussed along with the moisture loss over the period of testing. This chapter also provides results of populating existing numerical models and finite element models with LWFC parameters. The results of these models are compared to physical results and adjustments made where necessary.

5.1 Physical Testing

5.1.1 Shrinkage Testing

The results presented in this section provide the physically obtained drying shrinkage and autogenous shrinkage strain values for the chosen test mixes. For each mix variation e.g. C12, two cylinders each with two separate sets of gauge studs have been cast for both drying shrinkage and autogenous shrinkage values and the averages taken of both the two sets of gauge studs on each cylinder and both cylinders for each mix variation. In total for both drying shrinkage and autogenous shrinkage strain measurements, forty-four cylinders have been cast using a total of one hundred and seventy-six stainless steel gauge studs and measurements have been recorded over a period of one hundred and fifty-five days equating to a total of one thousand four hundred and eight individual data points being captured. Table 5-1 provides information on each mix variation tested for shrinkage strain measurements as well as their respective identification codes which are used going forward. This table only provides a brief indication of the mix variations, however, full mix composition tables may be found in Table 3-2. When considering the identification codes of each mix, it is important to note that C denotes cement-only, SC denotes sand and cement, AC denotes fly ash and cement, SAC denotes a combination of cement, sand and fly ash and P denotes the inclusion of propylene glycol. The numbers 12, 14 and 16 identify the densities of the cement-only mixes whilst the numbers 1 or 2 denote the filler-cement ratio of the mixes containing either sand, fly ash or a combination.

Table 5-1: Shrinkage Testing Mixes

Mix	Cylinders	Drying/ Autogenous	Description	ρ (kg/m ³)	s/c	a/c
C12	C12-1	Drying	Cement only.	1200	-	-
	C12-2					
	C12-3	Autogenous				
	C12-4					
C14	C14-1	Drying	Cement only.	1400	-	-
	C14-2					
	C14-3	Autogenous				
	C14-4					
C16	C16-1	Drying	Cement only.	1600	-	-
	C16-2					
	C16-3	Autogenous				
	C16-4					
SC1	SC1-1	Drying	Cement + Coarse Malmesbury Sand.	1400	1	-
	SC1-2					
	SC1-3	Autogenous				
	SC1-4					
SC2	SC2-1	Drying	Cement + Coarse Malmesbury Sand.	1400	2	-
	SC2-2					
	SC2-3	Autogenous				
	SC2-4					
AC1	AC1-1	Drying	Cement + Ulula Fly Ash.	1400	-	1
	AC1-2					
	AC1-3	Autogenous				
	AC1-4					
AC2	AC2-1	Drying	Cement + Ulula Fly Ash.	1400	-	2
	AC2-2					
	AC2-3	Autogenous				
	AC2-4					
SAC1	SAC1-1	Drying	Cement + Coarse Malmesbury + Ulula Fly Ash.	1400	1	1
	SAC1-2					
	SAC1-3	Autogenous				
	SAC1-4					
SAC2	SAC2-1	Drying	Cement + Coarse Malmesbury + Ulula Fly Ash.	1400	2	2
	SAC2-2					
	SAC2-3	Autogenous				
	SAC2-4					
SCP2	SCP2-1	Drying	Cement + Ulula Fly Ash + Propylene Glycol.	1400	-	2
	SCP2-2					
	SCP2-3	Autogenous				
	SCP2-4					
ACP2	ACP2-1	Drying	Cement + Coarse Malmesbury + Propylene Glycol.	1400	2	-
	ACP2-2					
	ACP2-3	Autogenous				
	ACP2-4					

As the aim of this section is not only to record the physical shrinkage strains of specimens but also investigate the effects of density and different SCM's, the deviation in target density has also been noted as an important factor to control. To ensure useable and reliable results, the mass of each cylinder cast has been recorded after stripping and compared to the mix target density, the results of which are indicated in Table 5-2.

Table 5-2: Shrinkage Testing Casting Densities

Mix	Target Density (kg/m ³)	Average Casting Density (kg/m ³)	Percentage off target density (%)
C12	1200	1227.9	-2.32
C14	1400	1467.03	-4.79
C16	1600	1659.75	-3.73
SC1	1400	1443.31	-3.09
SC2	1400	1466.88	-4.77
AC1	1400	1455.54	-3.97
AC2	1400	1411.46	-0.82
SAC	1400	1342.93	4.076
SAC2	1400	1452.61	-3.76
SCP2	1400	1467.77	-4.84
ACP2	1400	1462.71	-4.48

5.1.1.1 Drying Shrinkage

When isolating the results of cement-only mixes C12, C14 and C16 as shown in Figure 5-2, it may be seen that for the total period of one hundred and fifty-five days of drying, there appears to be an inverse relationship between the total amount of drying shrinkage exhibited and dry density. With a dry density of 1200 kg/m³, mix C12 exhibits the most drying shrinkage whilst mixes C14 and C16 with respective densities of 1400 kg/m³ and 1600 kg/m³ show an approximately linear decrease in total drying shrinkage strains shown visually in Figure 5-1. The total drying shrinkage strain exhibited by mix C14 is approximately 8.7% lower than that of mix C12, whilst mix C16 shows a final drying strain approximately 15.82% lower than mix C12. This is contrary to findings from other research efforts such as that of (Nambiar, 2014), where it has been found that drying shrinkage strains decrease with increasing foam content attributed to the increase in hydrated cement paste present in more dense mixes. This has been attributed to the fact that more hydrated cement paste results in a larger quantity of evaporable water and shrinkable medium. However, this study also concluded that in contradiction to previous studies where removal of water from macro-pores is said to have no effect on shrinkage, in LWFC specimens increasing the void content may actively contribute to increasing shrinkage due to lowered material stiffness – an explanation which seems to correlate well with the findings in Figure 5-1.

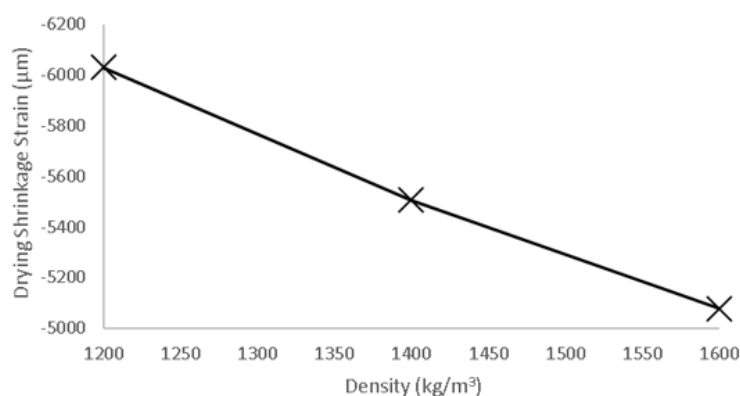


Figure 5-1: Relationship between total drying shrinkage and density

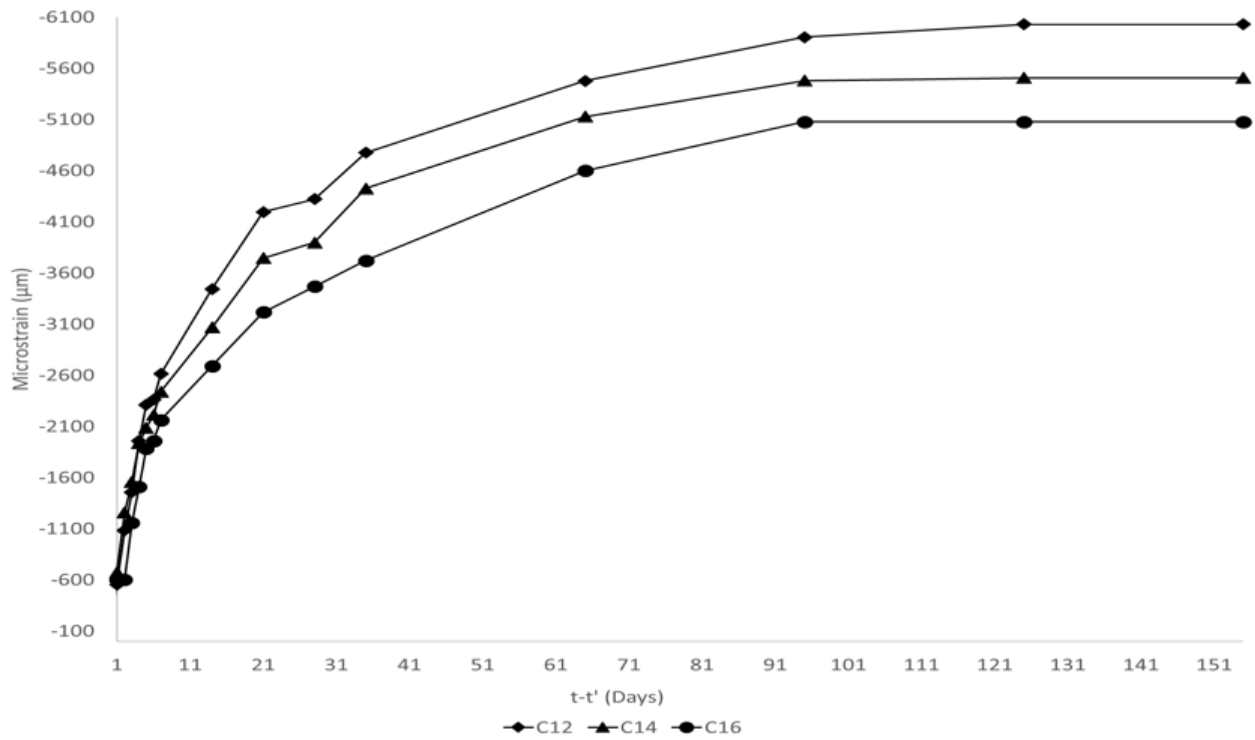


Figure 5-2: Total Drying Shrinkage Cement-only mixes

It is now possible to investigate the effects of various SCM's on total drying shrinkage strain. As stated in Chapter 3, the effects of varying SCM's have been investigated by comparing the total drying shrinkage experienced for mixes containing different types and quantities of SCM's to each other and to the control cement-only mix C14 all with a dry density of 1400 kg/m^3 . By first investigating the results of mixes AC1 and AC2, it is possible to see that the inclusion of fly ash in both mixes results in a decrease in the total drying shrinkage exhibited compared to mix C14. Mix AC1 with an ash-cement ratio of one shows an ultimate strain of $4468 \text{ } \mu\text{m}$ equating to an 18% reduction in total drying shrinkage, whilst mix AC2 with an ash-cement ratio of two sees an ultimate strain value of $4293 \text{ } \mu\text{m}$ and a 22% reduction in total drying shrinkage strain. These results are indicated visually by Figure 5-3. Overall, the results indicate that the inclusion of fly ash in LWFC on average is seen to decrease the total drying shrinkage strain by approximately 20%. This corroborates findings by (Nambiar, 2014) mentioned in Chapter 2 where mixes containing fly ash as a cement filler were also seen to exhibit smaller drying shrinkage strains than a control mix without fly ash and the same density. It should also be noted that in contradiction to this study, mix AC1 containing a smaller quantity of fly ash exhibited higher drying shrinkage strains than mix AC2 which contained a larger quantity of fly ash, whereas other research seems to indicate the opposite relationship. The reduction in drying shrinkage strains for LWFC mixes containing fly ash may be attributed to the reduction in the total amount of Portland cement present, thus reducing the total amount of hardened cement paste and shrinkable material. In addition, the inclusion of fly ash in LWFC aids in increasing long term strength and stiffness, reduces total water demand and lowers the heat of hydration which, in turn, increases the shrinkage restraining capacity of the specimen.

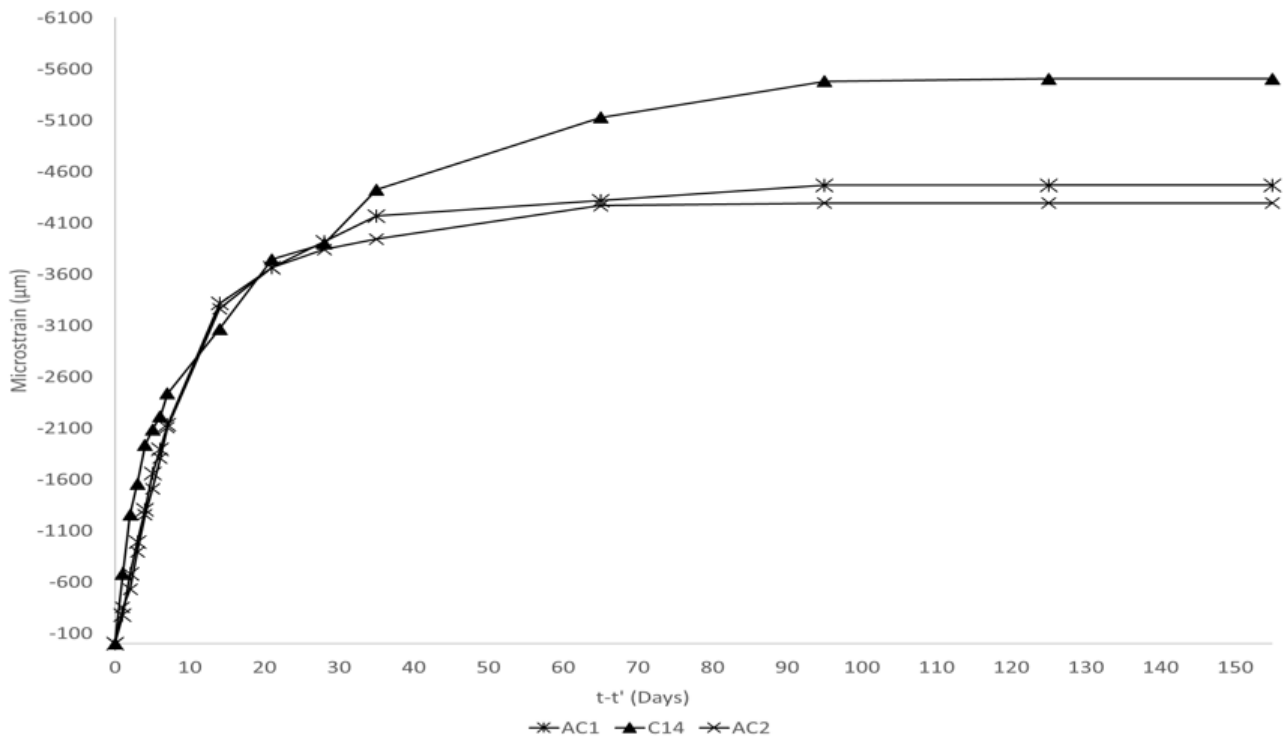


Figure 5-3: Total Drying Shrinkage Cement-ash mixes

Moving along from fly ash, the effects of including sand as a partial cement filler in LWFC are to be investigated. To investigate these effects, mix SC1 with a sand-cement ratio of one and mix SC2 with a sand-cement ratio of two have been used. It may immediately be seen that when compared to the control mix C14, both mixes containing sand significantly reduce the total amount of drying shrinkage exhibited and lie in the lower half of the mixes tested. Mix SC1 and mix SC2 exhibited ultimate shrinkage strains of 3115 μm and 2812 μm equating to a reduction of approximately 43.42% and 48.92% respectively. On average, it may be seen that the inclusion of sand in LWFC reduces drying shrinkage strains by approximately 46% compared to the control mix C14 and 32.35% compared to mixes containing fly ash. This result again corroborates findings highlighted in Chapter 2 where, not only was it found that mixes containing sand as a partial cement filler reduced drying shrinkage significantly compared to control mixes, but also that mixes containing sand exhibited lower shrinkage values than those containing fly ash. The reduction in drying shrinkage values is attributed to the higher shrinkage restraining capacity of stiffer sand particles, the lower overall content of shrinkable hardened cement paste and the lower water demand of mixes containing sand. Figure 5-4 indicates the final one hundred and fifty five day drying shrinkage strains of the LWFC mixes containing sand compared to the control mix C14.

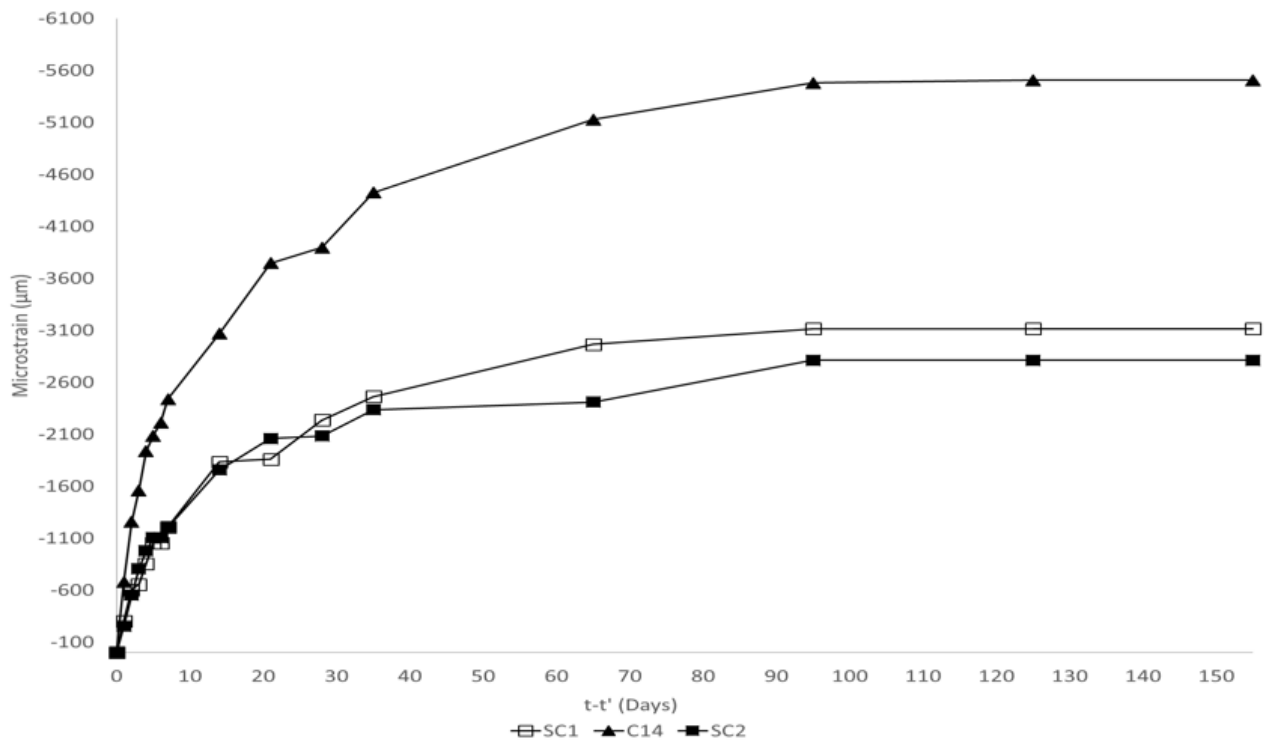


Figure 5-4: Total Drying Shrinkage Cement-sand mixes

As the effects of both fly ash and sand as partial cement fillers investigated, it is now possible to investigate their combined effect by examining the results obtained from mix SAC1 and SAC2. To begin this examination, it may be noted that mix SAC1 exhibits an ultimate drying shrinkage strain of 3916 μm whilst mix SAC2 exhibits 2635 μm resulting in a 28.86% and 52.13% reduction from the control respectively as shown in Figure 5-5. The overall drying shrinkage reduction for a combination of both fly ash and sand is approximately 40.5% when compared to the control mix C14. Mix SAC1 utilises an ash-cement and sand-cement ratio of one whilst mix SAC2 utilises an ash-cement and sand-cement filler ratio of two. With this in mind, drying shrinkage behaviour which appears to validate the results obtained for the mixes containing only sand and only fly ash may be seen. Mix SAC1 which has a lower quantity of both sand and fly ash exhibits higher drying shrinkage strains in line with the lower fly ash content and lower sand content of mix AC1 and SC1 respectively. By increasing the total content of sand and fly ash such as in mix SAC2, SC2 and AC2, the total drying shrinkage exhibited is decreased even further. In fact, mix SAC1 indicates a reduction of 12% compared to mix AC1 which contains only fly ash, however, it must be noted that mix SC which contains only sand in the equivalent ratio still exhibits strains approximately 20.5% lower than the combination. The results of mix SAC2, however, show a reduction in total drying shrinkage of approximately 6.3% and 38% respectively when compared to mixes SC2 and AC2. These results indicate that whilst only fly ash, only sand and a combination of the two are effective at reducing drying shrinkage, it appears that replacement in higher quantities and the inclusion of sand are the most effective ways of doing so.

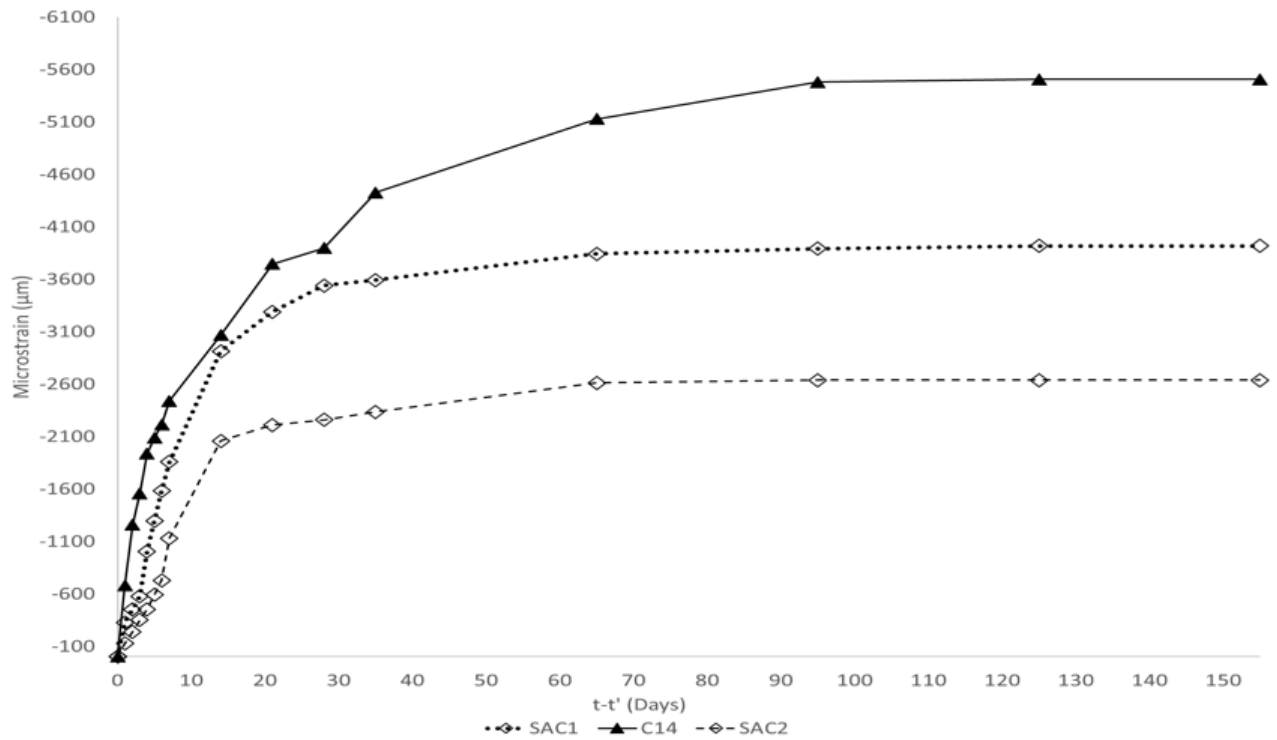


Figure 5-5: Total Drying Shrinkage Cement-sand-ash mixes

As the effects of both fillers in their varying quantities and combinations addressed, it is now possible to highlight the results obtained by adding 7% (by weight of cement) propylene glycol to the mixes. To attain these results, mixes which were anticipated to reveal the lowest levels of drying shrinkage from literature review (SC2 and AC2) have been dosed with the glycol compound. Mix ACP2 with an ash-cement ratio of two and mix SCP2 with a sand-cement ratio of two exhibited shrinkage strain values of 3013 μm and 1331 μm respectively. This equated to a reduction in shrinkage strain values from the control mix C14 of 45.27% and 75.82% respectively with an average reduction of 60.55% indicated visually in Figure 5-6 and Figure 5-7. In addition to this, it can also be seen that the inclusion of propylene glycol results in a reduction of drying shrinkage strains of 29.82% and 52.67% compared to equivalent mixes AC2 and SC2 which contain fillers in the same ratios but do not include the glycol. As uncovered in Chapter 2, these results seem to validate the results obtained by (Chindapasirt & Rattanasak, 2011) where the inclusion of only propylene glycol resulted in a decrease of approximately 40%. The vast reduction in drying shrinkage strains exhibited by mixes ACP2 and SCP2 is attributed to the combined effects of both the individual influences of the fly ash and sand and the hydrophilic behaviour of glycol compounds which makes the removal of free water from the specimen and evaporation far more difficult.

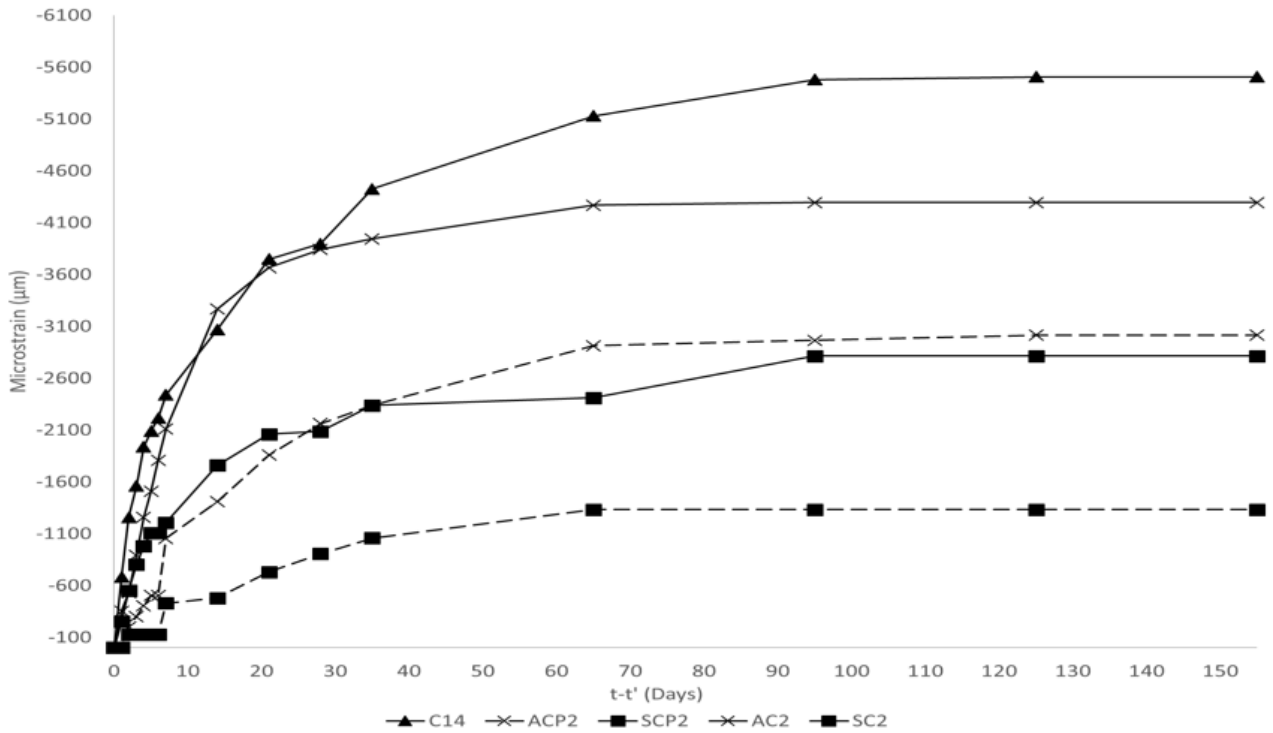


Figure 5-6: Total Drying Shrinkage PG mixes

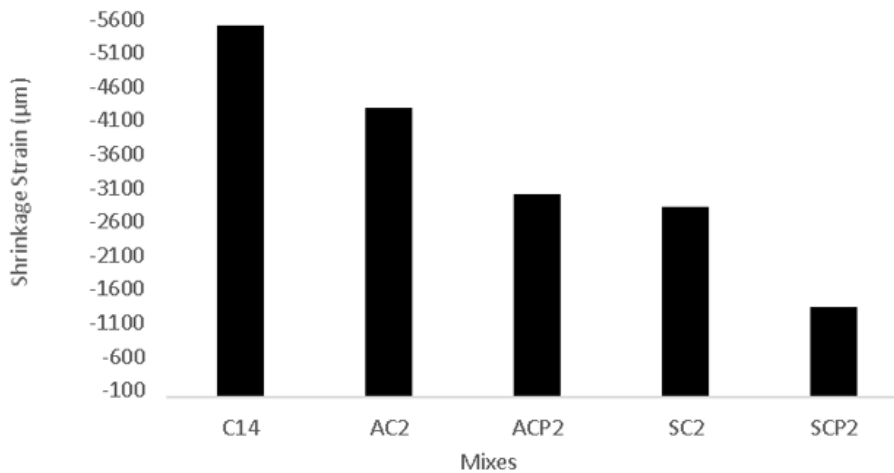


Figure 5-7: PG Drying Shrinkage Reductions

Investigating the overall results shown by Figure 5-8 for the total period of drying equal to one hundred and fifty-five days there are several interesting points to take note of. To begin it is possible to note that the maximum amount of drying shrinkage strain experienced is that of mix C12 which is equal to 6030 μm . This is then followed by mix C14 and mix C16 with drying shrinkage strains equal to 5505 μm and 5076 μm respectively. This is then followed by mixes AC1 and AC2 which both contain fly ash and exhibited final drying shrinkage strains of 4468 μm and 4293 μm respectively. From this point onwards there appears to be a break in the pattern of grouped mixes with the next highest drying shrinkage strain

exhibited by mix SAC1 equal to 3916 μm which is then followed by mix SC1 which displays a final drying shrinkage value of 3115 μm . At the lower end of the drying shrinkage spectrum are mixes SC2 and SAC2 displaying strain values of 3013 μm and 2812 μm respectively with the second least drying shrinkage strain equal to 2635 μm shown by mix ACP2 and closing off the field with the least drying shrinkage is that of mix SCP2 equal to 1331 μm .

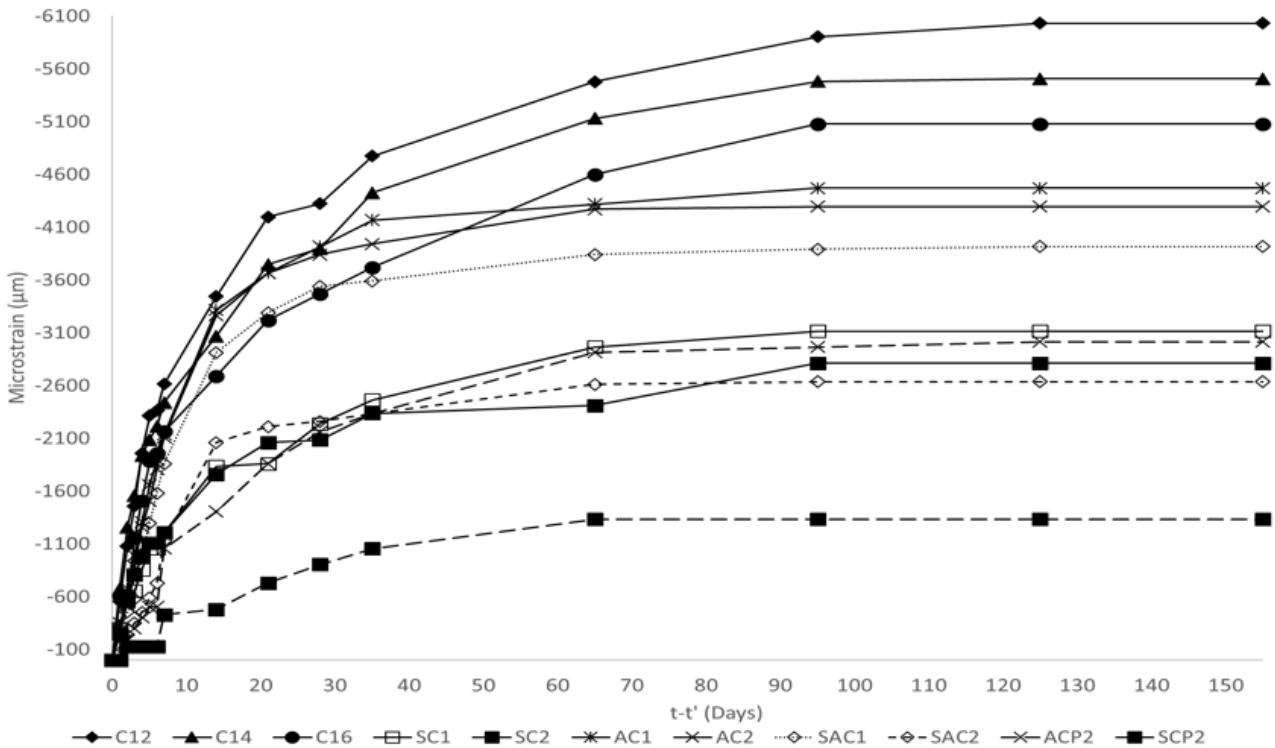


Figure 5-8: Total Drying Shrinkage all mixes

Table 5-3 and Figure 5-9 provide numerical and graphical indications of the total drying shrinkage strains recorded over the one hundred and fifty-five day period.

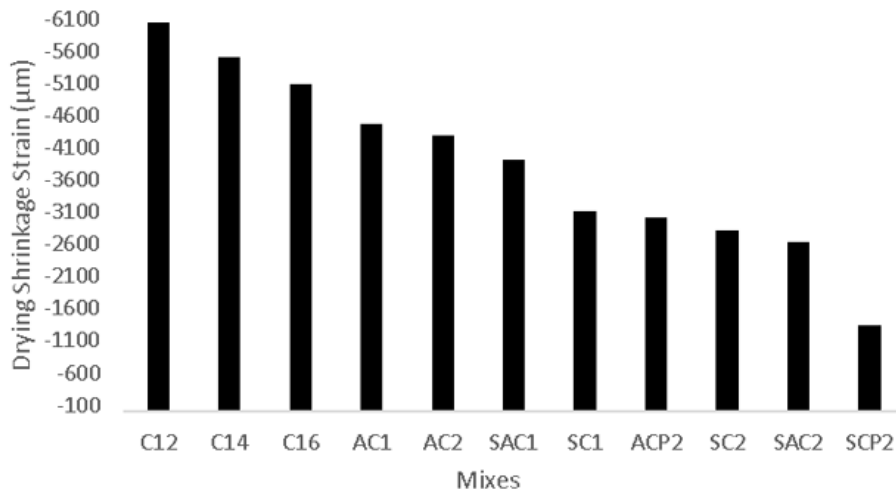


Figure 5-9: Total Drying Shrinkage Strains

Table 5-3: Total Drying Shrinkage Strains

Mix	C12	C14	C16	AC1	AC2	SAC1	SC1	ACP2	SC2	SAC2	SCP2
$\mu\text{m}(155)$	-6030	-5505	-5076	-4468	-4293	-3916	-3115	-3013	-2812	-2635	-1331

The results of total drying shrinkage strains recorded over the one hundred and twenty-five day period may be summarised as follows:

Table 5-4: Total Drying Shrinkage Summary

Mix	Average difference from control mix 1B (%)	Average difference from mixes containing only sand (%)	Average difference from mixes containing only fly ash (%)
C12	+ 8.7		
C14	-	+ 46.48	+20.89
C16	-15.82		
SC1	-43.42		
SC2	-48.92	-	-35.35
AC1	-18.84		
AC2	-22.02	+32.35	-
SAC1	-28.86		
SAC2	-52.13	+9.53	-25.23
ACP2	-45.27		
SCP2	-75.82	-26.71	-50.42

Using six order polynomial lines of best fit for the recorded data, it is possible to approximate the time taken for each mix variation to reach 50% of its ultimate shrinkage strain as the following:

Table 5-5: Time taken to reach 50% final drying shrinkage

Mix	155 Day microstrain	50% microstrain	$t_{50\%}$ (Days)
C12	-6029.58	-3014.79	8.96
C14	-5504.98	-2752.49	8.8
C16	-5076.26	-2538.13	9.8
SC1	-3115.40	-1557.70	10.7
SC2	-2811.80	-1405.90	8.3
AC1	-4468.13	-2234.06	7.6
AC2	-4293.03	-2146.51	7.5
SAC1	-3916.15	-1958.07	8.03
SAC2	-2635.41	-1317.73	9.3
ACP2	-3013.39	-1506.69	15.4
SCP2	-1331.85	-665.92	19

In addition, the total loss of moisture expressed as the average percentage of the total mass lost for each mix variation over the entire period of drying is given in Table 15-6 and shown visually in Figure 5-10. The mass records may be found in Appendix B.

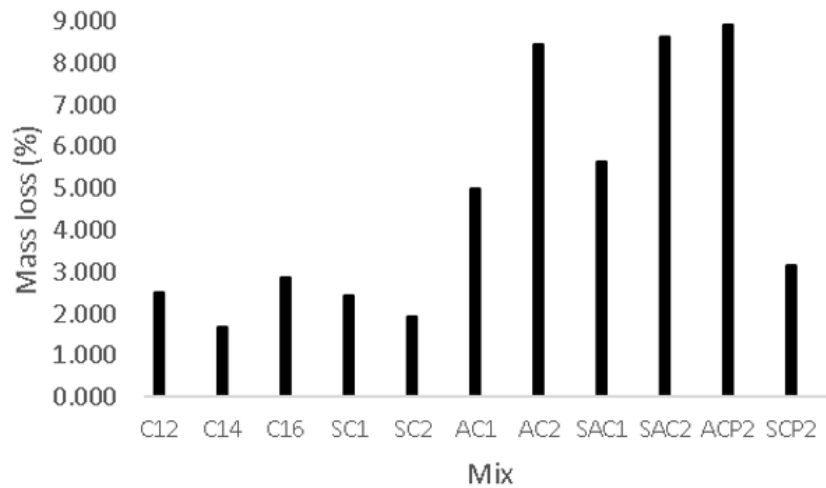


Figure 5-10: Drying Shrinkage Mass Loss

Table 5-6: Drying Shrinkage Mass Loss

Mix	Average mass loss over drying period (%)
C12	-2.513
C14	-1.685
C16	-2.850
SC1	-2.437
SC2	-1.926
AC1	-4.981
AC2	-8.453
SAC1	-5.651
SAC2	-8.624
ACP2	-8.896
SCP2	-3.157

Investigating the moisture loss values of all the drying shrinkage samples, it may be seen that the addition of sand in all mixes results in a reduction in the amount of moisture lost from the samples. It is also possible to note that the inclusion of fly ash results in a marked spike in total moisture loss with the values increasing with increasing ash content. Interestingly, mixes ACP2 and SCP2 which both exhibited smaller shrinkage strains are seen to exhibit higher moisture losses than their equivalent mixes. This may indicate that there may be additional mechanisms involved in the addition of propylene glycol. For the sand and ash mixes, however, the relationship between moisture loss and total shrinkage strain appears to agree with research such as (Nambiar, 2014). Also interesting to note is that whilst cement-only mixes exhibited the highest shrinkage strains, they also exhibited the lowest moisture losses. The volume of hydrated cement paste is responsible for volumetric shrinkage, this result also agrees with the research uncovered.

5.1.1.2 Autogenous Shrinkage

When investigating the one hundred and fifty-five day autogenous shrinkage strains for the mixes containing only cement shown in Figure 5-11, there are a handful of interesting points to take note of and variations from the results obtained for drying shrinkage strains. Firstly, it is possible to see that in contradiction to the drying shrinkage results where an inverse relationship has been found between dry density and total shrinkage, the results obtained for autogenous shrinkage indicate that the most dense 1600 kg/m³ mix C16 exhibited the most shrinkage strain followed by the least dense 1200 kg/m³ mix C12 with the lowest of the three being the control 1400 kg/m³ mix C14. Although not significant, the final autogenous shrinkage values of mix C12 and C16 are approximately 4.3% and 7.4% higher than mix C14 respectively. The findings of mix C16 exhibiting the highest autogenous shrinkage corroborate findings presented by (Nambiar, 2014) in Chapter 2 where higher shrinkage values have been previously linked to the higher amounts of hydrated cement paste. Where the results become more interesting is when comparing mixes C12 and C14. If the previous statement relating to cement paste content and shrinkage strains is valid, it would be expected that the more dense mix C14 would exhibit higher shrinkage strains than the less dense mix C12. As this is not the case, this may suggest an interesting relationship between cement paste content and foam volume where increasing both the cement paste and foam volume result in increased shrinkage and self-desiccation under sealed conditions. The “Goldilocks zone” therefore, may be a balance between the two resulting in an overall decrease of autogenous shrinkage strains such as that of mix C14 which lies in the middle of the cement content and foam range.

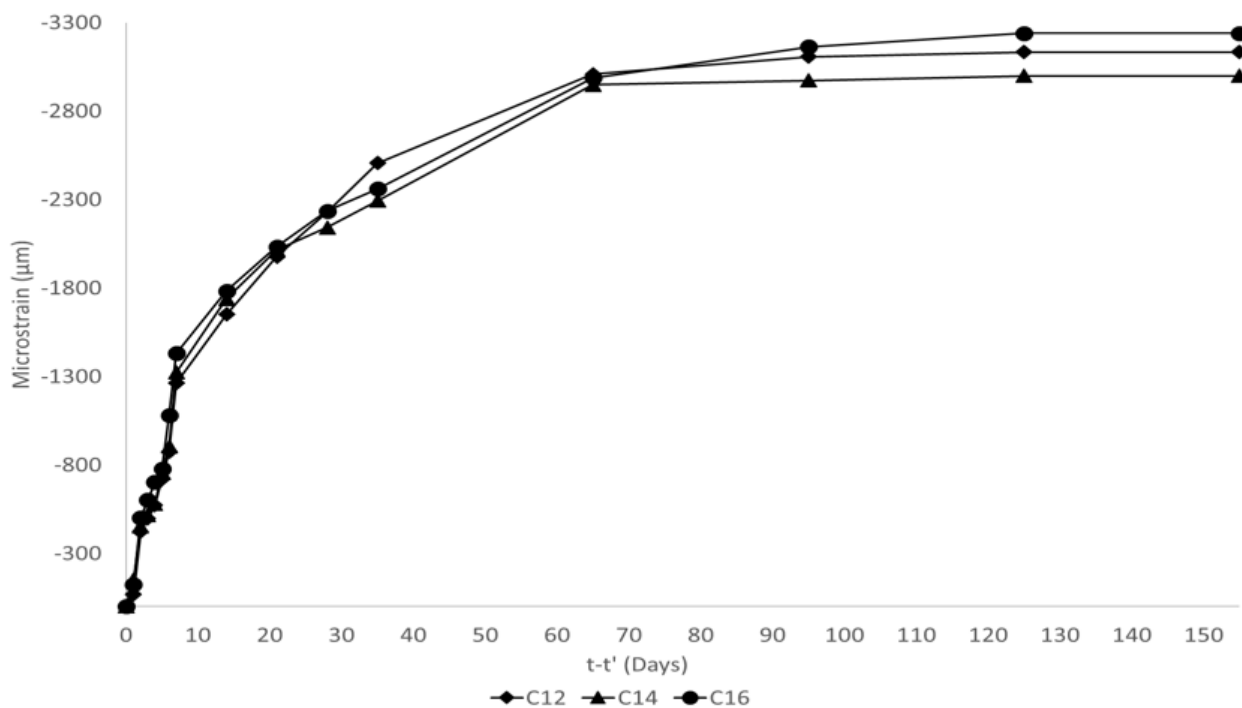


Figure 5-11: Total Autogenous Shrinkage Cement-only mixes

Delving into the effects of the various SCM's used, it is possible to note various differences compared to the results obtained for drying shrinkage analysis. Firstly, whereas both mixes containing fly ash exhibited higher shrinkage values than sand mixes under drying conditions, it appears that under sealed conditions the filler/cement ratio plays a more important role. Mixes SC1 and AC1 with a filler/cement ratio of one reduce autogenous shrinkage values compared to control mix C14 by approximately 18% and 36% respectively with an average reduction of 27% whilst mixes SC2 and AC2 with a filler cement ratio of two reduce the autogenous shrinkage strains by 48% and 57% respectively with an average reduction of approximately 51%. On average, the inclusion of fly ash in mixes AC1 and AC2 reduces the autogenous shrinkage strain by approximately 46% whilst the inclusion of sand in mixes SC1 and SC2 results in an average reduction of 32%. These results are shown visually in Figure 5-12 and there are two important things to take note of following these findings.

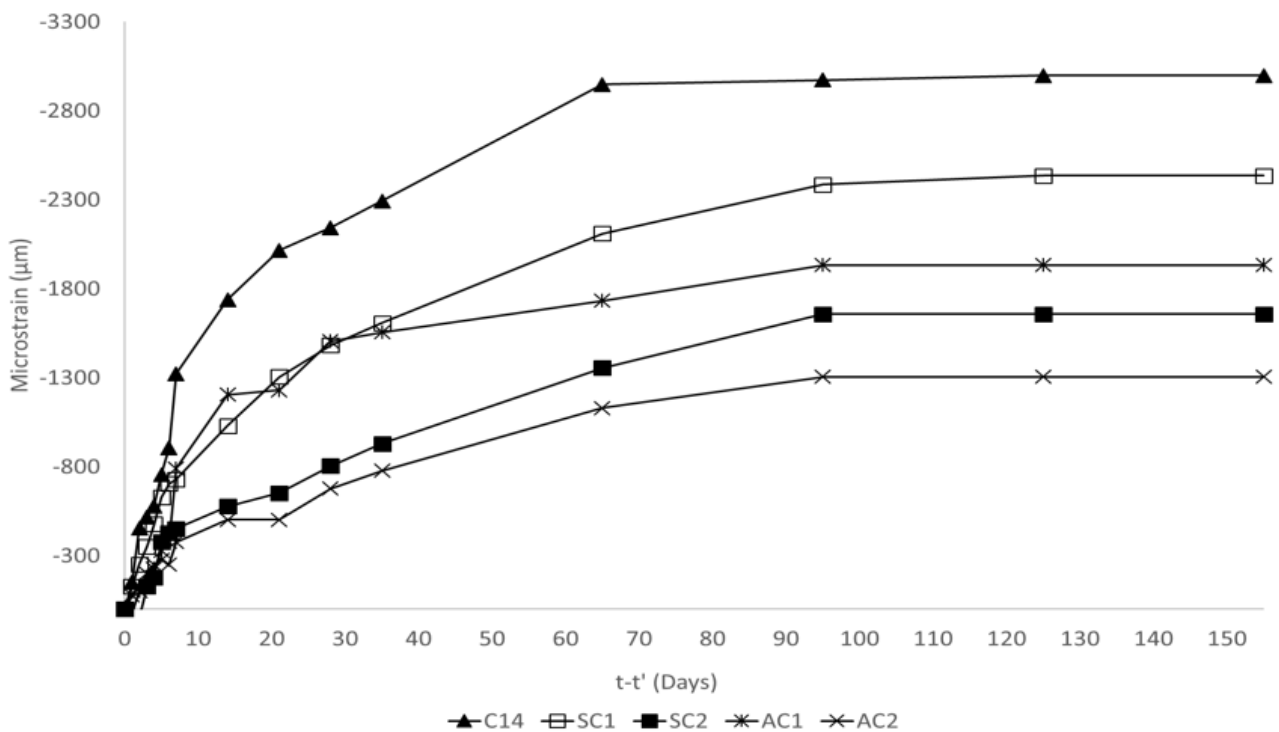


Figure 5-12: Total Autogenous Shrinkage cement-sand & cement-fly ash mixes

It is possible to see that doubling the filler/cement ratio in the LWFC approximately halves the autogenous shrinkage strain values which may be attributed to both the reduction in total hydrated cement paste and the increase in higher shrinkage restraining particles. By decreasing the total content of cement and cement paste, it is possible to effectively reduce the total amount of self-desiccation experienced whilst increasing the percentage of fillers both reduces the total content of this paste and increases the percentage of stiffer shrinkage restraining particles. The second thing to note which contradicts the findings of drying shrinkage experiments is that mixes containing fly ash appear to be more effective at reducing shrinkage under sealed conditions. As fly ash has a higher water demand than sand and is also slower to hydrate and react than cement, the sealed conditions may allow for more of the water to be

absorbed by the fly ash thus minimising the amount of water absorbed and used for self-desiccation of the shrinkable cement paste. As there is no possibility for free water to be lost to the environment in mixes containing sand under sealed conditions, it is more likely that this free water is absorbed by the shrinkable cement paste rather than the sand particles thus, increasing the total shrinkage strain exhibited when compared to fly ash mixes. This may also explain the increase in shrinkage restraining capacity of mixes by doubling their respective filler/cement ratios.

Perhaps the most interesting of the results obtained for autogenous shrinkage analysis is that of mixes SAC1 and SAC2 containing a combination of both fly ash and cement. Whereas under drying conditions these mixes had a relatively average effect on reducing the total amount of shrinkage strain, under sealed conditions it appears that the combination of both fillers has the most profound effect on reducing shrinkage. Mix SAC1 exhibits a reduction in autogenous shrinkage values of approximately 77% whilst mix SAC2 is capable of reducing these strains by up to 94% when compared to control mix C14 as indicated by Figure 5-13. With an average shrinkage reducing capacity of approximately 85%, the combination of both fillers shows the most promising results of all fillers and ratios tested for sealed conditions. It is interesting to note again that increasing the filler/cement ratio increases the shrinkage restraining capacity, although the difference between doubling the filler/cement ratios from mix SAC1 to SAC2 is less profound than mixes containing only one type of filler. The superior reduction in autogenous shrinkage strains for mixes containing both types of fillers may be attributed to a combination of the effects mentioned in the previous paragraph. By combining the positive aspects of both fillers, the final result appears to a system in which the sum result is greater than its parts.

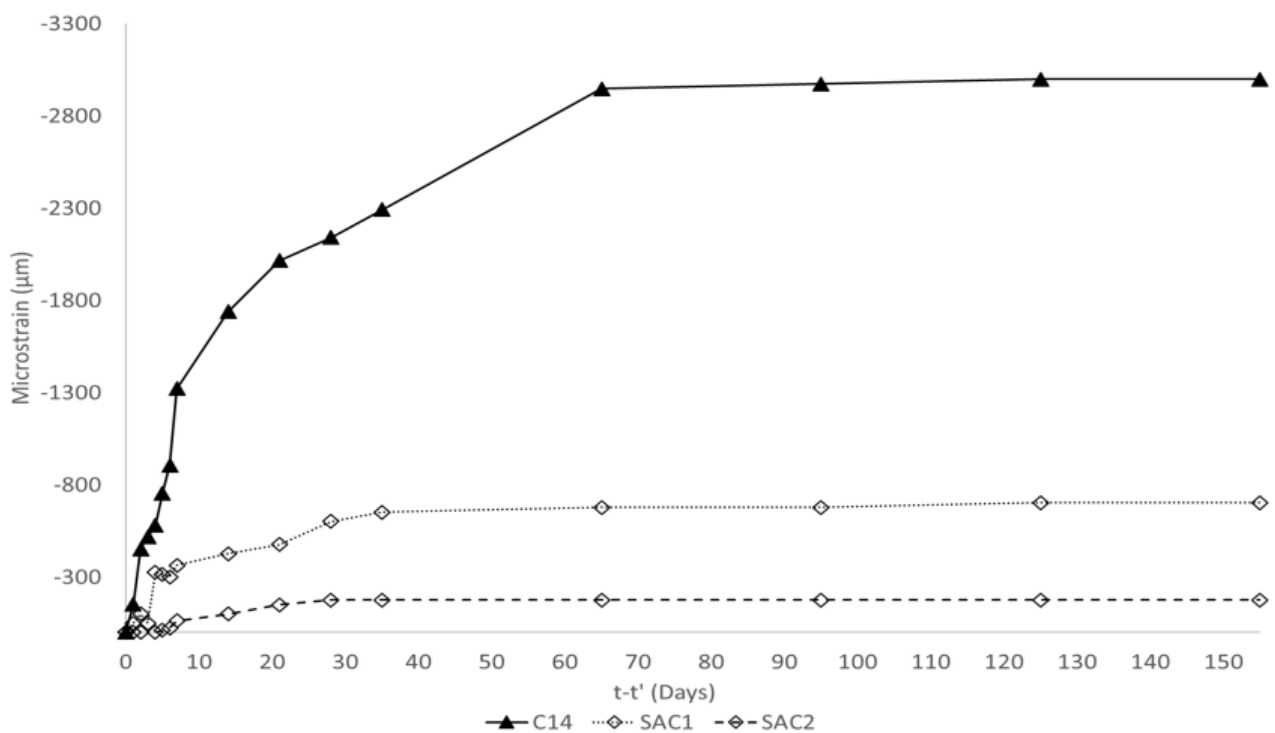


Figure 5-13: Total Autogenous Shrinkage cement-sand-fly ash mixes

When investigating the last of the mixes tested for autogenous shrinkage, it may be seen that the mix variations with the second most effective shrinkage restraining capacity are that of mixes ACP2 and SCP2 with an average reduction of approximately 82% compared to the control mix C14. As both mixes contain filler/cement ratios of two and the benefits of increasing the content of fillers as it pertains to autogenous shrinkage has already been investigated, the additional reduction in mixes ACP2 and SCP2 are attributed to the inclusion of propylene glycol. Mix ACP2 with an ash/cement ratio of two exhibits a reduction in shrinkage strains of approximately 73%, whilst mix SCP2 with a sand/cement ratio of two exhibits a reduction of approximately 90%. Interesting to note is that whilst equivalent mix SC2 containing sand was less effective at reducing shrinkage than mix AC2 containing fly ash, the inclusion of propylene glycol results in mix ACP2 containing fly ash being less effective at reducing shrinkage than mix SCP2 containing sand. Figure 5-14 and Figure 5-15 indicate the results of mixes SC2 and AC2 compared to equivalent mixes ACP2, SCP2 and control mix C14. It is possible to see that the inclusion of propylene glycol results in a 38.5% improvement for mix ACP2 containing fly ash whilst mix SCP2 containing sand sees an 82% improvement. The difference in values between ACP2 and SCP2 may be attributed to the glycol compounds ability to attract water particles and increase surface tension. As free water is absorbed by both the cement and fly ash particles in mix ACP2, stronger attraction forces may mean the glycol may be less effective at preventing this absorption than in mix SCP2 where water is mainly absorbed by the cement particles only.

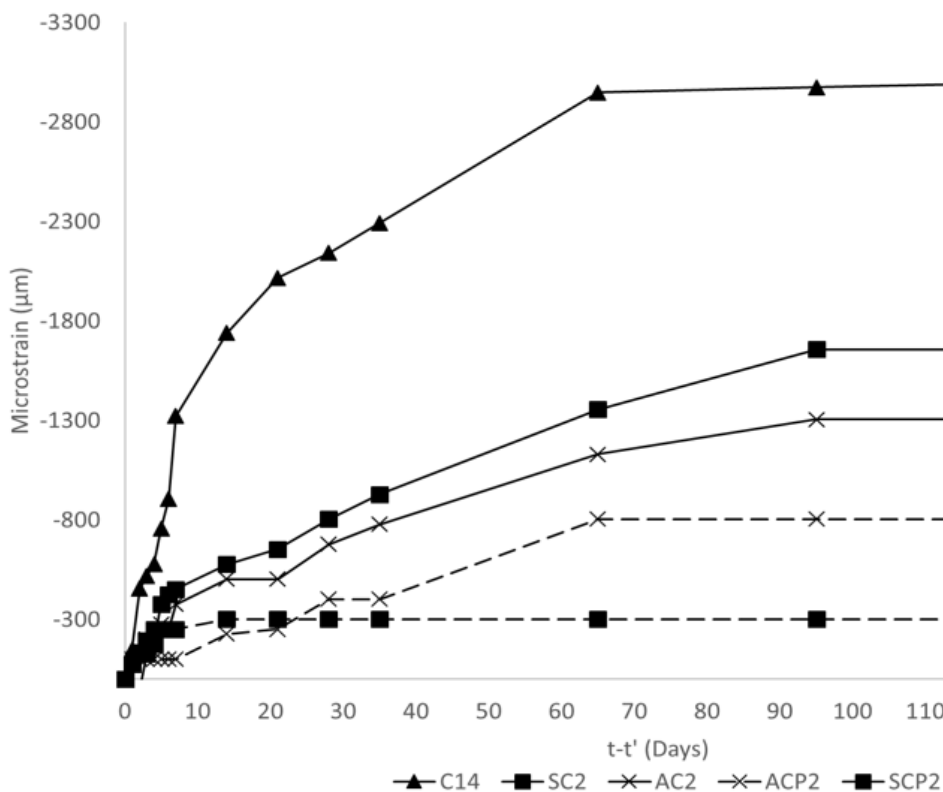


Figure 5-14: Total Autogenous Shrinkage PG mixes

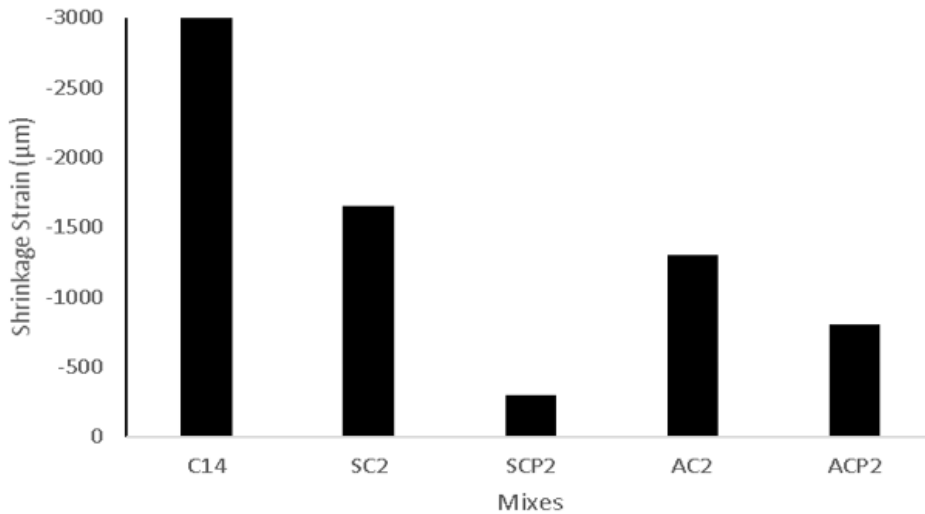


Figure 5-15 PG Autogenous Shrinkage Reductions

Figure 5-16 and Figure 5-17 depict the graphical results obtained for autogenous shrinkage strain values recorded for each mix variation over a one hundred and fifty-five day period. The strains depicted in this section are indicative of averaging each cylinder and mix, however, the full records may be seen in Appendix C. Table 5-7 is also provided for a numerical indication of the total autogenous shrinkage strains recorded over the period of testing.

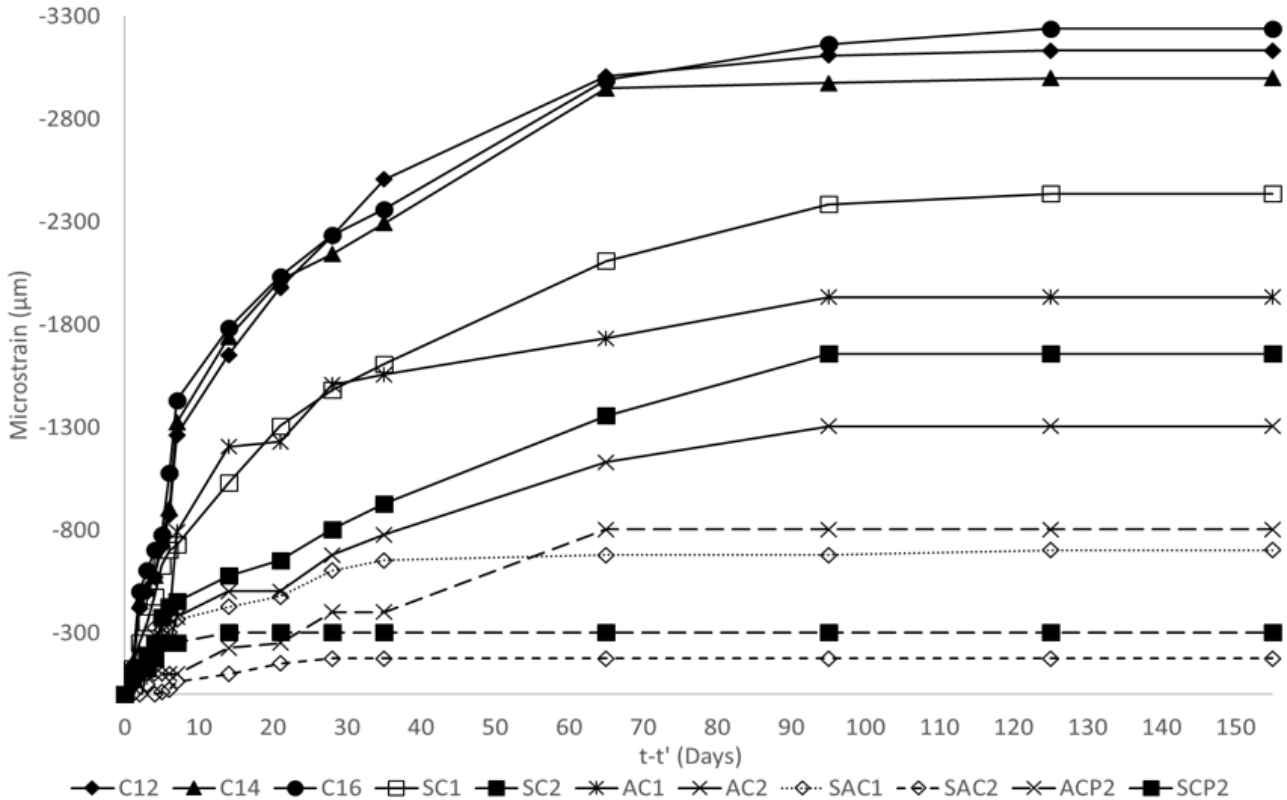


Figure 5-16: Total Autogenous Shrinkage Strains

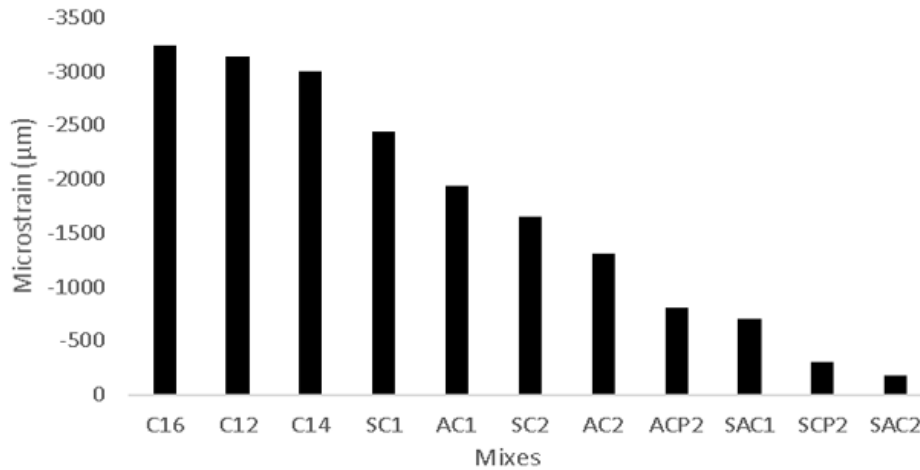


Figure 5-17: Total Autogenous Shrinkage Strains Comparison

Table 5-7: Total Autogenous Shrinkage Strain Values

Mix µm(155)	C16	C12	C14	SC1	AC1	SC2	AC2	ACP2	SAC1	SCP2	SAC2
	-3239	-3132	-2998	-2435	-1932	-1656	-1305	-803	-702	-301	-175

When considering the overall results presented in Table 5-7 for autogenous shrinkage strain measurements there are a variety of interesting points and relationships which can immediately be seen. Firstly, it may be noted that even in almost perfectly sealed conditions, the maximum amount of shrinkage strain exhibited exceeds 3000 µm whereas NWC typically experiences autogenous shrinkage strains between 20 µm – 100 µm which generally accounts for 10%-20% of the total shrinkage strains (Gribniak, Kaklauskas & Bacinskas, 2008). In fact on average, the autogenous shrinkage strains have been determined to contribute approximately 41% to the total drying shrinkage strain in all of the LWFC mixes tested. Table 5-8 indicates the maximum drying shrinkage and autogenous shrinkage values recorded after a period of one hundred and fifty-five days for each mix. It may be seen that the cement only mixes experience autogenous shrinkage strains on average approximately 57% of their equivalent drying shrinkage strains whilst mixes containing sand only show the greatest contribution of autogenous shrinkage equal to approximately 68.5% of their equivalent drying shrinkage strains. On the lower end are the mixes containing only fly ash with approximately 37% autogenous shrinkage contribution followed by mixes containing propylene glycol at a value of approximately 25%. Interestingly, the lowest autogenous shrinkage contributors are that of the mixes containing both fly ash and sand with the mix consisting of a filler/cement ratio of two seeing the lowest contribution at approximately 7%.

Table 5-8: Autogenous Shrinkage Contribution

Mix	Maximum Shrinkage (μm)		Autogenous Contribution (%)	Average
	Drying	Autogenous		
C12	6030	3132	51.94	
C14	5505	2998	54.46	56.74
C16	5076	3239	63.81	
SC1	3115	2435	78.17	68.53
SC2	2812	1656	58.89	
AC1	4468	1932	43.24	36.82
AC2	4293	1305	30.40	
SAC1	3916	702	17.93	12.28
SAC2	2635	175	6.64	
ACP2	3013	803	26.65	24.63
SCP2	1331	301	22.61	
			Average	41.34

Continuing on and focusing on autogenous shrinkage results specifically, it is possible to see that the mixes containing only cement exhibit the largest shrinkage strains even in sealed conditions. It can be seen that the highest autogenous shrinkage strain recorded is that of mix C16 at approximately 3238 μm closely followed by mixes C12 and C14 with final shrinkage values of approximately 3132 μm and 2998 μm respectively. In a deviation from the results obtained from drying shrinkage strains, it is possible to see that the next two highest autogenous shrinkage strains are attributed to mixes SC1 and AC1 both with filler/cement ratios equal to one. The maximum autogenous shrinkage strain recorded for mixes SC1 and AC1 are 2435 μm and 1932 μm respectively. Increasing the filler/cement ratio from one to two, it may be seen that the next two lowest shrinkage strain values are that of mix SC2 and AC2 at 1656 μm and 1305 μm respectively. Beyond this point, it may be seen that autogenous shrinkage strains move down into the triple digits with mix ACP2 equal to 803 μm followed by the first combination mix SAC1 with a filler/cement ratio of one and final shrinkage strain of 702 μm . Closing off the section are mixes SCP2 and SAC2 both with sand/cement ratios of two with final autogenous shrinkage strains of 301 μm and 175 μm respectively. The results of total autogenous shrinkage strains recorded over the one hundred and twenty-five period may be summarised as follows:

Table 5-9: Autogenous Shrinkage Summary

Mix	Average difference from control mix 1B (%)	Average difference from mixes containing only sand (%)	Average difference from mixes containing only fly ash (%)
C12	+ 4.3		
C14	-	+ 34.48	+48.19
C16	+7.41		
SC1	-18.8		
SC2	-44.8	-	+20.92
AC1	-35.56		
AC2	-56.5	-20.92	-
SAC1	-76.6		
SAC2	-94.16	-78.54	-72.87
ACP2	-73.0		
SCP2	-90	-73.00	-65.86

Additionally, the importance of sufficiently sealing samples tested for autogenous shrinkage is imperative in assessing the effects of internal mechanism in the absence of moisture transfer. Like the drying shrinkage samples, autogenous shrinkage samples have also been weighed and their masses recorded before testing and after testing to assess the degree of moisture loss. Shown in Table 5-10 and Figure 5-18, most if not all samples tested for autogenous shrinkage exhibit acceptable moisture losses with the only exception being the sand mixes at slightly over one percent. The mass records may be found in Appendix D.

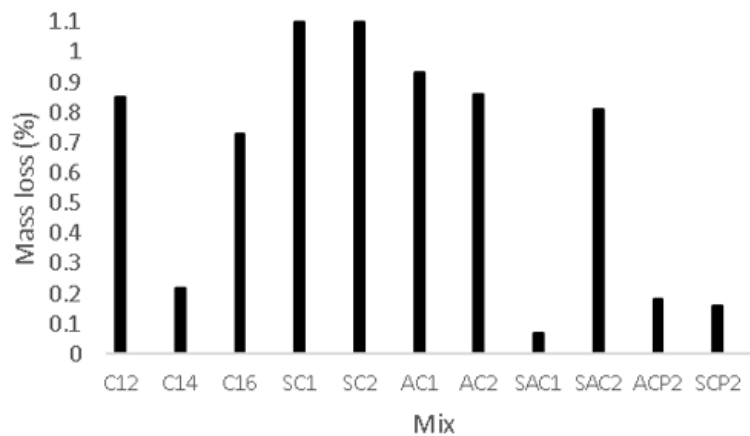


Figure 5-18: Autogenous Shrinkage Mass Losses

Table 5-10: Autogenous Shrinkage Mass Losses

Mix	Average mass loss over drying period (%)
C12	-0.85
C14	-0.22
C16	-0.73
SC1	-1.1
SC2	-1.1
AC1	-0.93
AC2	-0.86
SAC1	-0.07
SAC2	-0.81
ACP2	-0.18
SCP2	-0.16

5.1.2 Creep Testing

The results presented in this section provide the physically obtained drying creep and basic creep strain values for a selected number of the chosen test mixes. Due to unexpected delays and limitations on the total amount of creep frames available for use, only four LWFC mix variations have been tested for a total of twenty-eight days each. Only mixes which exhibited compressive strengths above 10MPa have been chosen for testing as well as those containing fly ash as this filler is a staple in LWFC mix design. Therefore, two standard ash mixes have been tested with ash/cement ratios of one and two with a third ash mix containing 7% propylene glycol also being tested. In addition, investigating the effects of different fillers has also been identified as a main research objective and thus, the strongest LWFC containing only sand has also been tested for creep strains. For each mix variation e.g. AC1, two cylinders each with two separate sets of gauge studs have been cast for both drying creep and basic creep values and the averages taken of both the two sets of gauge studs on each cylinder and both cylinders for each mix variation. In total for both drying creep and basic creep strain measurements, sixteen cylinders have been cast using a total of sixty-four stainless steel gauge studs and measurements have been recorded over a period of twenty eight days equating to a total of three hundred and fifty-two individual data points being captured. Table 5-11 provides information on each mix variation tested for creep strain measurements as well as their respective identification codes which are used going forward. This table only provides a brief indication of the mix variations, however, full mix composition tables may be found in Table 3-2.

Table 5-11: Creep Testing Mixes

Mix	Cylinders	Drying/ Basic	Description	ρ (kg/m ³)	s/c	a/c
SC1	SC1-1	Drying	Cement + Coarse Malmesbury Sand.	1400	1	-
	SC1-2					
	SC1-3	Basic				
	SC1-4					
AC1	AC1-1	Drying	Cement + Ulula Fly Ash.	1400	-	1
	AC1-2					
	AC1-3	Basic				
	AC1-4					
AC2	AC2-1	Drying	Cement + Ulula Fly Ash.	1400	-	2
	AC2-2					
	AC2-3	Basic				
	AC2-4					
ACP2	ACP2-1	Drying	Cement + Ulula Fly Ash + Propylene Glycol.	1400	-	2
	ACP2-2					
	ACP2-3	Basic				
	ACP2-4					

As all mixes tested for basic creep and drying creep have a density of 1400 kg/m^3 and been chosen to investigate the effects of varying SCMs rather than density, controlling the target density has been identified as a vitally important step. To ensure useable and reliable results, the mass of each cylinder cast has been recorded after stripping and compared to the mix target density, the results of which are indicated in Table 5-12.

Table 5-12: Creep Testing Casting Densities

Mix	Target Density (kg/m^3)	Average Casting Density (kg/m^3)	Percentage off target density (%)
AC1	1400	1446.53	-3.32
SC1	1400	1385.03	+1.07
AC2	1400	1352.20	+3.41
ACP2	1400	1401.53	-0.11

As indicated in the experimental design, cylinders subjected to compressive creep testing are to be uniaxially loaded to a value approximately 40% of their ultimate compressive strength to ensure linear behaviour throughout the duration of testing. Compression cylinders from each batch have been cast for supplementary testing and tested according to SANS 5863 as laid out in Section 3.5. The compressive strength results for each mix tested for creep and are indicated in Table 5-13.

Table 5-13: Creep Testing Compressive Strengths

Mix	Description	F_{ult} (kN)	F_{ult} (MPa)	$F_{40\%}$ (kN)	$F_{40\%}$ (MPa)
AC1	Cem + FA (a/c =1)	80.6	10.26	32.24	4.11
SC1	Cem + Sand (s/c=1)	94.6	12.05	37.84	4.82
AC2	Cem + FA (a/c=2)	114.2	14.54	45.68	5.82
ACP2	Cem + FA (a/c = 2) + 7% PG	130.1	16.56	52.04	6.63

5.1.2.1 Drying Creep

Figure 5-19 depicts the results obtained for drying creep strain values recorded for each mix variation over a twenty-eight day period. The strains depicted in this section are indicative of averaging each cylinder and mix, however, the full records may be seen in Appendix E.

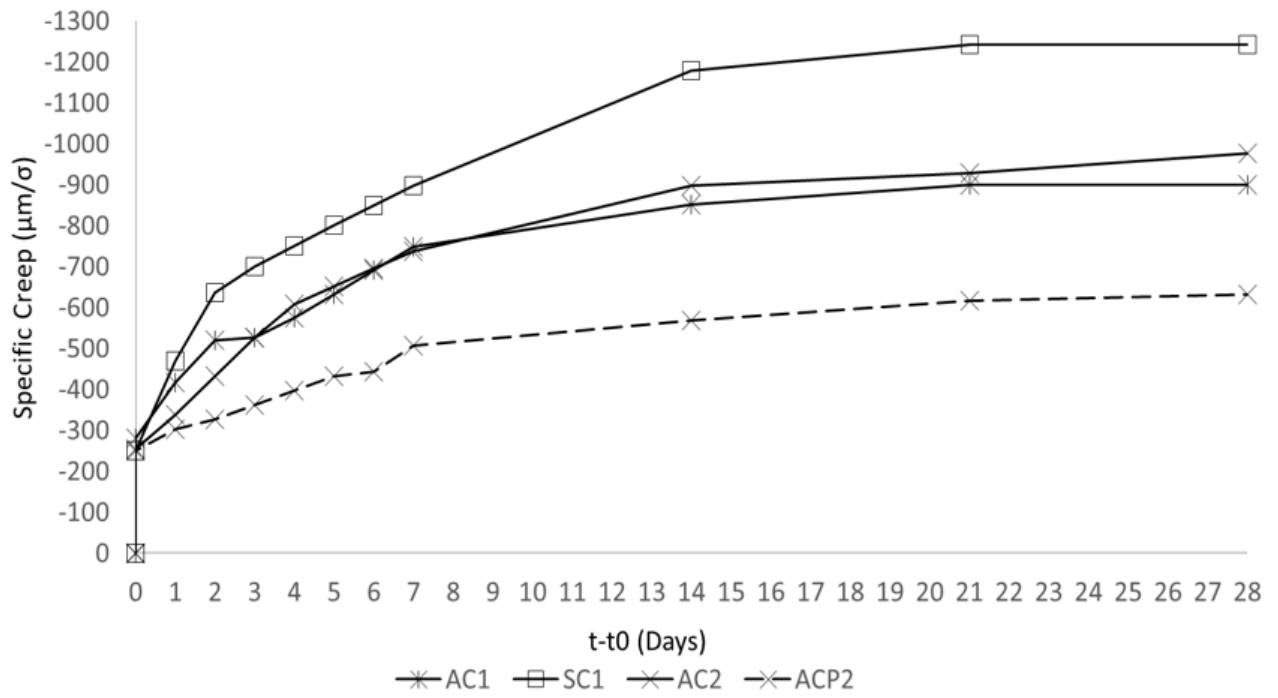


Figure 5-19: Total Drying Creep Strains

Table 5-14 and Figure 5-20 provide numerical and graphical indications of the maximum total drying creep strains recorded over the twenty-eight day period.

Table 5-14: Total Drying Creep Values

Mix	AC1	SC1	AC2	ACP2
µm(28)	-3696	-5982	-5675	-4193

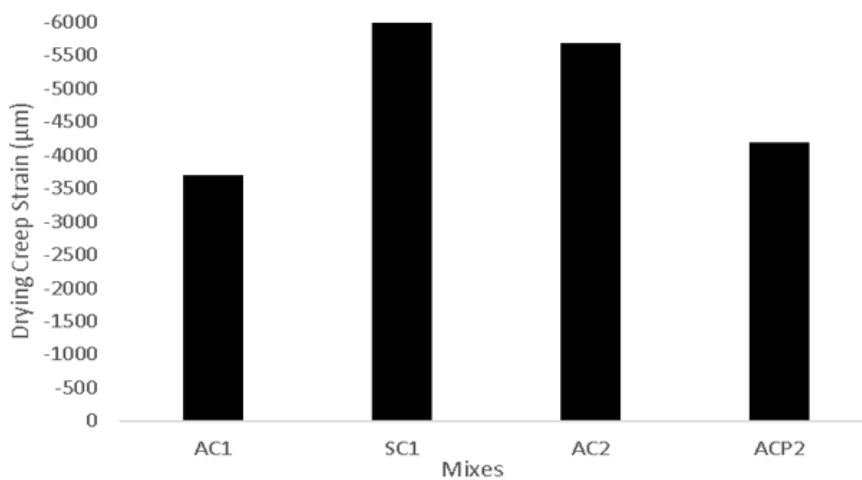


Figure 5-20: Total Drying Creep Strains Comparison

In addition to recording the maximum creep strains over the twenty-eight day period, the initial strain at the time of loading is also an important factor to consider for each design mix. As stated previously, loading the specimens with a force equal to forty percent of their ultimate compressive strength ensures linear behaviour is maintained. With this known, the applied stress together with the strains recorded immediately after loading may be used to attain an approximate estimation of the twenty-eight day Young's Modulus as follows:

$$E = \frac{\sigma_0}{\varepsilon_0} \quad (\text{Equation 5.1})$$

Table 5-15 indicates the recorded strain values immediately after loading, the value of the initial applied stress as indicated in Table 5-13 and the approximated twenty-eight day Young's modulus calculated therefrom.

Table 5-15: Creep Tests Young's Modulus

Mix	Description	F _{ult} (MPa)	F _{40%} (MPa)	ε ₀ (μm)	E ₂₈ (GPa)
AC1	Cem + FA (a/c =1)	10.26	4.11	-1157	3.55
SC1	Cem + Sand (s/c=1)	12.05	4.82	-1207	4
AC2	Cem + FA (a/c=2)	14.54	5.82	-1481	3.93
ACP2	Cem + FA (a/c = 2) + 7% PG	16.56	6.63	-1657	4

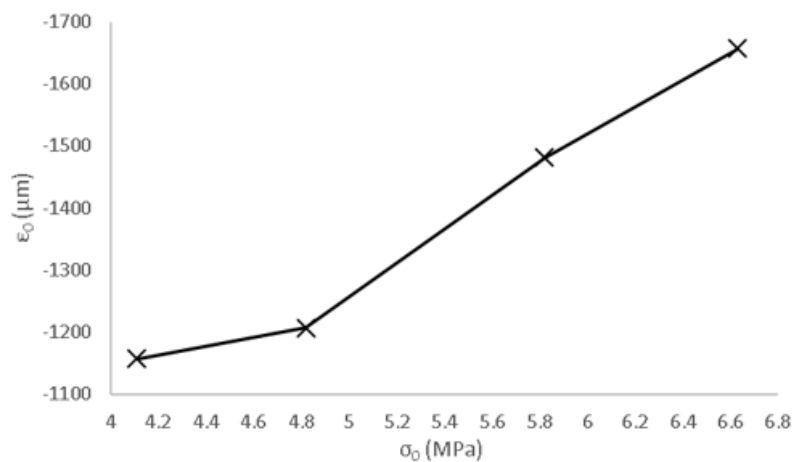


Figure 5-21: Relationship between initial strain and loading force

By referring back to Figure 5-19 and Table 5-14, it is possible to see that in contradiction to the results obtained for drying shrinkage testing, the maximum drying creep exhibit from all of the samples tested is that of mix SC1 with a final strain value equal to approximately 5982 μm . Following on closely from this, is the second highest drying creep strain equal to approximately 5675 μm attributed to mix AC2 which contains fly ash with an ash/cement ratio of two. Moving further down the line, mix ACP2 which contains fly ash with an ash/cement ratio of two and propylene glycol exhibits a final twenty-eight day drying creep strain value of approximately 4193 μm . Rounding off the results with the least drying creep strain is that of mix AC1 with an ash/cement ratio of one which exhibits a final drying shrinkage value of approximately 3696 μm .

Taking these values into consideration, it may be noted that mix AC2 exhibits drying creep strains approximately 5% lower than mix SC1 containing only sand, whilst mix ACP2 and mix AC1 exhibit reductions in drying creep strains of approximately 30% and 38% respectively. There are also several interesting things to take note of. Firstly, it may be noted that both the highest and lowest drying creep strains are attributed to the mixes containing sand and fly ash respectively both with a filler cement ratio equal to one. This is in contradiction to drying shrinkage testing where mixes containing only sand have been seen to exhibit smaller strains. The results of drying creep tests seem to correlate more closely to those of autogenous shrinkage where for both filler/cement ratios the mixes containing sand exhibited higher strains. This may suggest that contrary to research, creep and shrinkage may be effected in different ways by different and more complex internal mechanisms. The additional shrinkage restraining capacity attributed to sand particles may be lost under initial loading resulting in higher strains as time progresses. As fly ash is known to increase the long-term strength of LWFC, this may also be one reason why sand mixes are seen to contract more under sustained loading than those containing fly ash. The issue of free water and moisture loss may also be addressed. The lower absorption capacity of sand particles compared to fly ash particles may result in larger amounts of un-hydrated water within the cement paste being made available for removal, thus increasing the volumetric shrinkage of the paste.

Isolating mixes AC1, AC2 and ACP2 which contain only fly ash, there are also a number of interesting observations to take note of which directly contradict findings of the shrinkage tests performed. It may be seen that when measuring unrestrained shrinkage strains, mix AC1 with an ash/cement ratio of one experienced higher shrinkage strains than mix AC2 with an ash/cement ratio of two. In the case of drying creep, mix AC2 which has an ash/cement ratio of two exhibits higher strains than mix AC1 with an ash/cement ratio of one. In fact, mix AC1 exhibits drying creep strains approximately 35% lower than those exhibited by mix AC2. As the addition of fly ash increases the water demand of the mix, higher water quantities in mix AC2 may be the cause of the additional deformation. Comparing mix AC2 and mix ACP2 both with the same ash/cement ratio, it may be seen that the addition of propylene glycol aids in the process of reducing drying creep strains. Similar results are seen as under drying shrinkage

conditions the addition of this glycol compound resulted in reduction of approximately 29% compared to the equivalent mix without it, under drying creep condition the strains are reduced by approximately 26%.

Another way of indicating drying creep results is that of a compliance or specific creep function. As samples for different mixes are loaded with different compressive forces, the use of a specific creep function is one useful way to compare results as each creep curve is related to its accompanying applied stress. As discussed in previous sections, the specific creep curve is attained by dividing the strain recorded at any time during testing by the initial unit stress which results in values expressed as microstrain per unit stress. For each mix included in this drying creep analysis, a specific creep curve has been generated by dividing the time-dependent strains by the initial applied unit stress given in Table 5-13. The results shown in Figure 5-22, provide a better indication of the relative drying creep behaviour of each mix. Mix SC1 which contains only sand, exhibits the highest specific creep strain whilst both fly ash mixes correlate well to one another and exhibit the most intermediate specific creep behaviour of the mixes tested. The lowest of them all when comparing specific creep behaviour is now seen to be mix ACP2 which indicates that the use of propylene glycol may be quite an effective way to reduce the shrinkage and creep behaviour of LWFC.

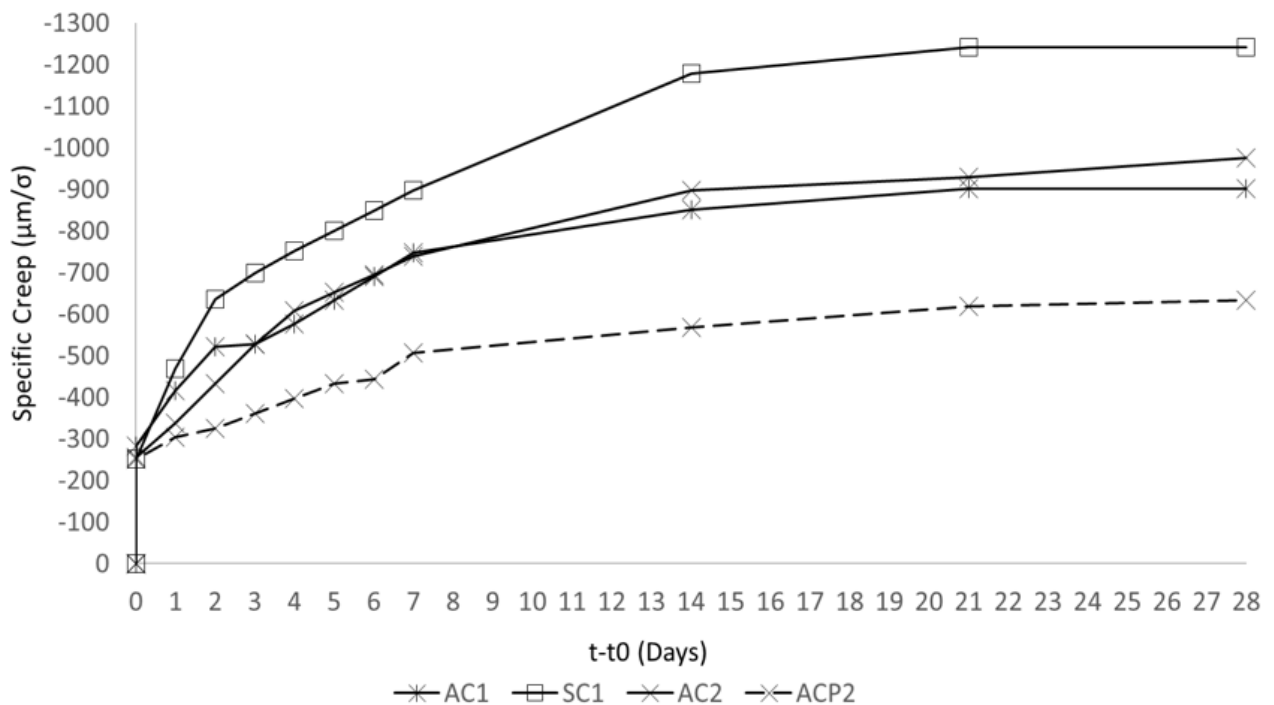


Figure 5-22: Total Specific Drying Creep

The results of total drying creep strains recorded over the twenty-eight day period may be summarised as follows:

Table 5-16: Total Drying Creep Summary

Mix	Average difference from mix containing only sand (%)	Average difference from mix containing only fly ash (a/c = 1) (%)	Average difference from mix containing only fly ash (a/c = 2) (%)	Average difference from mix containing only fly ash + PG (a/c = 2) (%)
AC1	-38	-	-36	+12
SC1	-	+38	+5	+38
AC2	-5	+36	-	+26
ACP2	-30	+12	-26	-

The total loss of moisture expressed as the average percentage of the total mass lost for each mix variation over the entire period of drying is given in Table 5-17. As mixes AC1 and ACP2 are still secured into the loading frame to assess the effects of long-term loading their masses have not been able to be recorded. However, the results for mixes SC1 and AC2 are provided which indicate that under drying conditions, the mixes containing fly ash exhibit higher moisture losses than those with sand which means the increased drying creep behaviour of mix SC1 above mix AC2 must also be attributed to some more complex internal mechanisms other than moisture loss. For an indication of moisture loss in mixes AC1 and ACP2, drying shrinkage mass losses have been used in Table 5-17.

Table 5-17: Drying Creep Moisture Loss

Mix	Average mass loss over drying period (%)
AC1	-4.981
SC1	-1.4
AC2	-5.2
ACP2	-8.896

5.1.2.2 Basic Creep

Figure 5-24 depicts the results obtained for basic creep strain values recorded for each mix variation over a twenty-eight day period. The strains depicted in this section are indicative of averaging each cylinder and mix, however, the full records may be seen in Appendix F.

Table 5-18 and Figure 5-23 provide numerical and graphical indications of the maximum total drying creep strains recorded over the twenty-eight day period.

Table 5-18: Total Basic Creep Strain Values

Mix	AC1	SC1	AC2	ACP2
$\mu\text{m}(28)$	-1107	-755	-2486	-3039

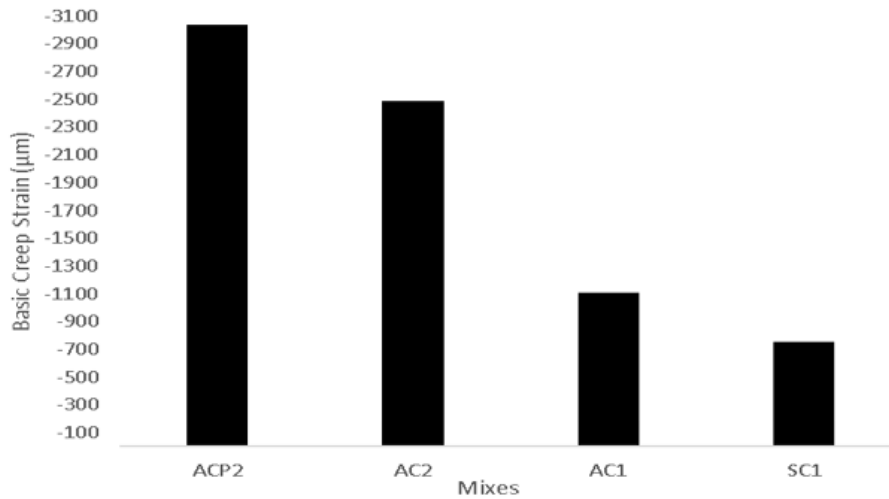


Figure 5-23: Total Basic Creep Strain Comparisons

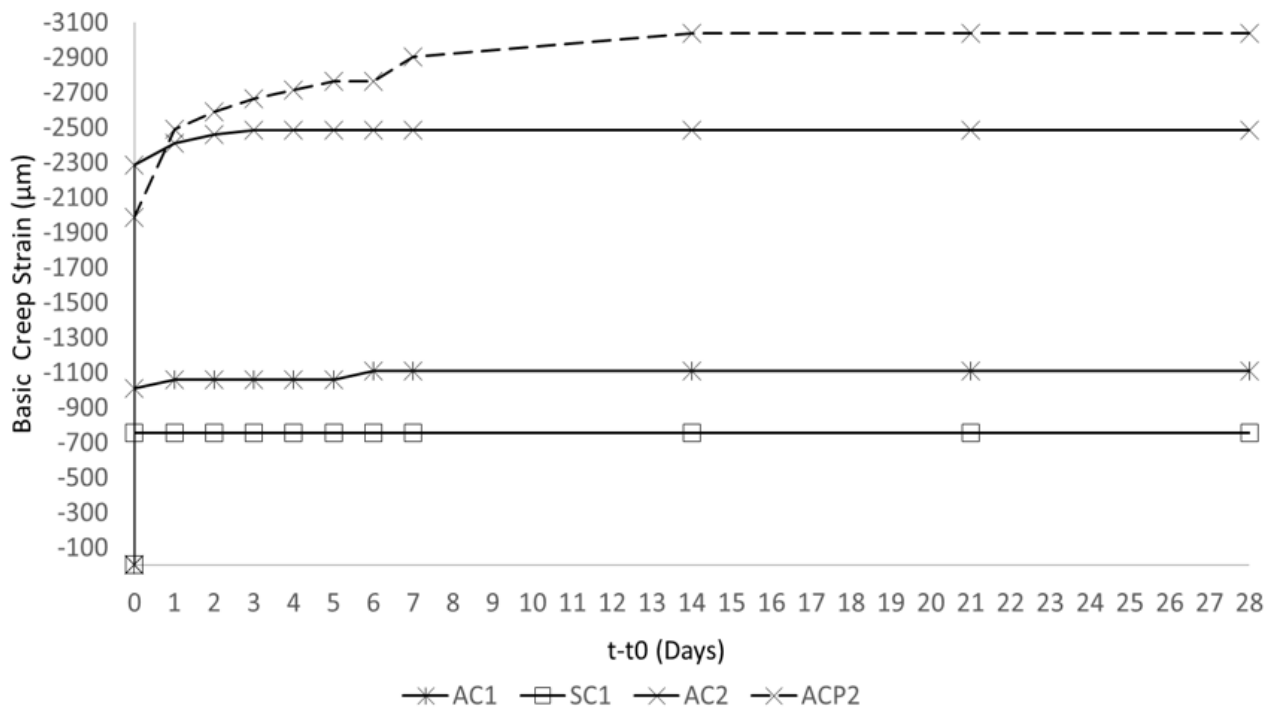


Figure 5-24: Total Basic Creep Strains

Investigating these results for basic creep strain measurements, there are a variety of interesting points and relationships which may immediately be seen. Firstly, it may be seen that even in almost perfectly sealed conditions, the maximum amount of strain exhibited similar to autogenous shrinkage results exceeds 3000 µm. In fact on average, the basic creep strains have been determined to contribute approximately 40% to the total drying creep strains which is also similar to shrinkage results where autogenous shrinkage has been seen to contribute approximately 41% to the total drying shrinkage strain in all of the LWFC mixes tested. Table 5-19 indicates the maximum drying creep and basic creep values recorded after a period of twenty-eight days for each mix.

Mix SC1 which contains only sand has a basic creep contribution of approximately 13%. Whereas under drying conditions mix SC1 exhibited the highest creep strains of approximately 5982 μm , under sealed conditions mix SC1 is seen to exhibit the lowest creep strains of approximately 755 μm . This indicates that a significant portion of the total drying creep experienced is attributed to moisture loss rather than more complex internal mechanisms. The lower water absorption capacity of sand particles may be responsible for the increased drying creep behaviour compared to mixes containing fly ash.

Comparing mix AC1 and mix AC2 which contain fly ash with an ash/cement ratio of one and two respectively, there are also some interesting points to note. Firstly, it may be seen that under sealed conditions mix AC1 exhibits a final creep strain of approximately 1107 μm whilst mix AC2 exhibits a final creep value of 2486 μm . This correlates well with drying creep tests where increasing the ash/cement ratio has been seen to increase the total creep strain. In addition, it may be noted that the basic contribution of mix AC1 is approximately 30% whilst mix AC2 exhibits a basic contribution of approximately 44%. This again indicates that the internal mechanisms, water absorption and hydration products associated with mixes containing fly ash are more significant than those associated with mixes containing sand.

An unforeseen but interesting observation can be seen when investigating the basic creep results obtained for mix ACP2 which contains fly ash with an ash/cement ratio of two and propylene glycol. Whereas under drying shrinkage, autogenous shrinkage and drying creep conditions the use of propylene glycol has been seen to reduce strains, under basic creep conditions the strains exhibited for mix ACP2 are higher than those seen for mix AC2. In fact, mix ACP2 with a final basic creep strain of 3039 μm is approximately 18% higher than equivalent non-glycol mix AC2. This may suggest that as anticipated from research, the hydrophilic nature of glycols means they are far more effective under conditions of drying. Under sealed and compressive conditions where no moisture is lost from the specimen, the glycol compounds may provide the means for some secondary and more complex internal reaction to take place and increase strain values. Additional evidence of this may be seen by investigating the initial strain at the time of loading. Although the slightly stronger and stiffer mix ACP2 exhibits a smaller initial strain than mix AC2, as time progresses the strains are seen to increase above those of mix AC2.

Table 5-19: Basic Creep Contribution

Mix	Maximum Creep (μm)		Basic Contribution (%)
	Drying	Basic	
7	3696	1107	29.95
8	5982	755	12.62
9	5675	2486	43.8
10	4193	3039	72.5
	Average		39.7175

As indicated for the results presented for drying creep strains, another way of indicating basic creep results is that of a compliance or specific creep function. For each mix included in this basic creep analysis, a specific creep curve has been generated by dividing the time-dependent strains by the initial applied unit stress given in Table 5-13. The results shown in Figure 5-25, provide a better indication of the relative basic creep behaviour of each mix. Mix AC2 and mix ACP2 which both contain fly ash with an ash cement ratio of two, correlate well to one another and exhibit the highest specific creep values under sealed conditions. Moving along, it is possible to see that reducing the ash content as in mix AC1 results in reducing the specific creep whilst the lowest specific creep is still attributed to mix SC1 which contains no fly ash at all.

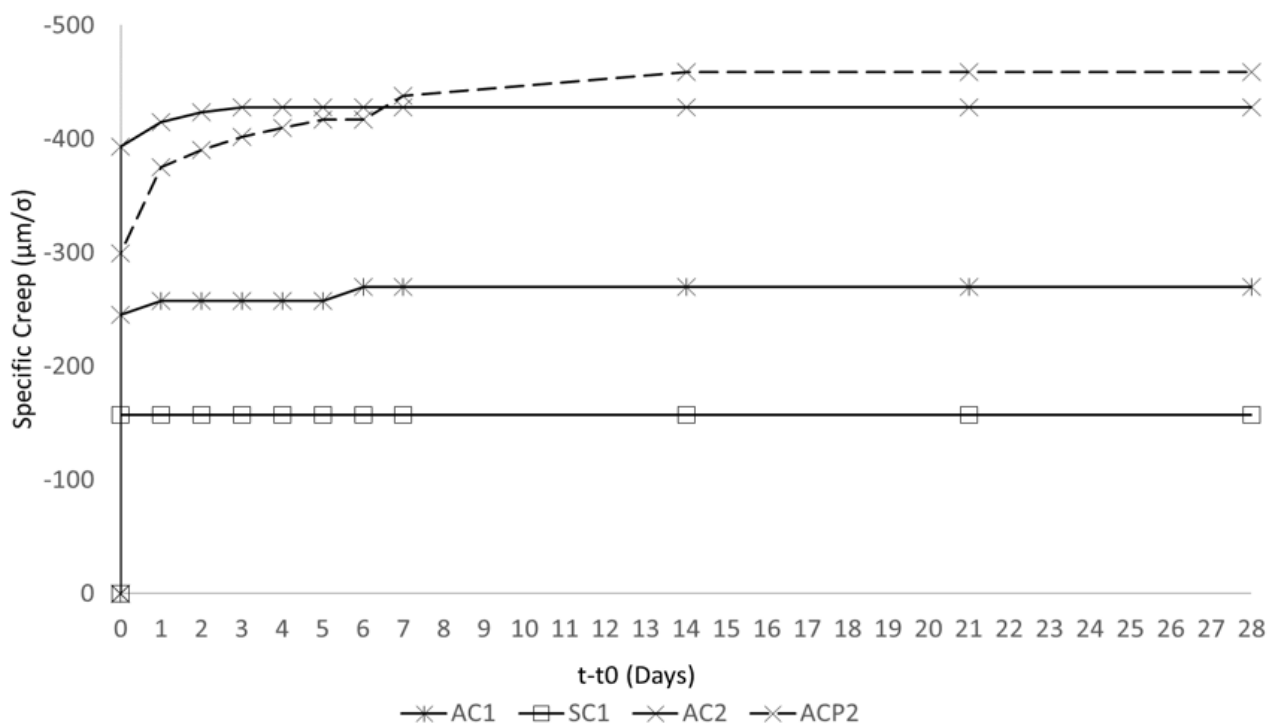


Figure 5-25: Basic Specific Creep Curves

5.2 Physical Results vs Numerical Models

In an effort to investigate the applicability and accuracy of the existing numerical models studied as they pertain to LWFC specifically, each model has been calibrated with properties of the physical LWFC samples tested in Section 5.1. The Fib Model Code 2010 as well as EN1992-1-1 values have additionally been adjusted by the factors specified for LWAC. Only a selected amount of the physically tested samples have been input into the numerical codes to gain an understanding of the adjustments required for the density of LWFC. As the 1200 kg/m^3 and 1600 kg/m^3 mixes represent lowest and highest compressive strengths of all the mixes tested respectively and the shrinkage strain is determined predominantly by environmental conditions, notional size and compressive strength, it is assumed that comparisons and

adjustments to codes based on cement only mixes which vary only in density is sufficient to cover the range of mixes. The input parameters for modelling of shrinkage strains are as follows:

Table 5-20: Numerical Model Experimental Input Parameters

Mix	Density (kg/m ³)	f _c (MPa)	2*(v/s) (mm)	t _s (Days)	w (kg/m ³)
C12	1200	7.14	40	7	320
C14	1400	11.01	40	7	380
C16	1600	24.5	40	7	440

By analysing the results obtained for each numerical model and comparing them to the results obtained from physical testing, the time-dependent shrinkage strains may be adjusted for each to give a preliminary estimate of the adjustment factor required to account for LWFC specifically. The results of all three cement-only mixes before and after adjustment are indicated in Figure 5-26- Figure 5-28 with the adjustment factors applied shown in Table 5-21.

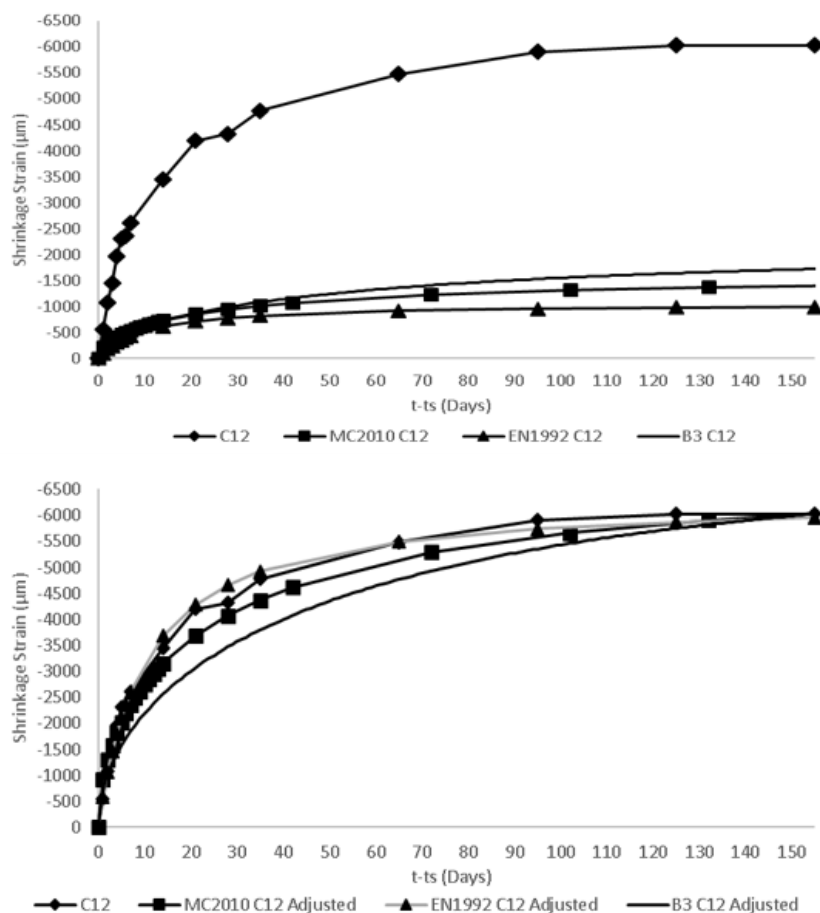


Figure 5-26: Numerical Modelling C12

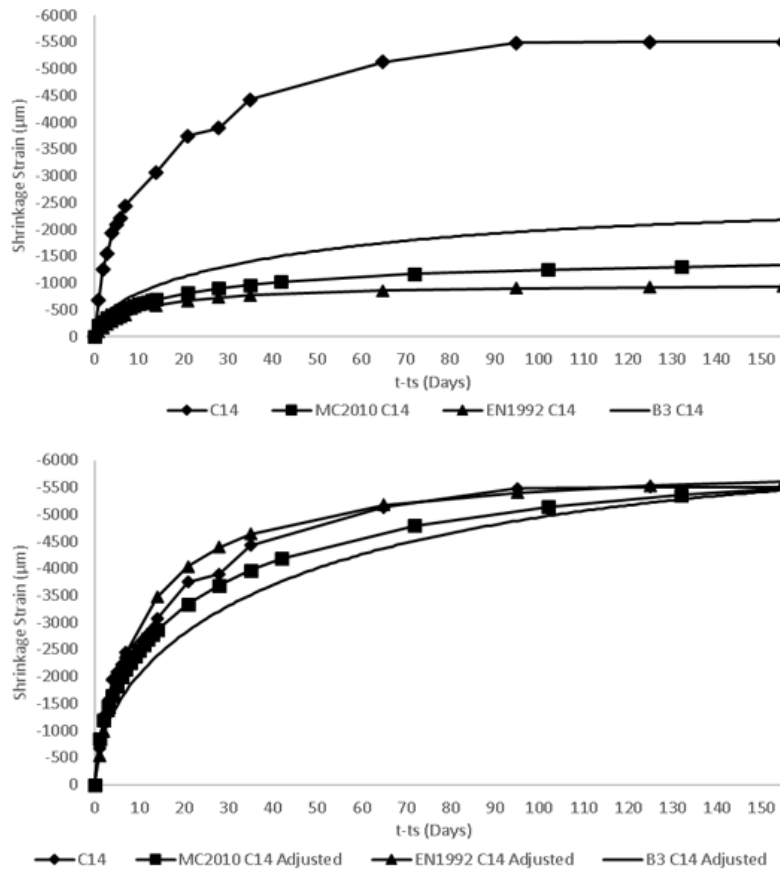


Figure 5-27: Numerical Modelling C14

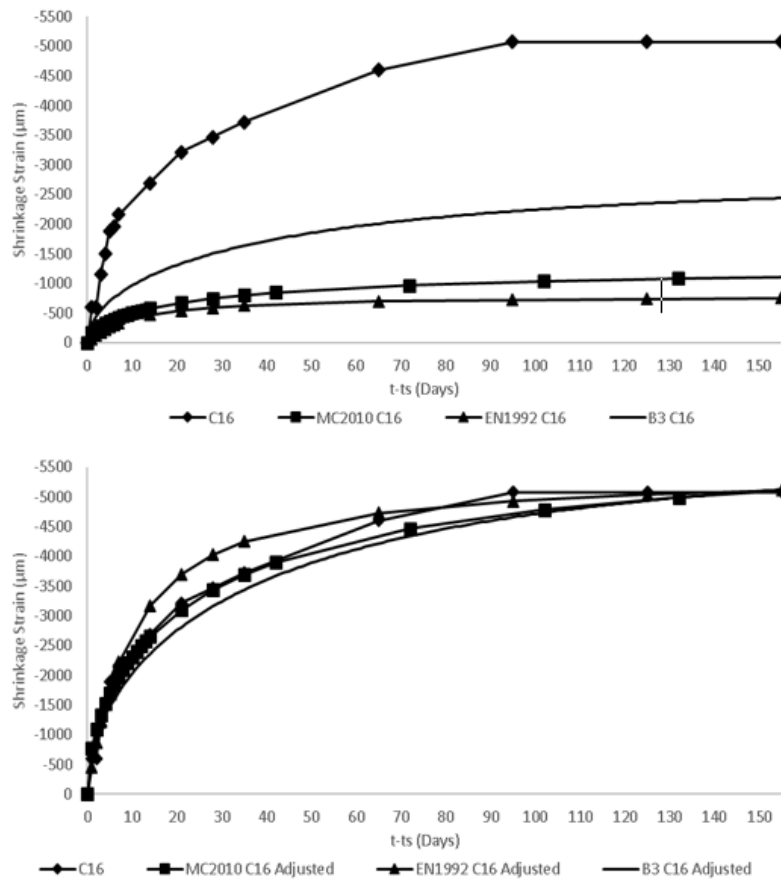


Figure 5-28: Numerical Modelling C16

Table 5-21: Numerical Model Shrinkage Adjustment Factors

Mix/Code	MC2010	EN1992	B3
C12	4.3	6	3.5
C14	4.1	6	2.5
C16	4.6	6.8	2.1
AVE	4.33	6.3	2.7

Figure 5-29 – Figure 5-31 indicate the results of populating the numerical models with the physical properties of the samples subjected to creep testing. It may be noted that although slight variations occur, provided the relevant Young’s moduli for each mix are used as given in Table 5-13 the numerical models appear to represent the true creep behaviour relatively well. As the Rilem B3 model relies upon an aggregate/cement ratio for calculation of total creep strains, correlation has been difficult to achieve and thus, only adjustments for the MC2010 code and EN1992 are provided.

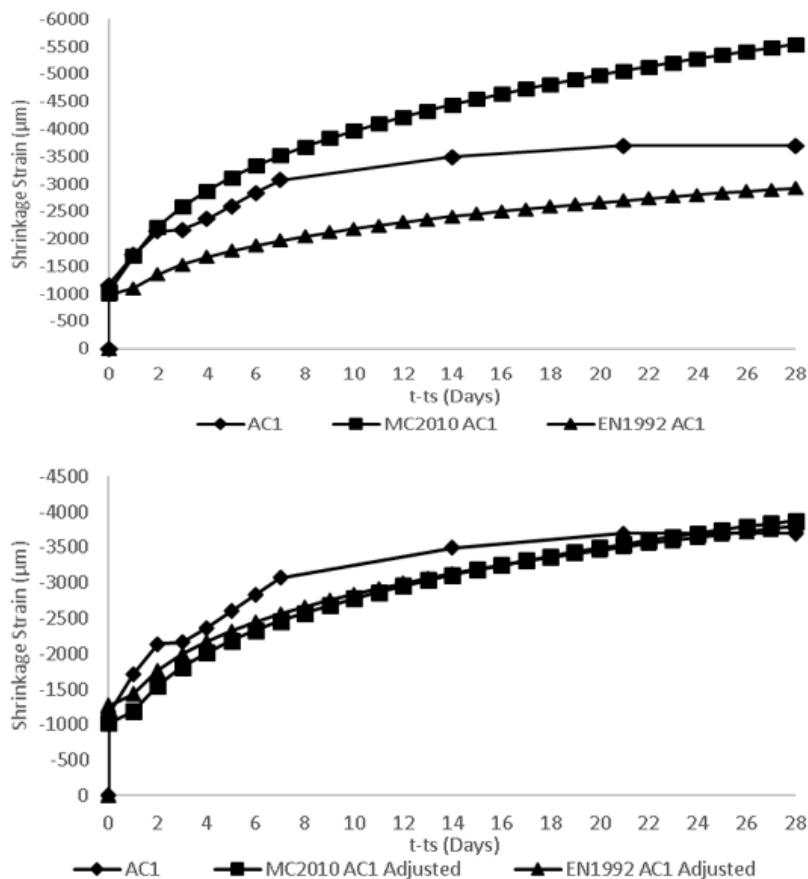


Figure 5-29: Numerical Modelling AC1

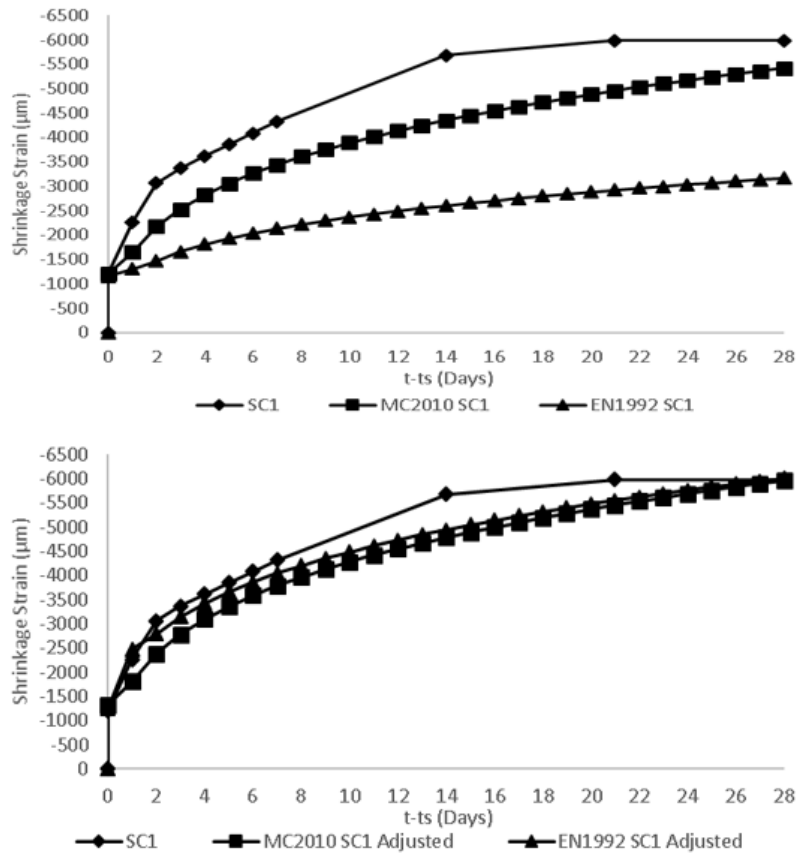


Figure 5-30: Numerical Modelling SC1

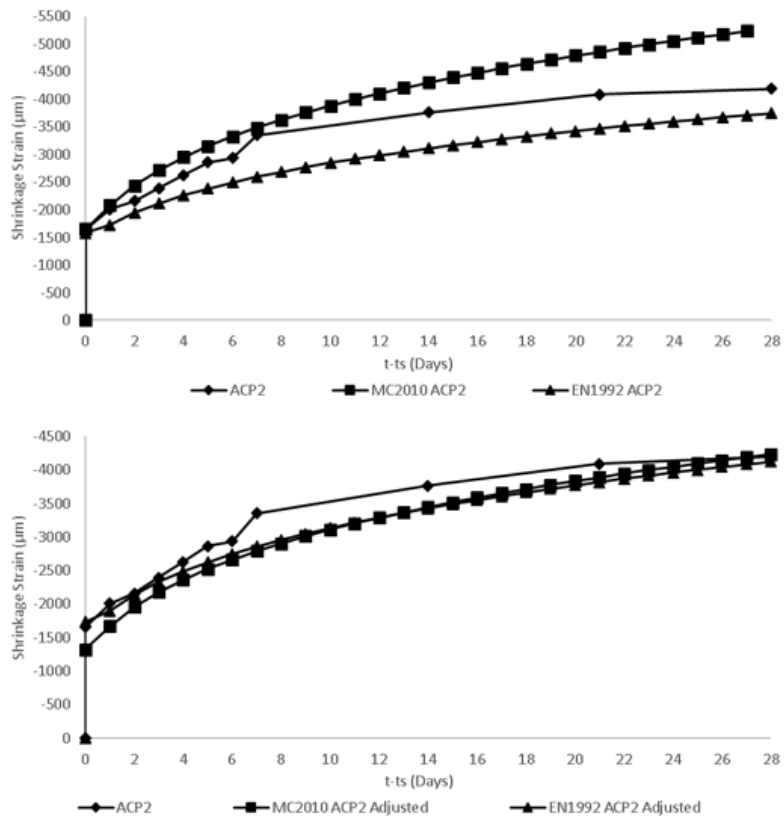


Figure 5-31: Numerical Modelling ACP2

Table 5-13: Numerical Model Creep Adjustment Factors

<i>Mix/Code</i>	MC2010	EN1992
AC1	0.7	1.3
SC1	1.1	1.9
ACP2	0.8	1.1
AVE	0.9	1.4

5.3 Physical Results vs Finite Element Results

In Chapter 4 an axisymmetric finite element model to replicate the results of physical creep and shrinkage tests on NWC cylinders is developed. This finite element model has been calibrated with existing data and the results verified by comparing the physically obtained results to those obtained by indirect input of creep and shrinkage curves into the Diana Kelvin-Chain model. The indirect input of creep and shrinkage curves into Diana yields results which match physical tests almost perfectly. With drying shrinkage, autogenous shrinkage, drying creep, basic creep and specific creep curves generated from the physical testing of various LWFC samples, these results are available for use to replicate creep and shrinkage tests in the finite element model.

Figure 5-32 – Figure 5-39 indicate the results of physical testing and Diana modelling output for the four mix variations tested both for shrinkage and creep. It should be noted that for all mix variations with all fillers in varying the ratios, the indirect shrinkage and creep curve input allows for precise strain modelling and thus, these four mixes are only shown as examples. Investigating the results of shrinkage modelling shown in Figure 5-32 – Figure 5-35, it may be seen that due to the absence of an externally applied unit stress, the output shrinkage curve generated from Diana matches those of experimental results exactly. When investigating the results obtained for creep modelling shown in Figure 5-36- Figure 5-39, it may be seen that the externally applied unit stress as well as the specified Young's modulus play a larger role on the curve fitting solution method employed by Diana when modelling a viscoelastic Kelvin-Chain material. The results obtained from Diana for creep testing vary approximately -0.57%, 0.023%, -0.81% and -0.44% from experimental results for mixes AC1, SC1, AC2 and ACP2 respectively.

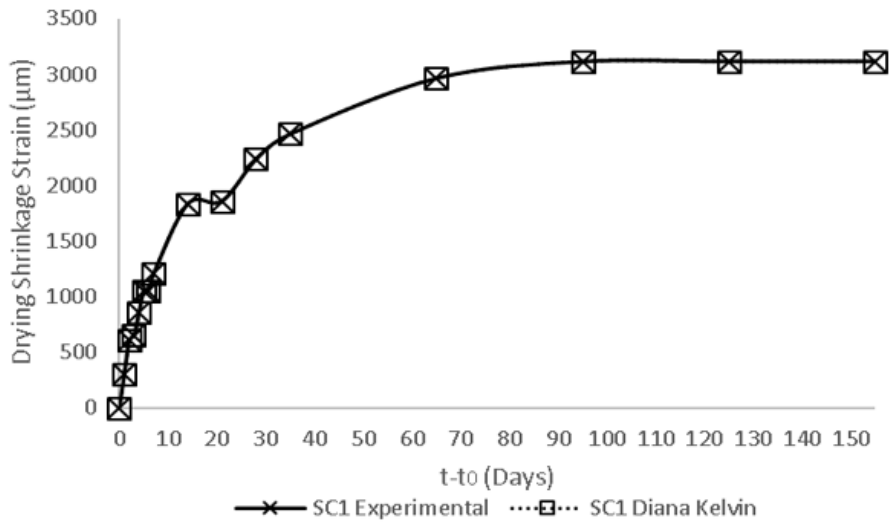


Figure 5-32 Diana Shrinkage Modelling SC1

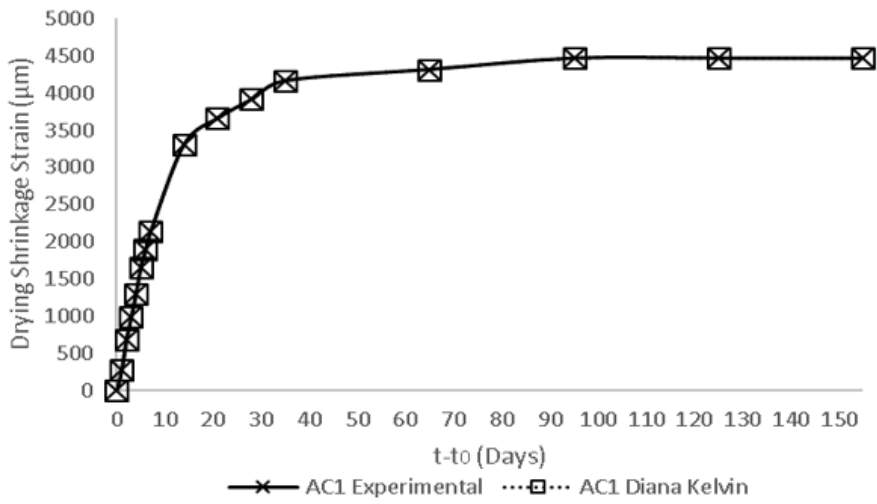


Figure 5-33: Diana Shrinkage Modelling AC1

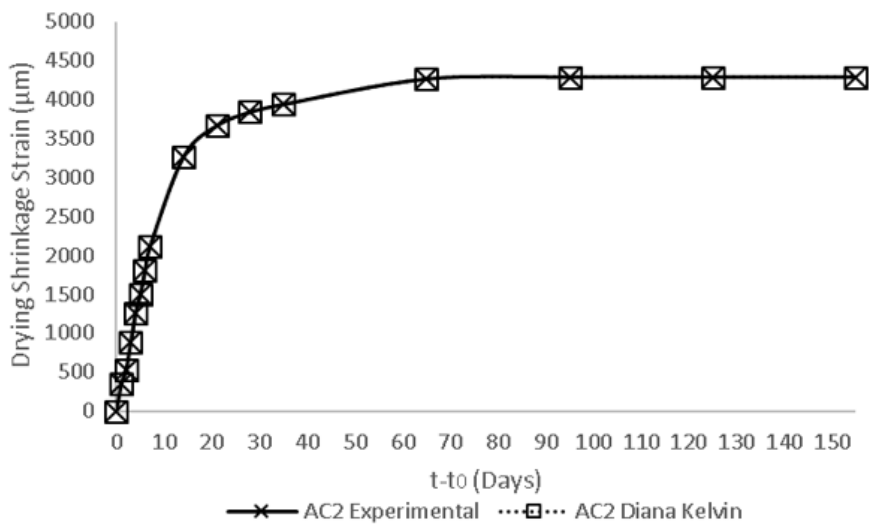


Figure 5-34: Diana Shrinkage Modelling AC2

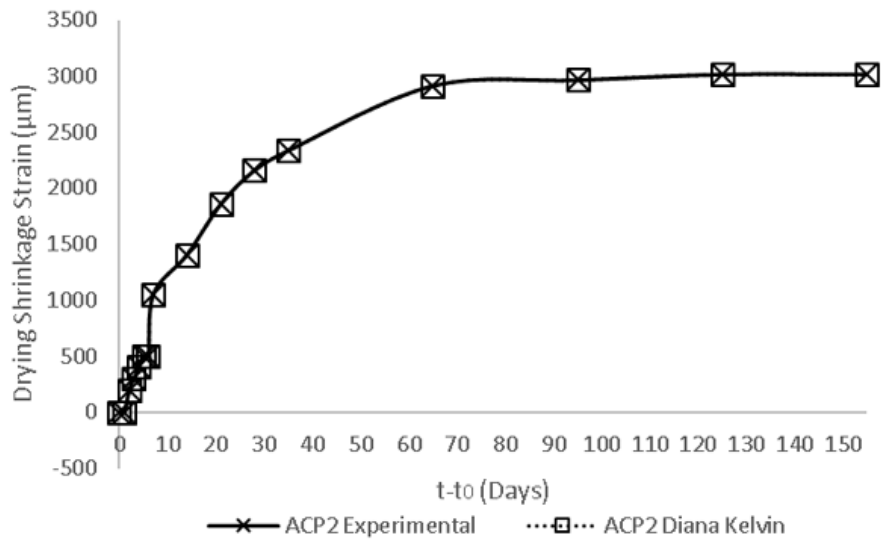


Figure 5-35: Diana Shrinkage Modelling ACP2

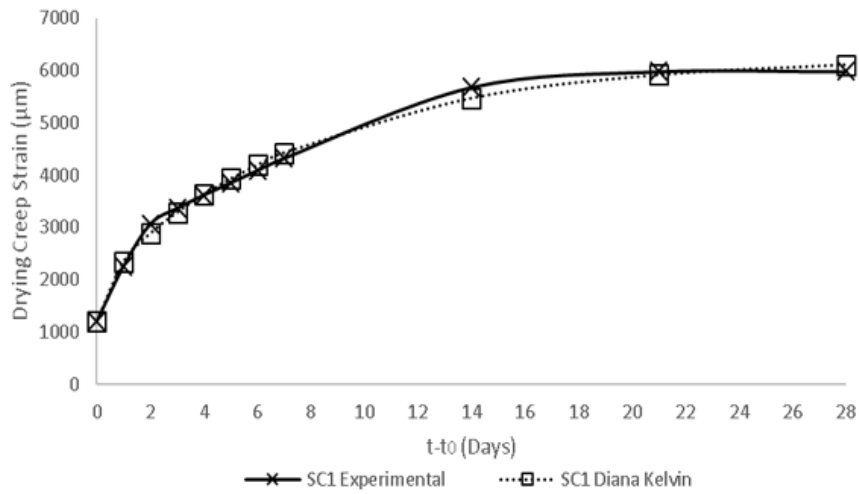


Figure 5-36: Diana Creep Modelling SC1

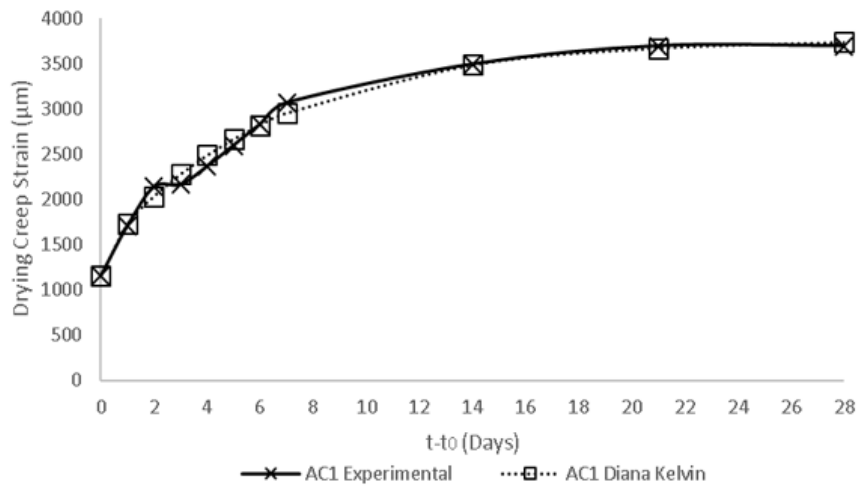


Figure 5-37: Diana Creep Modelling AC1

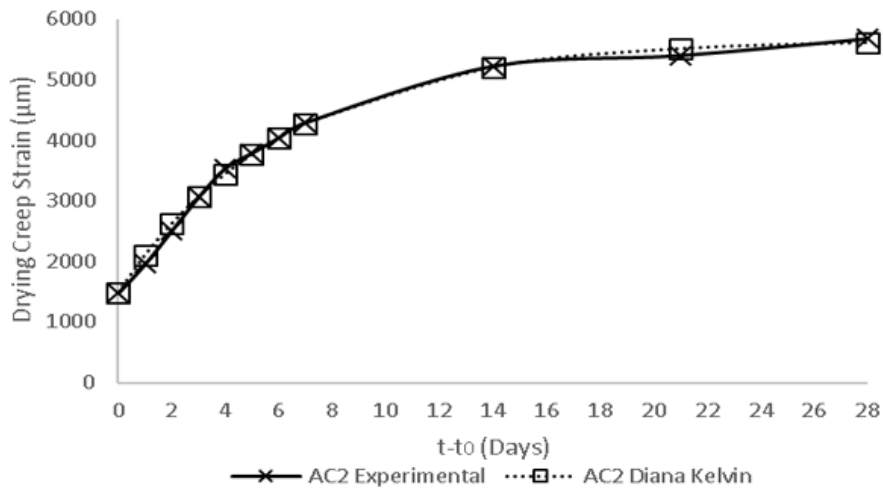


Figure 5-38: Diana Creep Modelling AC2

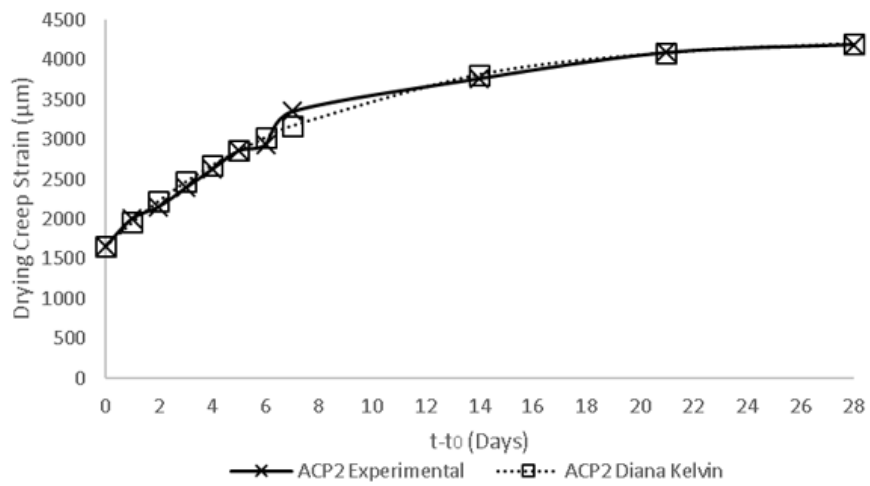


Figure 5-39: Diana Creep Modelling ACP2

Chapter 6 – Conclusions and Recommendations

This chapter provides a brief summary of the research conducted in this thesis and the procedures followed to attain experimental findings. The key research objectives given in Chapter 1 are then indicated and the fundamental observations, results and conclusions drawn therefrom are also provided. In addition, the chapter is concluded by providing recommendations for further research on the topic.

Thorough research together with experimental results, model code investigation and finite element modelling has been used in an effort to attain a holistic understanding of the creep and shrinkage behaviour of LWFC. The effects of foam volume, density, cement content and other fillers have been investigated by conducting experimental creep and shrinkage testing on a variety of LWFC samples which vary in density, inclusion of sand and fly ash as well as other additives such as propylene glycol. These results, together with results replicated in model codes and finite element analysis provide an indication of the dimensional stability of some typical LWFC variations.

6.1 Conclusions

- The maximum drying shrinkage strain recorded in excess of 6000 μm appears to verify findings such as that of (Nambiar, 2014), where LWFC has been seen to exhibit drying shrinkage strains more than six times larger than those seen in NWC specimens.
- Under sealed conditions, findings in this thesis indicate that autogenous shrinkage strains in LWFC may also exceed 3000 μm . In contradiction to other findings, results presented in this thesis indicate that there appears to be an inverse relationship between the density and drying shrinkage values in LWFC.
- This research has also indicated that LWFC mixes containing only cement exhibit much larger drying shrinkage values than those containing fillers, fly ash is less effective at reducing shrinkage than sand and increasing the filler-cement ratio both for sand and fly ash does aid in reducing the total amount of drying shrinkage exhibited. Additionally, including seven percent propylene glycol by weight of cement as an additive is highly effective at reducing the total amount of drying shrinkage experienced in LWFC specimens.
- The maximum drying creep strains are seen to be approximately six times higher than equivalent NWC in the range of 6000 μm .
- For drying creep it has been noted that sand is less effective than fly ash at restraining creep strains which is attributed to the larger strength gain in LWFC mixes containing fly ash. It has also been

seen that increasing the filler-cement ratio in LWFC results in higher drying creep strains, particularly when increasing the filler-cement ratio of LWFC containing fly ash.

- For basic creep measurements under sealed conditions, it has been noted that sand is more effective than fly ash at restraining creep strains and even under sealed conditions, LWFC still exhibits creep strains in excess of $3000\mu\text{m}$. Much like for drying shrinkage, the inclusion of seven percent propylene glycol by weight of cement has seen considerable reductions in the total amount of drying creep exhibited.
- All theoretical prediction models studied have shown good correlation in results for NWC, however, when populated with typical LWFC parameters all three models appear to severely underestimate the total strain values. By investigating and comparing theoretical results to those obtained experimentally, corrections have been made to attain preliminary adjustment factors for the creep and shrinkage values obtained from each model. For shrinkage behaviour, adjustment factors of 4.33, 6.3 and 2.7 have been obtained for the MC2010, EN1992 and B3 models respectively, whilst creep strain adjustment factors have been identified as 0.9 and 1.4 for the EN1992 and B3 models.
- The axisymmetric nonlinear viscoelastic Kelvin-Chain model developed is an effective way of replicating experimental results. Model code material models included in Diana FEA Software provide sufficiently accurate results for NWC, however, user-defined indirect input of experimental creep and shrinkage curves appears to be the most accurate way to replicate the long-term deformation behaviour of samples both for NWC and LWFC. The experimental results attained from physical testing of LWFC samples presented in this thesis are able to provide the necessary shrinkage and specific creep curves required to create a user-defined material model in Diana. These results may be used for future research and finite element modelling of LWFC where long-term deformation behaviour is required.
- The increase in creep and shrinkage strains in LWFC compared to NWC are almost certainly attributed to the reduction in stiffness of the hardened cement paste caused by the inclusion and coalescence of zero-stiffness air voids. It appears that this air void structure is far more responsible for increased creep and shrinkage strains than the removal of water from micropores which is the leading cause of creep and shrinkage in NWC.

6.2 Recommendations

By considering the entire experimental program, the results obtained and limitations experienced, it is possible to provide some recommendations on topics which would be suitable for further investigation in future research. These recommendations are as follows:

- i. Future research may be able to build upon the findings presented in this thesis by testing the dimensional stability of LWFC mixes containing different fillers such as silica-fume and ground-granulated blastfurnace slag. In addition, the effects of various fibres and the addition of superplasticisers may also be investigated.
- ii. Equivalent samples cast from base mixes without the addition of foam may be tested in an effort to gain an accurate indication of the effects of foam on the total shrinkage and creep strains compared to the shrinkage and creep arising from the paste itself.
- iii. The effects of moisture content and cement content on shrinkage and creep may be investigated by testing equivalent mixes with varying water-cement ratios.
- iv. The dimensional stability of 3D printed LWFC may be investigated by printing equivalent cylindrical samples and subjecting them to the same creep and shrinkage testing conducted in this thesis. The creep and shrinkage behaviour of 3D printed LWFC may then be directly compared to LWFC samples which has been prepared in a traditional way.

References

- Amran, Y.H.M., Farzadnia, N. & Ali, A.A.A. 2015. Properties and applications of foamed concrete ; a review. *CONSTRUCTION & BUILDING MATERIALS*. 101:990–1005.
- Awang, H. & Ahmad, M.H. 2015. Durability Properties of Foamed Concrete with Fiber Inclusion. (January 2014).
- Bažant, Z.R. & Prasannan, S. 1989. Solidification theory for concrete creep. I: Formulation. *J. Engrg. Mech, ASCE*. 115(8):1691–1703.
- Chindapasirt, P. & Rattanasak, U. 2011. Shrinkage behavior of structural foam lightweight concrete containing glycol compounds and fly ash. *Materials and Design*. 32(2):723–727.
- Domone, P. & Illston, J. 2010. *Construction Materials Their Nature and Behaviour*. Fourth ed. P. Domone & J. Illston (eds.). Spon Press.
- Du, L. & Folliard, K.J. 2005. Mechanisms of air entrainment in concrete. 35(July 2004):1463–1471.
- Gribniak, V., Kaklauskas, G. & Bacinskas, D. 2008. Shrinkage in reinforced concrete structures: A computational aspect. *Journal of Civil Engineering and Management*. 14(1):49–60.
- Hedegaard, B.D., Asce, S.M., Shield, C.K., Asce, M., French, C.E.W. & Asce, M. 2014. Smear-Bar Model for Viscoelastic Analysis of Uncracked Reinforced Concrete Smear-Bar Model for Viscoelastic Analysis of Uncracked Reinforced Concrete Structures. (November 2015).
- Hilal, A.A., Thom, N.H. & Dawson, A.R. 2015a. On void structure and strength of foamed concrete made without/with additives. *Construction and Building Materials*. 85:157–164.
- Hilal, A.A., Thom, N.H. & Dawson, A.R. 2015b. On entrained pore size distribution of foamed concrete. *Construction and Building Materials*. 75:227–233.
- Kearsley, E.P. & Wainwright, P.. 2001. The effect of high fly ash content on the compressive strength of foamed concrete. *Cement and Concrete Research*. 105–112.
- Kunhanandan Nambiar, E.K. & Ramamurthy, K. 2008. Fresh state characteristics of foam concrete. *Journal of Materials in Civil Engineering*. 20(2):111–117.
- Mehta, P.K. & Monteiro, P.J.M. 2006. *Concrete Microstructure, Properties and Materials*. Third Edit ed. McGraw-Hill (ed.).
- Nambiar, E.K.K. 2014. Shrinkage Behavior of Foam Concrete. 1561(May).

- Nambiar, E.K.K. & Ramamurthy, K. 2006. Influence of filler type on the properties of foam concrete. *Cement and Concrete Composites*. 28(5):475–480.
- Narayanan, N. & Ramamurthy, K. 2000. Structure and properties of aerated concrete: A review. *Cement and Concrete Composites*. 22(5):321–329.
- Owens, G. 2013. *Fundamentals of Concrete*. Third ed. G. Owens (ed.). The Concrete Institute.
- Paul, T. & Dunn, A. 2017. Precast Lightweight Foamed Concrete Walling , a Structural System for Low-Rise Residential Buildings by. (December).
- Ramamurthy, K., Kunhanandan Nambiar, E.K. & Indu Siva Ranjani, G. 2009. A classification of studies on properties of foam concrete. *Cement and Concrete Composites*. 31(6):388–396.
- Robert, B., Robert, F., Tristana, Y., Thomas, L. & Kamyar, C. 2015. Fabrication and Testing of Low-Energy Calcium Sulfoaluminate-Belite Cements that Utilize Fluidized Bed Combustion By-Products. (July).
- van Rooyen, A.S. 2013. Structural lightweight aerated concrete. (March):102. [Online], Available: <http://scholar.sun.ac.za/handle/10019.1/80106>.
- SANS. 2006. SANS 5863 : 2006 SOUTH AFRICAN NATIONAL STANDARD Concrete tests — Compressive strength of hardened concrete. 2–6.
- de Villiers, J.P., van Zijl, G.P.A.G. & van Rooyen, A.S. 2017. Bond of deformed steel reinforcement in lightweight foamed concrete. *Structural Concrete*. 18(3):496–506.
- De Villiers, J. 2015. Bond behaviour of deformed steel in lightweight foamed concrete. (December).
- Wei, S., Yiqiang, C., Yunsheng, Z. & Jones, M.R. 2013. Characterization and simulation of microstructure and thermal properties of foamed concrete. *Construction and Building Materials*. 47(October):1278–1291.

Appendices

Appendix A – Drying Shrinkage Strains

A-1: Average Drying Shrinkage Strain Readings

Drying Shrinkage Strains (μm)											
t (Days)	C12	C14	C16	SC1	SC2	AC1	AC2	SAC1	SAC2	ACP2	SCP2
0	0	0	0	0	0	0	0	0	0	0	0
1	-552.69	-678.77	-603.12	-301.48	-251.06	-276.14	-351.49	-326.34	-125.50	0.00	0.00
2	-1080.28	-1256.90	-603.12	-602.97	-552.32	-677.76	-527.24	-451.86	-238.45	-200.89	-125.65
3	-1457.16	-1558.56	-1155.98	-653.20	-803.37	-991.53	-891.26	-577.38	-351.40	-301.34	-125.65
4	-1959.60	-1935.65	-1507.80	-854.22	-979.11	-1305.29	-1255.28	-1004.13	-451.79	-401.78	-125.65
5	-2311.38	-2086.44	-1884.75	-1055.21	-1104.64	-1656.75	-1506.34	-1292.82	-589.84	-502.23	-125.65
6	-2361.55	-2212.11	-1960.14	-1055.22	-1104.64	-1895.20	-1807.60	-1581.52	-727.89	-502.23	-125.65
7	-2612.80	-2438.32	-2161.18	-1205.96	-1205.06	-2133.66	-2108.86	-1857.66	-1129.49	-1054.69	-427.21
14	-3441.87	-3066.74	-2688.91	-1834.07	-1757.38	-3313.39	-3263.71	-2912.02	-2058.18	-1406.25	-477.46
21	-4195.57	-3745.44	-3216.64	-1859.20	-2058.64	-3664.83	-3665.40	-3288.56	-2208.78	-1858.26	-728.75
28	-4321.19	-3896.26	-3467.95	-2236.06	-2083.75	-3915.87	-3841.15	-3539.60	-2258.98	-2159.60	-904.65
35	-4773.39	-4424.11	-3719.25	-2462.16	-2334.80	-4166.88	-3941.56	-3589.81	-2334.28	-2335.38	-1055.44
65	-5476.85	-5127.98	-4598.80	-2964.66	-2410.12	-4317.52	-4267.93	-3840.85	-2610.37	-2912.95	-1331.85
95	-5903.92	-5479.86	-5076.27	-3115.40	-2811.81	-4468.13	-4293.03	-3891.05	-2635.47	-2963.18	-1331.85
125	-6029.58	-5504.98	-5076.27	-3115.40	-2811.81	-4468.13	-4293.03	-3916.15	-2635.47	-3013.40	-1331.85
155	-6029.58	-5504.98	-5076.27	-3115.40	-2811.81	-4468.13	-4293.03	-3916.15	-2635.47	-3013.40	-1331.85

Appendix B – Drying Shrinkage Mass Loss

Mix	Sample	Mass at start of testing (kg)	Mass at end of testing (kg)	% loss	Avg
C12	1A1	1.807	1.761	2.535	2.513
	1A2	1.942	1.894	2.492	
C14	1B1	2.410	2.368	1.726	1.685
	1B2	2.211	2.175	1.643	
C16	1C1	2.702	2.626	2.824	2.850
	1C2	2.569	2.495	2.877	
SC1	2A1	2.254	2.195	2.607	2.437
	2A2	2.372	2.318	2.267	
SC2	2B1	2.302	2.265	1.606	1.926
	2B2	2.283	2.232	2.246	
AC1	3A1	2.262	2.145	5.172	4.981
	3A2	2.240	2.133	4.790	
AC2	3B1	2.204	2.022	8.271	8.453
	3B2	2.197	2.007	8.635	
SAC1	4A1	2.118	1.997	5.732	5.651
	4A2	2.113	1.995	5.570	
SAC2	4B1	2.419	2.214	8.495	8.624
	4B2	2.308	2.106	8.752	
ACP2	5A1	2.312	2.105	8.959	8.896
	5A2	2.214	2.018	8.834	
SCP2	5B1	2.177	2.105	3.289	3.157
	5B2	2.341	2.270	3.026	

Appendix C – Autogenous Shrinkage Strains

C-1: Average Autogenous Shrinkage Strains

Autogenous Shrinkage Strains (μm)											
t (Days)	C12	C14	C16	SC1	SC2	AC1	AC2	SAC1	SAC2	ACP2	SCP2
0	0	0	0	0	0	0	0	0	0	0	0
1	-70.28	-151.06	-125.50	-125.54	25.11	25.11	-75.31	-50.19	0.00	-100.40	-75.40
2	-421.67	-453.36	-502.10	-251.07	50.21	-100.37	-125.51	-100.38	-0.01	-100.40	-134.05
3	-496.97	-516.36	-602.52	-351.50	-125.52	-125.47	-200.80	-50.19	75.28	-100.40	-192.71
4	-572.28	-579.35	-702.95	-477.06	-175.72	-225.86	-250.99	-326.25	-0.01	-100.40	-251.36
5	-722.90	-755.76	-778.28	-627.68	-376.56	-326.24	-276.09	-313.70	-12.56	-100.40	-251.36
6	-873.51	-906.78	-1079.54	-703.00	-426.75	-376.45	-250.98	-301.15	-25.11	-100.40	-251.36
7	-1262.55	-1322.55	-1431.03	-728.11	-451.86	-790.53	-376.46	-363.89	-62.75	-100.40	-251.36
14	-1651.59	-1738.33	-1782.51	-1029.41	-577.36	-1204.62	-501.95	-426.63	-100.40	-225.89	-301.64
21	-1977.93	-2015.65	-2033.56	-1305.55	-652.69	-1229.72	-501.95	-476.82	-150.59	-251.00	-301.64
28	-2228.91	-2141.49	-2234.40	-1481.33	-803.30	-1505.76	-677.63	-602.30	-175.69	-401.61	-301.64
35	-2505.01	-2292.60	-2359.95	-1606.84	-928.81	-1555.95	-778.02	-652.50	-175.69	-401.61	-301.64
65	-3007.01	-2947.69	-2987.59	-2109.00	-1355.56	-1731.65	-1129.37	-677.59	-175.69	-803.19	-301.64
95	-3107.39	-2972.90	-3163.35	-2385.19	-1656.80	-1932.42	-1305.05	-677.59	-175.69	-803.19	-301.64
125	-3132.50	-2998.07	-3238.67	-2435.41	-1656.80	-1932.42	-1305.05	-702.69	-175.69	-803.19	-301.64
155	-3132.50	-2998.07	-3238.67	-2435.41	-1656.80	-1932.42	-1305.05	-702.69	-175.69	-803.19	-301.64

Appendix D – Autogenous Shrinkage Mass Loss

Mix	Sample	Mass at start of testing (kg)	Mass at end of testing (kg)	% loss	Avg
C12	1A3	2.065	2.052	0.630	0.848
	1A4	2.063	2.041	1.066	
C14	1B3	2.360	2.356	0.153	0.216
	1B4	2.325	2.319	0.280	
C16	1C3	2.601	2.583	0.688	0.740
	1C4	2.590	2.570	0.792	
SC1	2A3	2.587	2.561	0.997	1.109
	2A4	2.415	2.386	1.222	
SC2	2B3	2.492	2.467	1.023	1.134
	2B4	2.410	2.380	1.245	
AC1	3A3	2.363	2.340	0.956	0.930
	3A4	2.269	2.249	0.903	
AC2	3B3	2.254	2.236	0.794	0.859
	3B4	2.243	2.222	0.923	
SAC1	4A3	2.122	2.122	0.005	0.073
	4A4	2.259	2.256	0.142	
SAC2	4B3	2.374	2.356	0.767	0.814
	4B4	2.347	2.327	0.861	
ACP2	5A3	2.369	2.364	0.190	0.187
	5A4	2.385	2.381	0.184	
SCP2	5B3	2.429	2.425	0.152	0.157
	5B4	2.400	2.396	0.163	

Appendix E – Drying Creep Average Strains

E-1: Average Drying Creep Strain Readings

t (Days)	Drying Creep Strains (μm)				Specific Creep			
	AC1	SC1	AC2	ACP2	AC1	SC1	AC2	ACP2
0	0	0	0	0	0	0	0	0
0.0001	-1156.57	-1206.45	-1481.46	-1656.97	-281.816	-250.426	-254.714	-250.073
1	-1709.71	-2262.1	-1958.59	-2008.45	-416.596	-469.55	-336.749	-303.12
2	-2137.13	-3066.41	-2511	-2159.09	-520.744	-636.501	-431.729	-325.854
3	-2162.28	-3368.02	-3063.42	-2393.42	-526.871	-699.107	-526.708	-361.219
4	-2363.42	-3619.36	-3540.53	-2627.74	-575.882	-751.279	-608.741	-396.584
5	-2598.09	-3853.95	-3791.63	-2862.07	-633.063	-799.973	-651.913	-431.949
6	-2832.76	-4088.54	-4042.7	-2937.37	-690.243	-848.667	-695.08	-443.314
7	-3067.43	-4323.13	-4293.73	-3351.61	-747.423	-897.361	-738.241	-505.832
14	-3494.85	-5680.39	-5222.9	-3765.85	-851.571	-1179.09	-897.998	-568.35
21	-3695.99	-5982	-5398.68	-4092.25	-900.582	-1241.7	-928.22	-617.611
28	-3695.99	-5982	-5674.84	-4192.69	-900.582	-1241.7	-975.703	-632.769

Appendix F – Basic Creep Strains

F-1: Average Basic Creep Strains

t (Days)	Basic Creep Strains (μm)				Specific Creep			
	AC1	SC1	AC2	ACP2	AC1	SC1	AC2	ACP2
0	0	0	0	0	0	0	0	0
0.0001	-1006.29	-754.831	-2284.91	-1983.87	-245.197	-156.682	-392.856	-299.41
1	-1056.6	-754.831	-2410.46	-2486.11	-257.457	-156.682	-414.441	-375.209
2	-1056.6	-754.831	-2460.68	-2586.48	-257.457	-156.682	-423.076	-390.356
3	-1056.6	-754.831	-2485.78	-2661.84	-257.457	-156.682	-427.392	-401.731
4	-1056.6	-754.831	-2485.78	-2712.12	-257.457	-156.682	-427.392	-409.318
5	-1056.6	-754.831	-2485.78	-2762.39	-257.457	-156.682	-427.392	-416.905
6	-1106.92	-754.831	-2485.78	-2762.39	-269.717	-156.682	-427.392	-416.905
7	-1106.92	-754.831	-2485.78	-2900.46	-269.717	-156.682	-427.392	-437.744
14	-1106.92	-754.831	-2485.78	-3038.53	-269.717	-156.682	-427.392	-458.582
21	-1106.92	-754.831	-2485.78	-3038.53	-269.717	-156.682	-427.392	-458.582
28	-1106.92	-754.831	-2485.78	-3038.53	-269.717	-156.682	-427.392	-458.582